

9-3-2010

# DNA translocation through an array of kinked nanopores

Zh Chen

Follow this and additional works at: [https://digitalrepository.unm.edu/cbe\\_etds](https://digitalrepository.unm.edu/cbe_etds)

---

## Recommended Citation

Chen, Zh. "DNA translocation through an array of kinked nanopores." (2010). [https://digitalrepository.unm.edu/cbe\\_etds/2](https://digitalrepository.unm.edu/cbe_etds/2)

This Dissertation is brought to you for free and open access by the Engineering ETDs at UNM Digital Repository. It has been accepted for inclusion in Chemical and Biological Engineering ETDs by an authorized administrator of UNM Digital Repository. For more information, please contact [disc@unm.edu](mailto:disc@unm.edu).

Zhu Chen

*Candidate*

Chemical Engineering

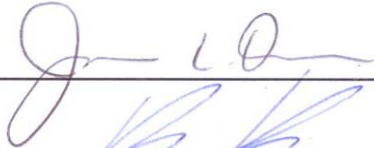
*Department*

This dissertation is approved, and it is acceptable in quality and form for publication:

*Approved by the Dissertation Committee:*



, Chairperson



**DNA TRANSLOCATION THROUGH AN ARRAY OF KINKED  
NANOPORES**

**BY**

**ZHU CHEN**

M.S., Chemical Engineering, The University of New Mexico, 2002

DISSERTATION

Submitted in Partial Fulfillment of the  
Requirements for the Degree of

**Doctor of Philosophy  
Engineering**

The University of New Mexico  
Albuquerque, New Mexico

**July, 2010**

© 2010 Zhu Chen

## ACKNOWLEDGMENTS

First of all, I sincerely acknowledge Professor C. Jeffrey Brinker, my advisor and dissertation chair, for his guidance, advice and support throughout my PhD research. His passion and dedication to work and his view in research have continuously inspired me to push the boundary to explore my potential as a researcher, as a coworker and as a human being. I am also grateful to my dissertation committee members Prof. Tim L. Ward, Prof. David John Keller, Prof. James Thomas and Dr. Darren R. Dunphy for their guidance, invaluable suggestions, insightful comments and their time in reviewing this dissertation.

A special thank goes to Dr. Ying-Bing Jiang, my closest friend and colleague who not only generously helped me with his expertise in TEM and ALD, but also provided tremendous support and encouragement throughout my research. Same thank goes to Dr. Nanguo Liu, also my closest friend and previous colleague, for his invaluable discussion and contribution in patch clamp set-up and cell-device design.

I would also like to thank everyone who have contributed to the experimental/model parts of this dissertation, especially Dr. Darren R. Dunphy for his contribution in GISAXS characterization and electrochemical deposition of Pt replica, Dr. David P. Adams and Mr. Carter Hodges from Sandia National Laboratory for their contribution in making single nanopores on SiN membrane using FIB lithography, Prof. N. RA. Aluru and Dr. Xiaozhong Jin from UIUC for their contribution in developing the transport model, Prof. Hugh W. Hillhouse and Mr. Steven J. Gaik from Purdue University for their contribution in GISAXS characterization and Dr. Nan Zhang for his contribution in PCR amplification.

Also many thanks go to Dr. George Xomeritakis, Dr. Carlee Ashley, Dr. Juewen Liu, Ms. Robin Sewell, Mr. Fred Garcia, Dr. Hongyou Fan, Dr. Zaicheng Sun, Dr. Huimeng Wu, Dr. Feng Bai, Mr. Shisheng Xiong and Dr. Xingmao Jiang for their help in the lab.

I would like to acknowledge Ms. Carol Ashley for her generous support during my PhD study at AML. Also many thanks go to Ms. Estelle Zamora, Ms. Maureen Reynold, Mr. Eric branson, Mr. Adam Cook, Mr. Ian Cooper and Ms. Cathy Casper for their administrative or technical support to make my PhD research a lot easier.

Finally, I am deeply indebted to my family for their love, support and encouragement, which have lead to every success in this dissertation.

**DNA TRANSLOCATION THROUGH AN ARRAY OF KINKED  
NANOPORES**

**BY**

**ZHU CHEN**

**ABSTRACT OF DISSERTATION**

Submitted in Partial Fulfillment of the  
Requirements for the Degree of

**Doctor of Philosophy  
Engineering**

The University of New Mexico  
Albuquerque, New Mexico

**July, 2010**

# **DNA translocation through an array of kinked nanopores**

by

Zhu Chen

M.S., Chemical Engineering, The University of New Mexico, 2002

Ph.D., Engineering, The University of New Mexico, 2010

## **Abstract**

Synthetic solid-state nanopores are being intensively investigated as single-molecule sensors for detection and characterization of DNA, RNA, and proteins. This field has been inspired by the exquisite selectivity and flux demonstrated by natural biological channels and the dream of emulating these behaviors in more robust synthetic materials that are more readily integrated into practical devices. To date, the guided etching of polymer films, focused ion beam sculpting, and electron-beam lithography and tuning of silicon nitride membranes have emerged as three promising approaches to define synthetic solid-state pores with sub-nanometer resolution. These procedures have in common the formation of nominally cylindrical or conical pores aligned normal to the membrane surface. Here we report the formation of ‘kinked’ silica nanopores, using evaporation induced self-assembly, and their further tuning and chemical derivatization using atomic layer deposition. Compared to ‘straight-through’ proteinaceous nanopores of comparable dimensions, kinked nanopores exhibit a factor of up to 5x reduction in translocation velocity, which has been identified as one of the critical issues in DNA sequencing. Additionally we demonstrate an efficient two-step approach to create a



nanopore array exhibiting nearly perfect selectivity for ssDNA over dsDNA. We show that a coarse-grained drift-diffusion theory with a sawtooth like potential can reasonably describe the velocity and translocation time of DNA through the pore. By control of pore size, length, and shape, we capture the major functional behaviors of protein pores in our solid-state nanopore system.

# TABLE OF CONTENTS

<b>CHAPTER 1. INTRODUCTION</b> .....	1
1.1 Overview of the development in DNA sequencing .....	1
1.2 Physical characteristics of DNA .....	8
1.2.1 DNA structure .....	8
1.2.2 Charge of DNA .....	9
1.2.3 Electric field.....	9
1.2.4 Elastic properties of polynucleotides.....	11
1.3 Coulter counter principle .....	12
1.4 Molecular sensor.....	13
1.4.1 Single-Channel Recording.....	14
1.4.2 Other molecular detection approaches.....	15
1.4.3 Size-related issues at molecular scale .....	16
1.5 Nanopore approach.....	17
1.5.1 Biological nanopore approach .....	17
1.5.2 Solid-state nanopore approach.....	20
1.6 Concept of Evaporation-Induced-Self-Assembly (EISA) .....	23
1.6.1 Surfactant-directed-self-assembly (SDSA).....	23
1.6.2 Evaporation-Induced-Self-Assembly (EISA) .....	24
1.6.3 Functional mesoporous materials .....	26
1.7 Concept of Atomic-Layer-Deposition (ALD) .....	27
1.8 Focused-Ion-Beam (FIB) lithography.....	31

1.9 Problem statement.....	32
<b>CHAPTER 2. GOALS AND OBJECTIVES .....</b>	<b>34</b>
<b>CHAPTER 3. EXPERIMENTAL .....</b>	<b>36</b>
3.1 Material preparation .....	36
3.1.1 Reagents and Materials.....	36
3.1.2 Synthesis of ultra-thin mesoporous silica film.....	36
3.1.3 ALD to fine tune the pore size and surface chemistry.....	38
3.1.4 FIB lithography to fabricate sub 100 nm single pore on SiN substrate.....	39
3.2 Material Characterization.....	41
3.2.1 Transmission Electron Microscopy (TEM).....	41
3.2.2 Scanning Electron Microscopy (SEM).....	42
3.2.3 Thermal analysis.....	42
3.2.4 N <sub>2</sub> adsorption/desorption isotherms of thin films.....	42
3.2.5 Ellipsometry .....	43
3.2.6 Fourier-Transform Infrared (FTIR) spectroscopy .....	43
3.2.7 Grazing Incidence Small Angle X-Ray Scattering (GISAXS) .....	43
3.2.8 X-Ray Diffraction (XRD) .....	44
3.2.9 Pt deposition experiment .....	44
3.2.10 Contact angle measurement.....	44
3.3 DNA translocation experiments.....	45
3.3.1 DNA design.....	45
3.3.2 DNA solution.....	48
3.3.3 Patch clamp instrumentation .....	48

3.3.4 Electrochemical cell device.....	49
3.3.5 Experimental procedure .....	49
<b>CHAPTER 4. RESULTS AND DISCUSSION I: FABRICATION OF NANOPORE ARRAY BY EISA .....</b>	<b>51</b>
4.1 Synthesis and characterization of ultrathin mesoporous silica film with brij 56 as surfactant on a solid substrate .....	51
4.1.1 X-ray diffraction.....	52
4.1.2 GISAXS characterization of ultra-thin mesoporous silica film .....	52
4.1.3 TEM.....	61
4.2 Determination of pore size and pore tortuosity .....	66
4.2.1 Surface-Acoustic-Wave (SAW) method .....	66
4.2.2 Synthesis of Pt replica in mesoporous structure.....	67
4.3 Fabrication of novel nanopore array .....	80
4.3.1 Fabrication of sub 100 nm single pore on SiN substrate by FIB.....	80
4.3.2 Fabrication of self-assembled nanopore array.....	81
4.4 Surfactant removal .....	95
4.4.1 Thermal treatment .....	95
4.4.2 Other treatment for surfactant removal .....	96
<b>CHAPTER 5. RESULTS AND DISCUSSION II: ATOMIC-LAYER-DEPOSITION (ALD) FOR THE MODIFICATION OF PORE SIZE AND PORE SURFACE CHEMISTRY.....</b>	<b>99</b>
5.1 TiO <sub>2</sub> ALD .....	99
5.1.1 TiO <sub>2</sub> ALD to fine tune the pore size.....	99

5.1.2 TiO <sub>2</sub> ALD to enhance the stability of silica thin film in high ionic solution.....	105
.....	105
5.2 Aminopropyl trimethoxysilane ALD .....	107
5.3 Piranha treatment.....	110
<b>CHAPTER 6. RESULTS AND DISCUSSIONS III: DNA TRANSLOCATION</b>	
.....	115
6.1 dsDNA translocation through 2.6-nm nanopore .....	115
6.2 ssDNA translocation through 1.4-nm nanopore after monolayer ALD of amino ligand.....	121
6.3 polymerase chain reaction (PCR) analysis to show DNA translocation .....	126
6.4 Transport model .....	129
6.5 Evaluation of noise level in nanopore array.....	134
6.6 Current blockade frequency as a function of pore number .....	138
<b>CHAPTER 7. CONCLUSIONS AND FUTURE WORK</b> .....	140
<b>REFERENCES</b> .....	147

# **Chapter 1**

## **Introduction**

Synthetic solid-state nanopores are being intensively investigated in the past a few years as single-molecule sensors for detection and characterization of DNA, RNA, and proteins. This field has been inspired by the exquisite selectivity and flux demonstrated by natural biological channels and the dream of emulating these behaviors in more robust synthetic materials that are more readily integrated into practical devices. In this dissertation, I will introduce a novel synthetic solid-state nanopore approach developed for DNA translocation and explore its unique features to facilitate potential DNA sequencing and separation/purification. In this Chapter, I will first give an overview of the development in DNA sequencing and the possible impact of the nanopore approach on DNA sequencing to address some major challenges that had been encountered by other approaches. Then, the background knowledge on the physical properties of DNA will be given, followed by a brief introduction of the most popular single molecule detection methods (derived from coulter counter principle). After that, I will go through the recent progress in the nanopore approaches from biological nanopores to synthetic solid-state nanopores. Finally, I will introduce a few techniques developed or modified in our group, e.g., Evaporation Induced Self-Assembly (EISA), Atomic-Layer-Deposition (ALD) and Focused-Ion-Beam (FIB) lithography, which we have applied in the fabrication of our novel solid-state nanopore array system.

### **1.1 Overview of the development in DNA sequencing**

The passage of individual ions/molecules through biological pores with nanometer-scale in membranes is essential to many processes in biology. The biological cells are assembled with all types of nanopores that actively control the trafficking of ions and molecules in and out of the cells to execute different functionalities. Two examples are ion channels and water channels in biological systems<sup>1-3</sup>. These natural biological channels all exhibit the characteristics of high flux and selective transport of specific ions or molecules. These unique features have inspired scientists to mimic these systems for a broad range of potential applications like water desalination, bioseparation and single molecule analysis, among which DNA sequencing has been considered as the most ambitious and significant application in the near future.

Since the first sequencing of the full human genome<sup>4, 5</sup>, genome-based medicine, such as drug discovery and medical therapies, has come closer to reality. As a result, there is imminent need for ultra fast and cheap methods for DNA sequencing analysis. Not only research laboratories will be able to sequence thousands of individual genomes during the development or clinical test phases of new drugs, but also individual medical consumers can be tested for the known genetic defects so that medicine and treatments can be tailored to their specific conditions. The present-day sequencing methods are the Sanger method<sup>6</sup> and several non-Sanger massively parallel approaches, which were recently commercialized in 2007 and have been described as “second generation” or “next generation”<sup>7-11</sup> sequencing (Genome Sequencer 20/FLX by 454/Roche, Basel; ‘Solexa 1G’ or ‘Genome Analyzer’ by Illumina/Solexa, San Diego; SOLiD<sup>TM</sup> system by Applied Biosystems, Foster City, CA, USA/Agencourt, Beverly, MA, USA; Polonator G0.007 by Dover Systems). In general, the Sanger sequencing process is composed of

four steps<sup>9</sup>: (1) DNA isolation; (2) sample preparation; (3) sequence production; and (4) assembly and analysis. In these four steps, step (2) is used to replicate the target DNA and break it into very short strands, while step (3) is used to detect the bases in the DNA sequence by combining three different procedures: first, chemical elongation creates labeled strands of DNA with the random insertion of a chain-terminating nucleotide; second, an electrophoretic process spatially separates the different lengths of DNA; finally, an optical readout detects the fluorescent end groups, which indicates the last base on each of the different lengths of DNA. Because electrophoresis which is involved in step (3) is sensitive to the physical difference between different lengths of single-stranded DNA, there exists a fundamental barrier to the maximum read length, i.e., the longest strands of DNA that can be sequenced accurately and efficiently. As a result, when the target DNA of sequencing is extremely long as for the human genome or mammalian genome, we expect very complex sample preparation and post-processing which dramatically enhances the cost in DNA sequencing. The development of “second generation” sequencing technologies had significantly reduced the cost of sequencing – from 1 cent for 10 bases to 1 cent for 1000 bases. However, these sequencing technologies all include an integral step of amplification of the target DNA by polymerase chain reaction (PCR), which means much of the time and cost required for DNA sequencing is expended in making and purifying many copies of these molecules to provide sufficient signal-to-noise ratios for fluorescence-based detection schemes. Amplification methods may also create several problems, e.g., the introduction of ambiguities resulting from contamination, from variability in amplification efficiency, and from other mechanisms not fully understood, the introduction of a bias in template



representation, and “dephasing” of the DNA strands due to loss of synchronicity in synthesis (i.e. different strands being sequenced in parallel)<sup>12</sup>.

There is no doubt that the cost, throughput and read-length are the three major issues in DNA sequencing in which cost reduction is especially in urgent demand because the prohibitive cost had become the burden for researchers to pursue new scientific enquiries. We have seen a more than 100-fold of cost reduction for a draft human-sized genome sequence from US\$ 24 million to US\$ 60,000 in the past a few years (“near-term” sequence goal) and anticipate another 100-fold cost reduction to ultimate US\$ 1,000 in next 5-10 years. Meanwhile, the read length has been increased from 12bp to 300bp from 1971 to 1977 and it was 1000bp in 2005.

Technology improvement and efficiency enhancement have a significant contribution to the above progress in DNA sequencing. The limitations of current sequencing technologies, as discussed above, open the door for researchers to pursue more promising technologies that provide faster and cheaper DNA sequencing. The so-called “US\$1,000 genome” project and many other inspiring programs funded by US National Human Genome Research Institute (NHGRI) give financial support in the research of new technology development aiming at cost reduction in DNA sequencing. Single-molecule sequencing (SMS), a so-called “third generation” or “next-next generation” sequencing technology, conducts direct analysis of single molecule which obviates the need for much of the upstream work like the amplification of target DNA, thus is anticipated to be much faster and cheaper than current DNA sequencing methods. Meanwhile, Single molecule methods may also provide unique gene expression

information by allowing analysis of nucleic acids from single cells, instead of averaging over many cells. Although this method was proposed as early as 1989<sup>13-15</sup>, it was not until 2008 that the first commercialized SMS instrument (HelioScope) was developed by Helicos Biosciences, Cambridge, MA using sequencing by synthesis (SBS) principle. It is still debatable if this “third generation” sequencing technologies will completely replace the other methods simply because most of the SMS are still at proof-of-concept stage. Table 1.1 compares the new-generation DNA sequencing platforms. It is more convincing to expect that, SMS technologies will either be the dominant DNA sequencing methods or co-exist with other technologies in the future.

Features	Second-generation sequencer			Third-generation sequencer (single molecule)			
	454- FLX	Solexa	Solid	Helicos tSMS	PacBio SMRT	Nanopore and modified forms	ZS Genetics TEM
Read-length (bp)	240- 400	35	35	30	100000	Potentially unlimited?	Potentially unlimited?
Cost/human genome (US\$)	1000000	60000	60000	70000	Low	Low	Low
Run time (h/Gb)	75	56	42	~12	<1	>20	~14
Ease of use	Difficult	Difficult	Difficult	Easy	Easy	Easy	Easy

**Table 1.1** A comparison of new-generation DNA sequencing platforms (Adopted from Gupta PK<sup>12</sup>)

From Table 1.1, it is clear that SMS has obvious advantages over existing sequencing technologies regarding cost, throughput and read length. Among all the SMS approaches like scanning probe microscopy, exonuclease sequencing, SBS<sup>16-20</sup> etc., the nanopore approach uses nanopores as detectors, which detect individual DNA properties

by pulling the DNA strand through a nanopore with comparable pore diameter and then measuring the changes in the ionic current through the pore caused by the DNA blockage. If nanopore sequencing can be achieved, it will provide several advantages including minimal sample preparation, sequence readout that does not require nucleotides, polymerases, ligases, or fluorescence labeling, and the potential of very long read-lengths and high throughput. Since Kasianowicz et al.<sup>21</sup> first detected DNA translocation through  $\alpha$ -hemolysin biological nanopores embedded in a lipid bilayer, the nanopore approach has been explored as the basis of technologies for single-molecule sequencing and analysis because of its promising features for faster and cheaper sequencing. Compared to other approaches, the nanopore approach holds some unique features:

1. They employ nanoscale probes to examine the structural or electronic signatures of individual DNA bases. That is, they rely on physical differences between the bases. This is a major departure from existing sequencing paradigms that rely on chemical techniques and physical differences between strands of DNA.
2. Nanopores can be designed in a way that their dimension is comparable to that of target DNA, so that for ssDNA to pass through this channel, the molecule must be straightened from its randomly coiled native state, with the individual nucleotides entering and exiting the channel in single file. This serial progression of the nucleotides through the nanopores makes the single-step analysis of unamplified DNA possible therefore becomes very attractive for direct DNA sequencing schemes.
3. The nanopore approach is easy to combine with other technologies, such as “hybridization”-assisted nanopore sequencing (HANS) and “Design polymer”-assisted

nanopore sequencing to facilitate single molecule detection; meanwhile, different methods, e.g. electronic (ion current measurement etc.), optical and force methods can be applied for DNA detection.

## 1.2 Physical Characteristics of DNA

### 1.2.1 DNA structure

Both deoxyribonucleic acid (DNA) and ribonucleic acid (RNA), two typical examples of polynucleotides with distinct biological function, are built up of repeated units of monomer (nucleotide), which consists of a base, phosphate group (PO<sub>4</sub>), and sugar. Double-stranded (ds) DNA helix is formed when bases of one polynucleotide pair with bases on correspondent positions of another polynucleotide by the Watson-Crick base pairing, following the rules that Adenine (A) pairs with Thymine (T) and Cytosine (C) pairs with Guanine (G) (for DNA) and with Uracil (U) (for RNA). One global property of polynucleotide is called *secondary structure*. For ds-DNA, for instance, there exist several different types of helices, in which the most common ones are called A-DNA and B-DNA. B-DNA is preferred in an aqueous environment because water molecules can bind in the grooves along the helix, while ionic and water environment can change the global structure of DNA between A- and B-DNA. The base-pair–base-pair distance in the B-DNA helix is 3.4 Å and there is a 36° angle between them, which gives about 10 bases per turn of the helix. The diameter of B-DNA is ~2 nm. Furthermore, there is a process called *denaturation* in which the two strands in ds-DNA unbind into two single-stranded (ss) DNA molecules under thermal and extreme pH conditions.

Single strands show the secondary structure of helices as well, which is mostly due to the interaction energy of base stacking. Another secondary structure is hairpin, a popular structure when part of the ss DNA/RNA can base-pair by itself to form a double strand. The double-stranded portion is called the stem and the unpaired portion is called a loop. There is no doubt secondary structure has huge effect on the dynamics of polynucleotide translocation through nanopores because of the structural difference with the random coil form<sup>22, 23</sup>.

### **1.2.2 Charge of DNA**

One of the most important properties of polynucleotides is that they are charged in solution. The *pKa* of the phosphate group, i.e., the measure of how readily that group will give up a hydrogen cation (proton), is near 1. Thus, under physiological pH, the backbone will contain a single negative charge for each nucleotide unit (or two negative charges for a Watson-Crick pair of nucleotides in a double strand). In ionic solution, though, there will be nearby counterions such as sodium (Na<sup>+</sup>), potassium (K<sup>+</sup>), or magnesium (Mg<sup>2+</sup>), which neutralize a part of this charge. By using optical tweezer and nanopore techniques, Keyser et al. determined that the effective charge for each nucleotide pair on the ds DNA is about 25% of its bare value, i.e., 0.5e instead of 2e in the range of ion concentration from 0.02M KCl to 1M KCl<sup>24</sup>. Nevertheless, polynucleotides are still regarded as highly charged polymers which can be easily driven by electric force.

### **1.2.3 Electric field**

One of the most important applications of the property of polynucleotides that they are charged in solution is that one can pull the DNA through nanopores with an electric field. As discussed earlier, the nanopore approach in DNA detection is under intensive investigation recently and maybe of significance in revolutionary DNA sequencing in the near future. Kasianowicz et al. showed that at 120 mV applied to  $\alpha$ -hemolysin biological nanopore on a lipid-bilayer membrane, a 210-base poly[u] blocks the channel current for about 1 msec<sup>21</sup>. Single stranded polynucleotide with this length has a diffusion coefficient of about  $3 \times 10^{-11}$  m<sup>2</sup>/sec in bulk water under normal conditions<sup>25</sup>. Using this coefficient for the diffusion in the pore and applying diffusion relaxation time formula with the pore length substituted by the nucleotide length, 30  $\mu$ sec for a characteristic time of a 'purely diffusional' relaxation is obtained which is 30 times smaller than the blocking time found experimentally. This result implies that strong polynucleotide/pore interactions exist for DNA translocation in nanopores with comparable pore size, which may be caused by many factors, such as the entropy energy barrier in nanopores formed from unraveling the polynucleotides. Therefore, by controlling the electric field applied on charged polynucleotides, the barriers in the pore during DNA translocation can be overcome.

More specifically, the charged polynucleotides have to be captured from the bulk solution to the pore and then be translocated through the pore. The capture of the polymer will depend on the diffusion of the polymer from the bulk to the pore and on local effects around the pore, such as the electric field and interactions between the entrance of the pore and the polymer. The capture rate will depend on concentration and applied bias<sup>26, 27</sup>

as well as what molecule is under investigation, and will have repercussions on the ability to detect and sequence. The translocation through the pore will be driven by the applied bias, but depends on many factors, including the polymer-pore interactions, ionic effects, and viscous drag.

#### **1.2.4 Elastic properties of polynucleotides**

Elastic properties of polynucleotides are important for understanding the translocation behaviors of DNA through nanopores because the nanopores force DNA to straighten out during translocation. In other words, the molecules with higher elasticity tend to be easier to translocate through the nanopores. The worm-like chain (WLC) model has worked well to explain the elastic properties of DNA molecule by treating it like a flexible rubber hose – the stiffer the molecule, the straighter it will be<sup>28</sup>. And the model assumes that each segment in the molecule obeys Hooke's law: the elastic restoring force is proportional to how much the molecule is bent. Because the elastic energy of DNA is comparable to the thermal energy that makes DNA “wiggle”, the DNA molecule is considered “soft”. Under physiological conditions, the persistence length of ds DNA is between 45 nm and 50 nm<sup>29</sup>, while the overall length varies from several hundreds of nm to micrometers. For ss DNA, at high salt concentrations, the persistence length goes down to between 0.8 nm and 1.3 nm, while at lower ionic strength, the molecule becomes stiffer and has higher persistence length<sup>30</sup>. The WLC model is limited in predicting how the elastic properties of DNA change with salt concentration.

Meanwhile, although the WLC model can perfectly explain the experimental results when forces on single DNA molecules are measured at length scales much longer



than the persistence length, it fails to predict the experimental results when the probed length is significantly smaller than DNA's persistence length<sup>31</sup>. Nelson and colleagues used high-resolution AFM to image the curvature of a large number of ds DNA molecules over distance as short as 5 nm and found that DNA is a lot more flexible than predicted by the WLC model<sup>31</sup>. Their analysis on these length scales suggests that the elasticity does not follow Hooke's law and they proposed a new general model (sub-elastic chain model) to explain the observed nonlinear elasticity. This new model implies that the elastic restoring force is constant when the molecule is bent on small length scales. It provides an insight into the nature and form of DNA elasticity at very small length scales, therefore helps us understand the behavior of DNA translocation through a variety of biological and synthetic pores at nanometer scales.

### **1.3 Coulter counter principle**

The coulter counter is a common resistive-pulse method that is widely used to size, identify, and determine the concentration of the analyte species. The coulter counter principle was first proposed by Coulter in early fifties<sup>32</sup>, who used an electrochemical cell in which a small aperture separates two ionic solutions, where electrodes are placed into each salt solution to measure the ionic current passing through the aperture. When a non-conducting particle suspended in a conducting medium passes through a small capillary/pore, it displaces a volume element of ionic solution equivalent to the particle volume in the capillary/pore, and therefore increases the resistance of the capillary/pore relative to that when the capillary/pore is filled with the conducting medium alone. This transient increase in aperture resistance is monitored via the corresponding increase in

transaperture voltage drop. The number of such voltage pulses reflects a count of the particles suspended in the electrolyte. The magnitude of this momentary voltage pulse is proportional to the volume of the particles in the aperture, and therefore provides information of particle size. Actually, the distribution of pulse amplitudes reflects the relative distribution of the volumes of the particle counted. Beckman Coulter product literature predict that an aperture can be used to detect particles with size in the range from 2% to 60% of the aperture diameter, in which the low size limit for a given aperture is determined by the electrical noise associated with the passage of the ionic current through the aperture (i.e. the magnitude of the voltage pulse has to be bigger than noise level to be detected), while the upper size limit is determined by the ability to keep the particle in suspension<sup>33</sup>.

Coulter-type resistive-pulse detector had been reported to size and count particles e.g. virus and bacteriophage as small as 60nm<sup>34</sup>. Since the diameter of the particles to be detected is in much degree determined by the diameter of aperture in use, there is no doubt coulter counter can be used to detect particles of much smaller size with the continuous development of technology of making smaller apertures. When the dimension of the aperture is comparable to that of molecules, molecule detection is possible. We call this advanced resistive-pulse detector as “molecular sensor”, to distinguish from the conventional coulter counter method.

#### **1.4 Molecular sensor**

As mentioned at the very beginning of this Chapter, scientists borrowed the interesting and challenging concept of molecule detection by the nanopore approach from

the protein channels made by Mother Nature. Because resistive-pulse sensing requires that the dimension of the aperture is comparable to that of the detected target, nanometer or even sub-nanometer size aperture is needed for molecule detection. With the development of nanopore technology, several platforms of biological nanopores and synthetic solid-state nanopores have been reported to meet this requirement and have been used in the exciting prospect of DNA translocation which can potentially lead to DNA sequencing in the near future. As the nanopore approach is the main focus of this dissertation and will be discussed in Chapter 1.5 separately, here I will introduce some general concepts that are related to molecular sensor.

#### **1.4.1 Single-Channel Recording**

As the dimension of nanopores has been reduced to nanometer-level which is comparable to that of molecules, single-channel current recording technology becomes significant to achieve improved time resolution and signal-to-noise ratio as compared to conventional coulter counter method. Single-channel current recording was achieved almost 40 years ago when planar bilayer recording was developed<sup>35</sup> and first applied in single-channel current measurement by Hladky and Haydon, who observed the opening and closing of individual channels formed by gramicidin A, a peptide antibiotic<sup>36</sup>. Then, the development of patch clamp technology with high-resistance (gigaohm) seals<sup>37, 38</sup> allowed single-channel recording from intact biological membranes, which minimizes the capacitive current associated with the larger area of a conventional planar bilayer and thereby improves time resolution and signal-to-noise ratio. Although protein pores had been widely used to detect and characterize polymers that produce channel blockage

since then, it was not until 1996 when Kasianowicz and his colleagues first observed the translocation of single polynucleotide (DNA and RNA) through a biological protein  $\alpha$ -hemolysin by single-channel recording that the application of resistive-pulse sensing had become a significant approach in single molecule detection. This is partly because of the significance of DNA sequencing/analysis in many critical research areas of human health, partly because  $\alpha$ -hemolysin provides a perfect size and configuration for DNA detection.

#### **1.4.2 Other molecular detection approaches**

I have to point out that, besides the nanopore approach by single-channel current measurement, many other approaches have been used for single-molecule analysis. Optical tweezers and traps<sup>39-44</sup>, steady shear flow<sup>45</sup>, combinations of optical trapping and mechanical actuators<sup>46</sup>, oscillating non-uniform electric fields<sup>47</sup>, magnetic tweezers<sup>48-50</sup>, biomembrane force probes<sup>51</sup>, atomic force microscopy (AFM) methods<sup>52, 53</sup>, single-molecule fluorescence detection<sup>54, 55</sup> and fluorescence resonance energy transfer (FRET) probes<sup>56</sup> have been used to study the mechanical properties of biological polymers<sup>57</sup>. Attempts to directly size or determine the composition of individual nucleic acid fragments have also been made by flow cytometry<sup>58</sup>, optical mapping<sup>59</sup>, and capillary electrophoresis (CE) separation with single-molecule detection<sup>60, 61</sup>. Fluorescence detection of single immobilized molecules has been used to detect specific sequences within a DNA strand<sup>62, 63</sup>, while FRET probes have been proposed as a possibility for direct sequencing<sup>64, 65</sup>.

I should point out that, many of the above approaches can be combined with the nanopore approach to improve sequencing technology as well as further investigate the

mechanisms of single DNA molecule during translocation through the nanopores. A novel device using optical tweezers<sup>66</sup> in conjunction with a nanopore had been demonstrated to slow the translocation of ds-DNA down by five order of magnitude compared to its free translocation rate, bringing it down from  $\sim 8$  mm/s to  $30$  nm/s<sup>24</sup>. Another proposed idea is to couple the optical method with nanopore ( $\alpha$ -hemolysin) for direct sequencing. Generally speaking, fluorescent labeled ds DNA is pulled into a small pore, when the double strand has to unzip into single strand. This pulls the fluorescent tag away from its quencher, therefore allows the tag, then the base in the original strand, to be detected via optical means<sup>67</sup>.

### **1.4.3 Size-related issues at molecular scale**

While particle-pore interaction hardly mattered in the case of conventional Coulter counter, it has to be taken into account when the pores go to the molecular scale. Steric, hydrodynamic, and electronic interactions are three major forms of particle-pore interaction and are all size-related. A straightforward geometrical consideration<sup>68</sup> shows that in the case when the particle radius is half the pore radius, the partition coefficient is reduced by a factor of four. For flexible polymers, since steric interactions are mostly related to the loss in the number of possible polymer configurations as a result of its confinement by the pore, entropic repulsion plays an important role in polymer partitioning into the pore and, therefore, in polymer transmembrane transport. Hydrodynamic interaction mostly results in a substantial decrease in diffusion rate when the particle and pore sizes are comparable. The significance of electrical interactions, which not only include Coulomb forces between fixed charges on the pore wall and on

the molecule, but also include van der Waals attractive forces and multiple electrostatic polarization effects, is also dramatically increased by the micron-to-nanometer scale transition.

## **1.5 Nanopore approach**

### **1.5.1 Biological nanopore approach**

Kasianowicz et al.<sup>21</sup> first demonstrated that an  $\alpha$ -hemolysin pore in a lipid membrane can be used to study the DNA translocation process. It features a transmembrane channel with restriction of 1.4 nm in diameter at its narrowest point which allows the passage of ssDNA with a diameter of 1.3 nm but not dsDNA with a diameter of 2 nm. Under the external voltage, highly charged ssDNA molecules can be driven through the nanopores in a linear single-file fashion. Because part of the liquid volume that carries the ionic current is occupied by ssDNA during translocation, the ionic conductivity is diminished by the passage of target molecules. Therefore, each current blockade event represents the passage of one ssDNA molecule through the pore, from which DNA information such as sequence would perhaps be allowed to be read off.

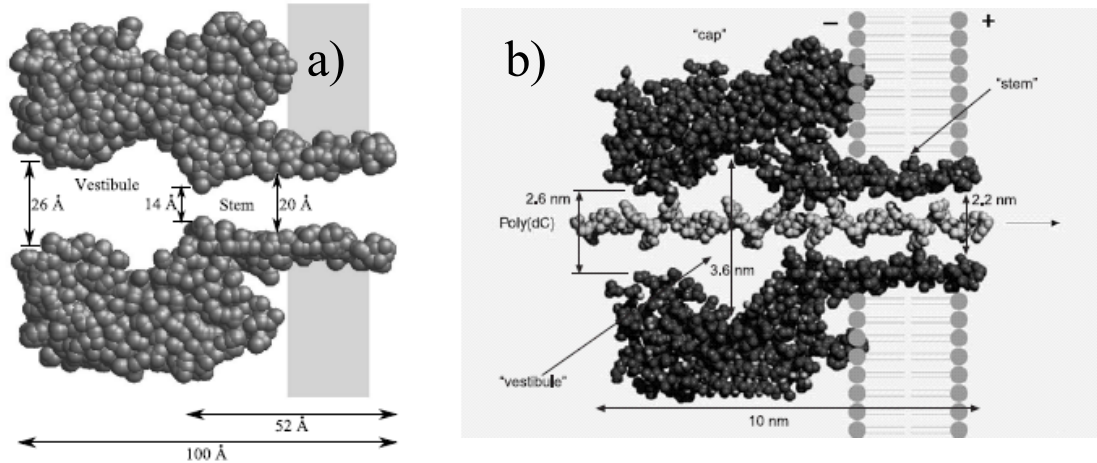


**Figure 1.1** a) Schematic of the  $\alpha$ -hemolysin pore adopted from Zwolak M et al.<sup>69</sup>; and b) Schematic of polynucleotide transport through  $\alpha$ -hemolysin nanopore (adopted from Meller A. et al<sup>70</sup>).

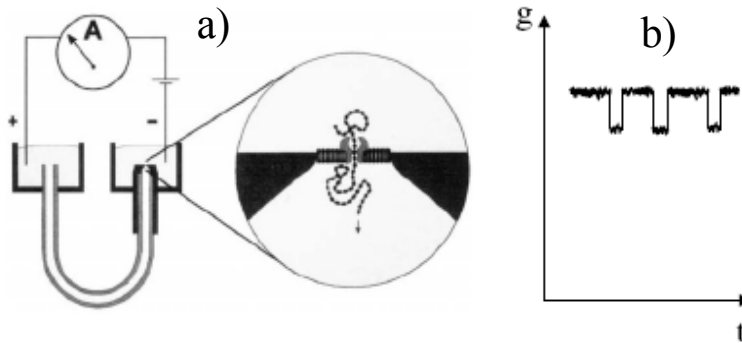


**Figure 1.2** a) A typical experimental setup for an  $\alpha$ -hemolysin pore in which the positive voltage is applied to the trans chamber and the negative voltage to the cis chamber (adopted from Akeson et al.<sup>22</sup>); and b) Current blockage signal recorded by amplifier during DNA translocation.

Some pioneering work has been done to test the hypothesis of the application of  $\alpha$ -hemolysin for direct sequencing<sup>22, 23</sup>. Although the current level differences between purine and pyrimidine ribonucleotides had been observed, unfortunately these easily

measured distinctions were due to the base stacking and other secondary structural differences between polyA and polyC oligomers, rather than the direct reflection of ribonucleotides themselves. Single nucleotide discrimination was still in question because the ionic current blockades are the consequence of 10-15 nucleotides rather than a single nucleotide that occupy the membrane-spanning domain of  $\alpha$ -hemolysin pores<sup>71</sup>.

Even though a nanopore cannot yet resolve the single bases with  $\sim 0.4$  nm distance in a DNA strand, it can be used to infer sequence with coarser-grained current-blockage information, in combination with sequencing by hybridization<sup>72</sup>. For de novo sequencing (basic concept of hybridization-assisted nanopore sequencing (HANS)<sup>73</sup>) where hybridization probes of known sequences are used to derive the sequence of an unknown ssDNA strand, we can use current blockade measurement from a nanopore that is large enough to translocate dsDNA to distinguish the passage of ssDNA from the passage of dsDNA. As a result, it may be able to detect and resolve the location and number of oligonucleotide probes that are hybridized to a long translocating ssDNA.

$\alpha$ -hemolysin had been extended to probe molecules besides nucleotides such as biotin-binding proteins with a biotin-labeled chain<sup>74</sup> and organic molecules with hydrophobic groups<sup>75</sup>.  $\alpha$ -hemolysin had been chemically engineered with modern molecular biology technologies such as mutagenesis<sup>76</sup> to extend its application. Scientists had also utilized  $\alpha$ -hemolysin's unique size that allows ssDNA translocation but rejects dsDNA to study the unzipping of ssDNA hairpins<sup>77, 78</sup> and ssDNA with a dsDNA end<sup>79</sup>. Other protein nanopores such as anthrax had also been reported for molecular translocation<sup>80</sup>.



### 1.5.2 Solid-state nanopore approach

Although the extensive research of biological nanopores on nucleotides translocation for its unique size compatible to certain molecules (like ssDNA), there are several drawbacks with biological pore approach: first, the 1.4 nm diameter at narrow part of lumen make its application restricted to ss-DNA; second, the lipid bilayer platform for protein nanopores requires very strict conditions regarding pH, salt concentration, temperature, mechanical stress, etc. therefore limits the applications in different device for potential commercialization. As a result, solid-state nanopores had emerged as an appealing alternative approach in nanopore family in recent years. To date, the guided etching of polymer films, focused ion beam sculpting, and electron-beam lithography and tuning of silicon nitride membranes have emerged as three promising approaches to define synthetic solid-state pores with sub-nanometer resolution. Li et al.<sup>81</sup> first used so-called “ion-beam sculpting” method and applied it to fabricate single nanopore with diameter as small as 3nm on SiN membrane. They demonstrated that such a solid-state nanopore microscope was able to detect the current blockade events of individual ds-DNA during translocation. Heng JB et al.<sup>82,83</sup> reported fabrication of single nanopore in 10nm thick Si<sub>3</sub>N<sub>4</sub> membrane by electron beam stimulated decomposition and sputtering using TEM operating at 200KeV. Storm AJ et al. claimed another solid-state nanopore fabrication method<sup>84</sup> by combining electron beam lithography, reactive-ion etching, wet chemical KOH etching and thermal oxidation to fabricate solid-state nanopores with any desired diameter. Siwy et al.<sup>85</sup> reported fabrication of conical pores on polymer films with 2 nm diameter at cone tip using the track etching technique. Chen P. et al.<sup>86</sup> declared that both nanopores and nanochannels can be used to probe single

DNA transport. Chang H.<sup>87</sup> claimed that by fabricating 50-60nm long, 4-5nm diameter nanochannels, the DNA molecules can be stretched out inside the channels so that the complex electronic signature of DNA moving through the channels due to conformational changes can be suppressed. Other materials that had been reported in published paper on DNA translocation include silica nanotube<sup>88</sup> and nanopore embedded in PDMS using micromolding techniques<sup>89</sup>. All these procedures have in common the formation of nominally cylindrical or conical pores aligned normal to the membrane surface and have successfully detected single DNA translocation events through the nanopore/nanochannel. Such materials offer many advantages such as tunable pore size and stability over a wide range of voltages, temperatures, pH, etc. as well as allowing the integration of different types of electronic/optical sensors or functionalization of the inner surface of the pore/channel.

Although solid-state nanopores have shown many advantages over the biological pores for single molecule detection, there remain some problems. First, fabricating a solid-state nanopore with a dimension comparable to that of DNA (2 nm and below) is difficult. It usually includes one or multiple steps of shrinkage of larger pores by irradiation under high energy source like electron beam etc. The many steps involved in nanopore fabrication and comparatively harsh processing conditions (E-beam etc) make it hard to predict the morphology of material in the vicinity of pore, pore structure (pore size, pore thickness and pore shape) and pore surface chemistry, therefore enhance the difficulty in getting reproducible solid-state nanopores for current blockade measurement. Second, many current research on DNA translocation by solid-state nanopore approaches reported a much higher DNA translocation velocity over biological nanopores approach

(~10mm/sec compared to <1mm/sec), which might be a burden for potential single base discrimination, as a higher translocation speed requires higher bandwidth for an electronic sensing system, a condition accompanying with higher electronic noise level. Finally, much of the preceding research on solid-state nanopores had focused on the development of single nanopore systems that display biological information. A related challenge arises in the engineering of materials for diagnostics and array technologies, in which large numbers of nucleic acids or proteins are presented in a format that allows rapid and highly parallel read out of biological information<sup>90</sup>. Due to the enormous number of applications that could potentially use parallel analysis, spatially patterned nanopore arrays have gained attention in recent years<sup>91</sup>. However, because the fabrication of solid-state nanopores, especially those in the nanometer level, requires the resizing of nanopores with ionic/electronic beam, an array of nanopores is typically fabricated in a ‘one-at-a-time’ manner which enhances the fabricating time and cost..

As a novel approach to conventional top-down solid-state nanopore fabrication, here I report a self-assembly approach to create an array of nanopores suspended over a silicon nitride aperture. Using a non-ionic surfactant to direct the formation of a porous silica mesophase, a periodic pore network array with pore orientations that deviate periodically from the surface normal is formed. Atomic layer deposition is used subsequently to adjust the pore diameter from 2.6 to 1.4-nm as well as alter the surface chemistry. In this dissertation I will demonstrate this novel fabrication of solid-state nanopore array made by evaporation-induced-self-assembly addresses some major issues encountered by conventional top-down solid-state nanopore approaches as described above; Meanwhile it exhibits some extraordinary features that are beneficial to potential

DNA sequencing and single-molecule analysis compared to other solid-state nanopore approaches and even biological nanopore approach. In the next three sections, I will give overall introductions of Evaporation-Induced-Self-Assembly (EISA), Atomic-Layer-Deposition (ALD) and Focused-Ion-Beam (FIB) lithography, three main methods to be applied in our approach to fabricate the novel nanopore array.

## **1.6 Concept of Evaporation-Induced-Self-Assembly (EISA)**

### **1.6.1 Surfactant-Directed Self-Assembly (SDSA)**

Since Kresge et al.<sup>92</sup> at Mobil first invented MCM41 mesoporous silica materials exhibiting highly ordered hexagonal arrangement of monosized mesopores in 1992, surfactant-directed self-assembly had been widely applied to make inorganic networks with a high degree of uniform porosity. A typical SDSA process of silica material is conducted in the aqueous solutions of soluble silica species in the presence of surfactants to initiate the spontaneous coassembly of silica-surfactant mesophases. Polymerized silica has high chemical and mechanical stability and is synthesized from silica precursors such as TEOS (tetraethyl orthosilicate) with aqueous, room temperature chemistry. Surfactant removal creates periodic mesoporous solids, potentially useful in catalysis and molecular transport.

Surfactants mentioned here are amphiphilic templating molecules serving as structure-guiding agents during inorganic network self-assembly. The dual nature of amphiphiles causes self-aggregation into dynamic micelles at concentrations above the critical micelle concentration (cmc). Hydrophobic tails are protected from water in the

interior of the aggregate, while hydrophilic head groups are at the surface. As surfactant concentration increases, we expect that local ordering, from lamellar sheet to arrays of cylinders occurs, which minimize surface area interaction caused by the increased repulsive forces between micelles. A so-called liquid crystal directed mechanism had been proposed to explain the formation of ordered silica mesophases in the presence of amphiphilic micelles: silica monomers and oligomers in the continuous solvent phase are present between the ordered aggregates, initiating the formation of silica/surfactant liquid crystal mesophase; further condensation and calcinations leave the rigid walls around template. Many surfactants had been used to template the synthesis of mesoporous inorganic network with various symmetries (lamella, 1D-hexagonal, 2D-hexagonal, 3D hexagonal, face-centered cubic, body-centered cubic, primitive cubic) and pore diameter (2nm-10nm). These surfactants include cationic surfactant such as cetyltrimethylammonium bromide (CTAB), nonionic surfactants such as  $C_{16}H_{33}(OCH_2CH_2)_nOH$ ,  $n \sim 10$  (Brij56),  $C_{16}H_{33}(OCH_2CH_2)_nOH$ ,  $n \sim 20$  (Brij58), and block copolymer such as  $EO_{20}PO_{70}EO_{20}$  (P123) and  $(EO)_{106}(PO)_{70}(EO)_{106}$  (F127) and anionic surfactant: sodium dodecyl sulfate (SDS).

### **1.6.2 Evaporation-Induced-Self-Assembly technique (EISA)**

Widely known as a simple and cost-effective method in preparing high quality thin film, evaporation-induced self-assembly<sup>93</sup> provides good control over the formation of silica mesophases through liquid crystalline templating. Starting with a homogeneous alcohol/water solution of hydrophilic silicic acid precursors plus surfactant with concentration far below the critical micelle concentration ( $c_0 \ll c_{mc}$ ), preferential



Compared to all other solid-state nanopore systems creating only straight-through pores, one distinctive feature of mesoporous thin film made by EISA is that pore connectivity of self-assembled nanopores is not necessarily straight through with respect to film surface. If the pore-to-pore connectivity can be represented by nodes connecting a series of rods, the adjoining rods of the same node sometimes have adjacent angle different from  $90^\circ$  and  $180^\circ$ , which means the pore-to-pore connectivity is tortuous. For example, the three dimensional model of well investigated Double-Gyroid (DG) biocontinuous structure derived from electron crystallography method clearly shows tortuous pore connectivity<sup>98,99</sup>. The study of kinetics pathway from hexagonal perforated lamellar (HPL) structure to Double-Gyroid (DG) structure shows adjacent angles of connected tripods in DG structure are  $70.53^\circ$ <sup>100</sup>. This tortuous pore connectivity in the self-assembled mesoporous thin films is more interesting because it is different from any current solid-state nanopore systems and possibly hosts some unique features that are beneficial for the single molecule analysis.

### **1.6.3. Functional mesoporous materials**

Besides the simplicity and cost-effectiveness of EISA as mentioned above, another advantage of EISA approach compared to other solid-state nanopore fabrication approaches is its availability to produce a lot of surface hydroxyl (-OH) groups on pore surface which can be used to covalently react with various functional groups for surface modification. One simple example is the incorporation of  $-NH_2$ ,  $-COOH$  contained ligands to change the charge density of pore surface. Also, Azobenzene-contained ligands (BSUA and TSUA) whose conformation is responsive to the external light stimuli

through the photoisomerization had been incorporated into the silica framework to demonstrate the light-induced control of mass transport of different ferrocene molecules<sup>101</sup>.

Figure 1.4 shows three kinds of surface –OH groups: single –OH, hydrogen-bonded –OH and geminal -OH<sup>102</sup>. For as-prepared mesoporous silica, there are 4-5 hydroxyl groups per nm<sup>2</sup> on the pore surface.

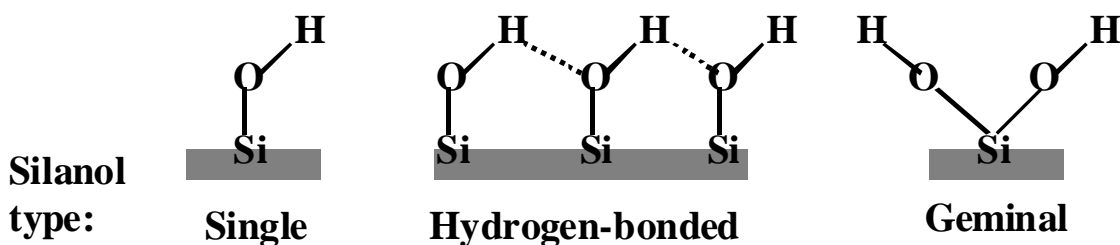


**Figure 1.4** Three types of –OH groups on the silica surface.

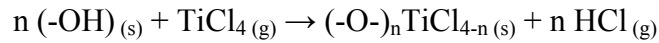
There are two methods to incorporate the functional group into mesostructured silica network: one-pot synthesis --- co-condensation reaction between organosilanes and inorganic precursors<sup>95, 96</sup>; and, post-synthesis modification covalent-bonding functional groups to the pore surface through coupling reaction between hydroxyl (–OH) groups on the pore surface and functional groups. Next, I will give a brief introduction of an advanced surface modification method --- Atomic-Layer-Deposition which is applied in this dissertation for fine tuning the pore size and surface chemistry.

### 1.7 Concept of Atomic-Layer-Deposition (ALD)

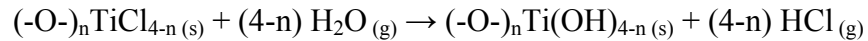


As discussed earlier, mesoporous silica thin films made by EISA provide plenty of –OH groups on the pore surface for surface modification. For a simple TiO<sub>2</sub> deposition on pore surface with TiCl<sub>4</sub> and H<sub>2</sub>O as precursors, it is believed that the reactions are as follow if we introduce TiCl<sub>4</sub> and H<sub>2</sub>O successively:

in TiCl<sub>4</sub> pulse:



in H<sub>2</sub>O pulse:

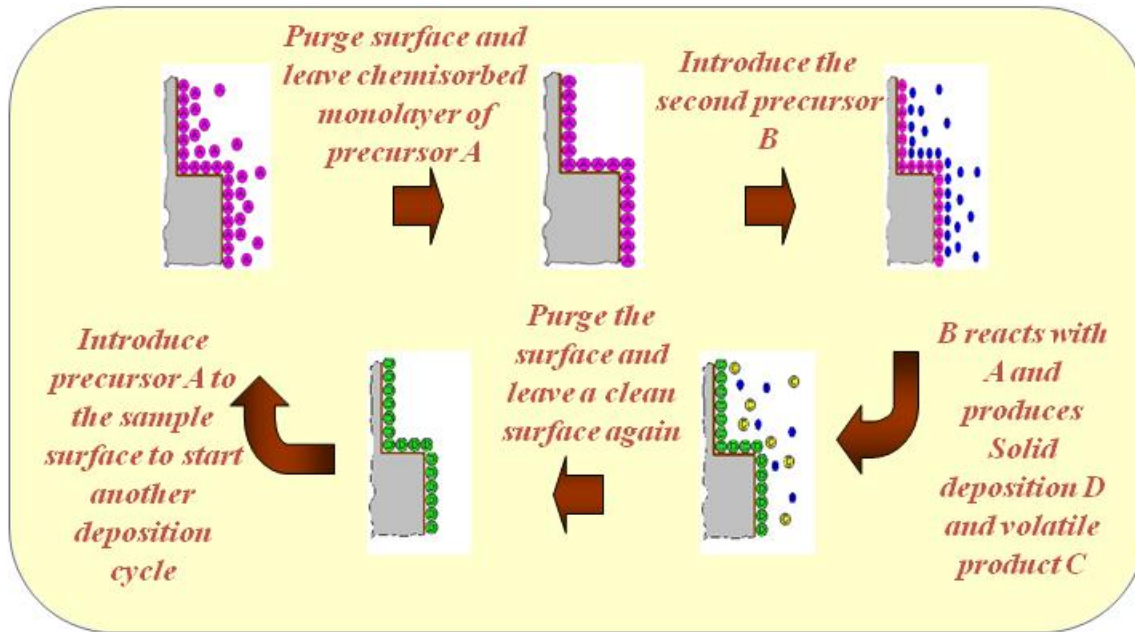


However, for traditional Chemical-Vapor-Deposition (CVD) approach, because two reactants are introduced into reaction chamber at the same time, most likely they will react each other before they even enter deeper inside the pores:  $\text{TiCl}_4 + 2\text{H}_2\text{O} \rightarrow \text{TiO}_2 + 4\text{HCl}$ . So we expect a thin film of TiO<sub>2</sub> formed on mesoporous film surface rather than inside the pores.

Different from traditional CVD, the reactant gases are introduced onto the sample surface successively during ALD process. The second precursor will not be injected into the reactor until the excessive free molecules of the first precursor are swept away by purging. The successive injections of precursors and the purging in between the injections guarantee that the deposition reactions only occur on the monolayer of precursors that chemically adsorbed on the surface. Since the gaseous precursors will adsorb on all pore surface, we expect to see homogenous film deposition deep inside the porous matrix on monolayer level.

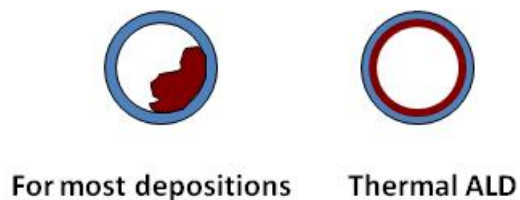
Therefore, ALD is a self-limiting, highly conformal, layer-by-layer deposition process that is extremely suitable for our mesoporous thin film structures to achieve pore size tuning at atomic level (Angstrom). Meanwhile, ALD appears to have several other advantages over traditional CVD: lower processing temperature; wider range of precursors; very thin thickness of the film; inherent 100% surface coverage with excellent conformality and lower impurity levels; smoother surface and higher quality.

Figure 1.5 shows the schematic of a typical thermal ALD process, which is comprised of the following major steps: 1) in a vacuum deposition chamber, a gaseous precursor “A” is introduced to the clean sample surface, forming several adsorption layers on the sample surface, where the first layer is the chemisorption layer and the following layers are the physisorption layers; 2) the chamber is purged or evacuated, and the weakly-bonded physisorption layers are swept away, leaving only the chemisorption layer, which is ideally one monolayer on the sample surface; 3) another gaseous precursor “B” is introduced to the sample surface, which will react with the chemisorbed “A” molecules, forming the desired solid deposition “D” on sample surface and may also producing some volatile product “C”; 4) the chamber is purged or evacuated again, to remove the excessive precursor “B” and any gaseous products, leaving a clean chamber and fresh sample surface that is ready for step 1 again. Steps 1~4, which is called one deposition chemisorbed cycle, may be repeated for a number of times thereby a thin film with accumulated thickness can be attained.



**Figure 1.5** Schematics of one cycle ALD to deposit a monolayer thin film on substrate.

For our mesoporous silica thin film with small pore dimension (sub 3 nm), ALD is an ideal method for surface modification and pore size tuning. Because there are plenty of hydroxyl groups on the surface of silica thin film, ALD is easy to start from the surface. Compared with other post-grafting surface modification methods in which precursors diffuse in liquid phase<sup>103</sup>, a ALD process allows vapor phase precursors to diffuse deeper inside the pores in a small pore system. Alternative introduction of the two precursors into the reaction chamber allows the precise control of pore size at angstrom level due to the conformal deposition on the pore walls. Meanwhile, The deposition temperature was set to medium temperature (150° - 180°C) to avoid the condensation of precursor molecules within nanopores at low temperature<sup>104</sup> as well as the decomposition of organosilane at high temperature<sup>105</sup>.



**Figure 1.6** Comparison of ALD with most other methods regarding the conformality of deposition inside the nanopores.

Plasma ALD, on the other hand, is a process where the reaction between the two precursors won't happen until it is irradiated by plasma. Different from thermal ALD with conformal deposition inside the pores, plasma ALD preferentially induces deposition near the pore entrance. Since conformal deposition inside the pores for surface modification and pore size tuning is the purpose of ALD process in this research, plasma ALD is not applied here.

### **1.8 Focused-Ion-Beam (FIB) lithography**

So far, numerous work had been conducted to integrate mesoporous thin films into porous substrates, especially Anodic-Aluminum-Membrane (AAM), so the molecular transport on the direction normal to the substrate surface becomes possible. While most research focused on the nanoscale confinement effect of substrate pores on cooperative assembly between inorganic and organic components of silica mesophases<sup>106</sup>,

<sup>107</sup>, some research had demonstrated that mesoporous structures integrated into porous substrates can be used for molecular transport. For example, integrating mesoporous structure with pore size of 3nm into AAM provides nanometer-order size-exclusive separation (allowing 2.4nm vitamin B12 to pass while excluding 4.0nm myoglobin) with promising throughput<sup>108</sup>. Also, Xomeritakis G. et al.<sup>109</sup> demonstrated that the mesoporous thin films deposited on home-made  $\alpha$ -Al<sub>2</sub>O<sub>3</sub> substrate with 0.2  $\mu$ m pore diameter by EISA may find application in ultrafiltration separation process. Meanwhile, the aerosol-assisted deposition of mesoporous thin film described by Xomeritakis G. et al. provides a new method to make smooth film structure on coarse-pore supports.

However, integrating mesoporous thin film into current commercialized porous supports like AAM is not a solution for the single molecule analysis purpose that we are interested here simply because the numerous nanopores on the substrate create very high overall ionic current which can easily exceeds the limit of current detecting apparatus. On the contrary, FIB lithography technology offers an option to drill a single pore with a wide variety of pore size on dielectric substrates like SiN<sub>x</sub><sup>110</sup>. Depositing mesoporous thin film above a single aperture made by FIB dramatically limits the number of nanopores serving for molecule transport, thus avoids the overloading issue and allows us to detect distinctive electronic signals that are representative of the molecule translocation events through the nanopores.

## **1.9 Problem statement**

In this chapter I have briefly introduced the development of DNA sequencing technology. Also, I have pointed out three major challenges encountered in current DNA

sequencing: cost, throughput and read-length, in which cutting the cost has become the main drive for the development of many new sequencing technologies, such as SMA. As a comparatively new SMA method, the nanopore approach has drawn more attention lately for its promising features for faster and cheaper sequencing. However, biological nanopores have to face challenges like low stability and difficulty to integrate into devices, while most solid-state nanopores have encountered issues like very fast DNA translocation speed and difficulty in making very small single nanopores or nanopore arrays with sub- 2nm dimension. As had been mentioned before, slowing down DNA translocation speed inside the nanopores is critical for the potential single base discrimination with the nanopore approach<sup>111</sup>, as a higher translocation speed requires higher bandwidth for an electronic sensing system, a condition accompanying with higher electronic noise level. Therefore, finding a simple solid-state nanopore fabrication approach that exhibits reduced DNA translocation speed is of interest for the potential application of the nanopore approach in DNA sequencing.

Meanwhile, inspired by the exquisite selectivity and flux demonstrated by natural biological channels, achieving the selectivity of synthetic solid-state nanopores by precise controlling pore size and surface chemistry of engineered nanopores is of interest for many practical applications like DNA separation/purification, but is still a big challenge for most current synthetic solid-state nanopore systems.

## **Chapter 2**

### **Goals and Objectives**

The overall goal of this research is the synthesis and characterization of a novel solid-state nanopore array by combining our expertise in Evaporation-Induced-Self-Assembly (EISA) with other fabrication capabilities like Focused-Ion-Beam (FIB) lithography and Atomic-Layer-Deposition (ALD), which allow us to precisely control the combination of pore size, shape, charge and surface chemistry needed to mimic natural nanopore systems, as well as allow straightforward integration into fluidic platforms needed for gating, separation and detection of specific molecules like DNA. Through the combination of bottom up synthesis and top down fabrication, this doctoral dissertation attempts to achieve several objectives. In particular,

1. Design, synthesis and characterization of a robust, free-standing nanopore array by a simple self-assembly procedure to direct the size, shape and tortuosity of an array of solid-state nanopores;
2. Further physical and chemical modification of the above nanopore array by conformal ALD of an oxide or silane to reduce uniformly the diameters of all pores or change the surface chemistry;
3. Integration of the above nanopore array into fluidic platforms for the convenience of practical applications like single molecule sensor.

With full investigation and understanding of the above novel nanopore array system, we attempt to utilize its unique features to address some of the critical issues in DNA sequencing and DNA separation/purification. In particular,

1. Investigation of the influence of pore size and pore shape of our nanopore array system, especially the tortuous pore shape that is different from all other reported nanopore systems (biological and solid-state nanopores) on DNA translocation to address the important issue of reducing translocation speed in DNA sequencing;
2. Demonstration of an efficient two-step approach (nanopore array fabrication with further pore size modification by conformal ALD) to exhibit nearly perfect selectivity for ssDNA over dsDNA.



## Chapter 3

### Experimental

#### 3.1 Material Preparation

##### 3.1.1 Reagents and Materials

Surfactants:

non-ionic surfactant Brij 56,  $\text{CH}_3(\text{CH}_2)_{15}(\text{OCH}_2\text{CH}_2)_n\text{-OH}$ ,  $n \sim 10$ , Aldrich

Silanes:

tetraethylorthosilicate (TEOS, 99.999%),  $\text{Si}(\text{OC}_2\text{H}_5)_4$ , Aldrich

2-cyanoethyltriethoxysilane (CTES) (97%),  $\text{CNCH}_2\text{CH}_2\text{Si}(\text{OC}_2\text{H}_5)_3$ , Aldrich

aminopropyl trimethoxysilane (APTMS) (97%),  $\text{NH}_2\text{CH}_2\text{CH}_2\text{CH}_2\text{Si}(\text{OCH}_3)_3$ , Aldrich

Substrates:

Si wafer: (from silicon valley microelectronics Inc.) N/phos (type/dopant), (100)

(orientation), 1-50  $\Omega\text{-cm}$  (resistivity), 475-575  $\mu\text{m}$  (thickness)

$\text{Si}_3\text{N}_4$  membrane: (from SPI; West Chester, PA) 200 nm-thick, low stress  $\text{Si}_3\text{N}_4$  films

(window of 0.25 mm x 0.25 mm) adhered to silicon substrates of 200  $\mu\text{m}$ -thick

##### 3.1.2 Synthesis of ultra-thin mesoporous silica film

Prior work in our group used Brij 56 under acidic conditions to direct the formation of supported cubic nanoporous silica membranes characterized by an  $\text{Im}\bar{3}\text{m}$  body-centered symmetry and Barrett-Joyner-Halenda (BJH) pore diameter of

approximately 2.6-nm<sup>96</sup>. Here, we adopted the same recipe but diluted 8x in ethanol, yielding the final Si : Brij56 : EtOH : HCl : H<sub>2</sub>O molar ratio 1.28 : 0.076 : 248 : 0.09 : 71. The mixed sol was aged for ~120 minutes and then deposited on silicon substrates or porous substrates by spin-coating (at 1000 RPM for 1 min) or aerosol deposition at room temperature (22.5°C). Figure 3.1 shows schematic of aerosol deposition setup. After 24 hours of film deposition, the surfactant molecules in the mesostructured films were removed by calcinations in 400°C oven for 1 hr. Other critical condition influencing film formation includes humidity. The film deposition was conducted under constant humidity of 30% in a glove box which was connected to a Nitrogen gas source and a humidifier.

### Ultrasonic Aerosol Deposition Setup

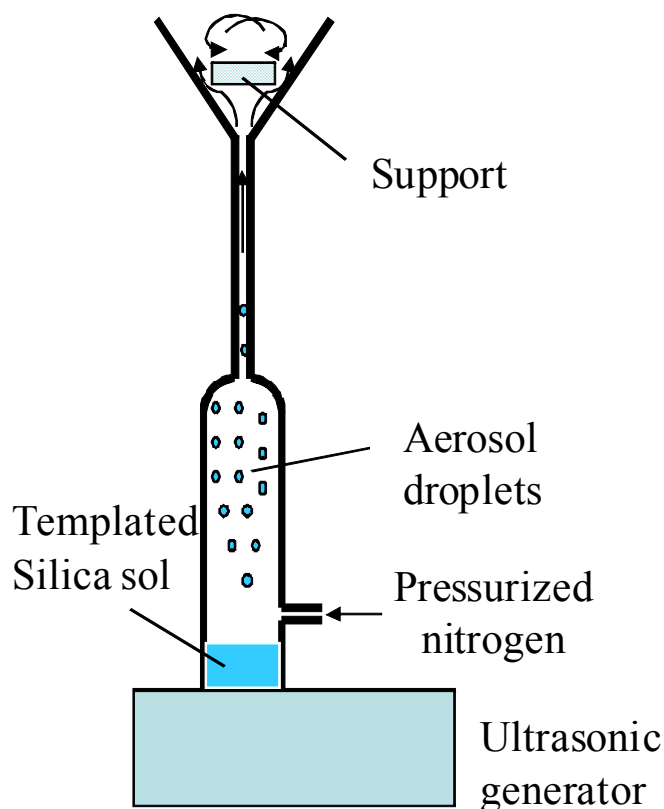


**Figure 3.1** Aerosol deposition set up (adopted from Xomeritakis, G. et al.<sup>109</sup>)

### 3.1.3 Atomic-Layer-Deposition (ALD) to fine tune the pore size and surface chemistry

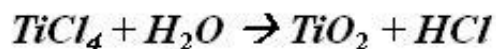
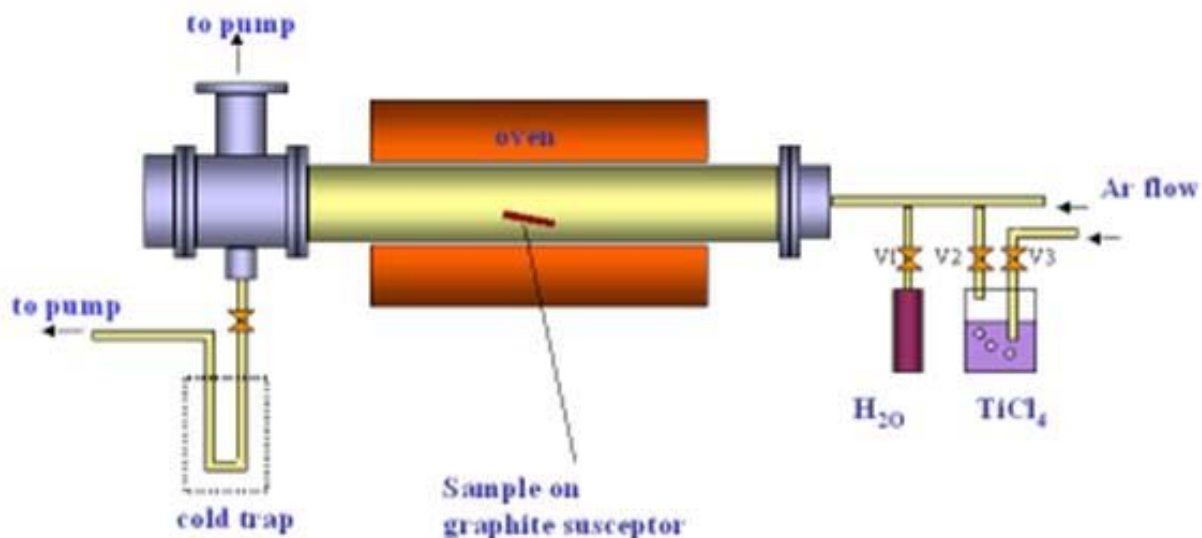


**Figure 3.2** Schematics of ALD set-up for deposition of  $\text{TiO}_2$  using  $\text{TiCl}_4$  as precursor. We also used the same ALD setup to form a coherent aminopropyl silane monolayer using the molecular precursor aminopropyl trimethoxysilane (APTMS). Deposition temperature is  $150^\circ\text{C}$  and the reaction time is comparatively longer than  $\text{TiO}_2$  deposition.

The ALD deposition experiments were carried out in an Angstrom Thermal ALD system designed by Angstrom Thin Film Technologies (see Figure 3.2). The deposition chamber was a Pyrex glass chamber, evacuated to a base vacuum of  $0.5 \times 10^{-3}$  Torr. A  $\text{N}_2$  cold trap was installed between the pump and the deposition chamber to trap corrosive precursors as well as to eliminate the backflow of pump oil vapor. Heated precursors reservoirs were mounted at the upstream of the system and precursor vapors were delivered into the reaction chamber by Ar carrier gas. The deposition temperature was set to medium temperature ( $\sim 180^\circ\text{C}$ ) to avoid the condensation of precursor molecules

within nanopores at low temperature<sup>104</sup> as well as the decomposition of organosilane at high temperature<sup>105</sup>. Before the deposition, samples were kept at 180°C under vacuum condition for 4 hrs for outgas to obtain a clean sample surface prior ALD. Then, vaporized precursor and water were introduced into the reaction chamber sequentially with a reasonable reaction time and separated by 15 sccm Ar purge. These two steps (referred as one cycle) were repeated to obtain multilayer deposition.

### 3.1.4 Focus-Ion-Beam (FIB) lithography to fabricate sub 100nm single pore on SiN substrate

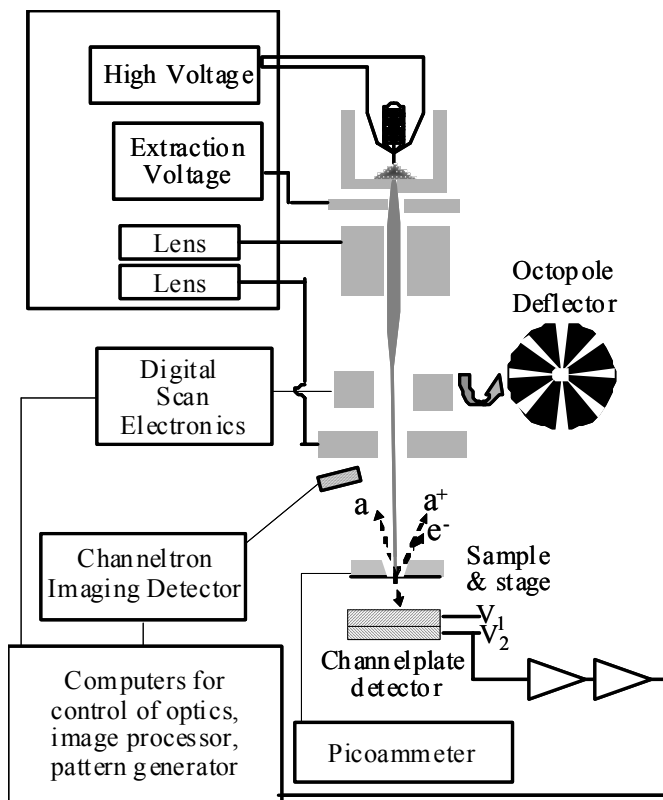


**Figure 3.3** Experimental setup for FIB (adopted from Patterson et al.)<sup>110</sup>.

To drill nanopores on SiN substrate, we used a dual lens, ion-pumped Magnum FIB column (FEI, Co.; Hillsboro, OR), accompanying BC-100 electronics/software, and a custom target chamber. The target chamber is diffusion pumped to a base pressure of  $7 \times 10^{-8}$  Torr and contains a grounded sample stage, channeltron electron imaging detector and model APD 3040MA 12/10/8 D backside microchannelplate detectors (Burle Industries, Inc.; Lancaster, PA) as shown in Figure 3.3. A loadlock chamber is adjoined to the target chamber so to minimize pumpdown time after sample introduction.

The specimens consist of 200 nm-thick, low stress  $\text{Si}_3\text{N}_4$  films (Structure Probe, Inc.; West Chester, PA) adhered to silicon substrates. The focused ion beam-entry side of the specimen is sputter coated with 400 Å W in order to prevent charging effects.

Nanopores are drilled at the center of 250  $\mu\text{m}$ -wide windows (coated with W) after correcting for astigmatism and focusing. A single pixel contained within a 5-10  $\mu\text{m}$  field-of-view is bombarded with a 1, 10, 30 or 50 pA beam of 30 keV Ga ions. The working distance (from the beam exit aperture of the ion column to sample) is 30 mm, and the distance from the sample to the front surface of the backside channelplate detector is 43 mm.

The detector front plate is biased to  $-1500$  V ( $V_1$  in Fig. 3.3) and the back plate ( $V_2$ ) is grounded. It is contained on the movable x-y stage but is isolated from this grounded apparatus. A model PMT-4 preamplifier/amplifier (Advanced Research Instruments, Corp.; Golden, CO) is located external to the vacuum chamber and is connected through a 2  $\frac{3}{4}$ " conflat flange. The amplifier boosts the signals provided by the microchannelplate detector prior to sampling by a Model 6035E data acquisition card (National Instruments; Austin, TX).

## **3.2 Material Characterization**

Here we list all material characterization methods with a brief description for each method.

### **3.2.1 Transmission Electron Microscopy (TEM)**

TEM was performed on a JEOL 2010, operating at an accelerating voltage of 200 kV and equipped with a Gatan slow scan CCD camera. TEM samples were prepared by scraping the film with a sharp blade and transferring the flakes to a carbon-coated copper grid.

For cross-sectional TEM image observation, two identical 3mm x 10 mm bars were cut from the same original sample and then were glued together with epoxy face to face (i.e. thin film sides of each bars are in touch with each other by the epoxy). The glued sample was baked at 70°C overnight and sliced along the direction normal to the sample interface into small specimen by a diamond saw. The small specimen was then mechanically polished along cross-section direction until the thickness is below 15 micron. After that, the thinned specimen was glued to TEM copper grid and ion milled with a Gatan 600 A ion miller starting with 5 keV ion energy followed by gradually reduced ion energy when the specimen became thinner and thinner. When the color of the final specimen turned red under optical microscope, the sample was thin enough for TEM observation.

Imaging was performed in under-focus conditions. For TEM observation of thin films on FIBed customer-ordered SiN membrane, a special-designed TEM holder where the membrane can glue was used.

### **3.2.2 Scanning Electron Microscopy (SEM)**

A **Hitachi S-5200** Ultra-high resolution, in-lens SEM with resolution of 0.5 nm at 30 kV and 1.7 nm at 1 kV was used to observe plan-view or cross-sectional nanostructures on solid or porous substrates with maximum magnification 2,000,000 X. SEM was coupled with PGT Spirit EDS system with image mapping capability.

### **3.2.3 Thermal analysis**

Thermogravimetric Analysis (TGA)/Differential Thermal Analysis (DTA) were performed on Perkin-Elmer 7000 instrument using air, oxygen or argon as the processing atmosphere and a heating rate of 2 °C/min to characterize thermal stability of the organic compounds in mesoporous silica thin film.

### **3.2.4 N<sub>2</sub> adsorption/desorption isotherms of thin films**

Surface acoustic wave (SAW) technique was used to measure the nitrogen adsorption isotherms of thin film structures for porosity and pore size distribution (PSD) estimation. Nitrogen adsorption isotherms were collected using an in-house designed 96MHz surface acoustic wave (SAW) apparatus interfaced with a Micromeritics ASAP 2020 surface area and porosimetry analyzer. Thin Films were deposited on SAW substrates to measure the frequency shifts of the SAW device configured as the feedback element of an oscillation circuit during adsorption and desorption of nitrogen. The amount of nitrogen adsorbed as a function of relative pressure was determined from the frequency change, assuming that the SAW frequency is only perturbed by a mass loading variation. Nitrogen adsorption/desorption isotherms at 77 K were obtained by plotting the

amount of nitrogen adsorbed vs. the corresponding relative pressure of nitrogen. Surface areas, pore size, and pore size distributions were estimated using the BET equations and the Barrett-Joyner-Halenda (BJH) model.<sup>112</sup>

### **3.2.5 Ellipsometry**

A multi-wavelength spectroscopic ellipsometer (J. A. WOOLLAM CO. INC., model EC110) using a Cauchy dispersion model was applied to measure the thickness and refractive index of the films. All refractive index values (reported at a wavelength of 632.5 nm) and thickness measurements were made in triplicate and averaged to obtain the data points reported herein.

### **3.2.6 Fourier-Transform Infrared (FTIR) spectroscopy**

For FTIR studies, films were deposited onto undoped silicon substrates and analyzed in a transmission geometry using a Nicolet model 800 infrared spectrometer equipped with a mercury cadmium telluride (MCT) detector.

### **3.2.7 Grazing Incidence Small Angle X-Ray Scattering (GISAXS)**

GISAXS measurements were performed at the Advanced Photon Source at Argonne National Laboratories using a wavelength of 1.6868Å, a sample-to-detector distance of either 1580 or 1254 mm, and a 2048 x 2048 Marr CCD detector. Reflectivity measurements were used to position the sample angle in the range above the critical angle of the film but below that of the substrate, the criterion for grazing incidence; typical analysis angles were 0.18-0.20°. NANOCELL<sup>113</sup>, a program developed at Purdue



University for analysis of SAXS and GISAXS data of nanostructured materials, was used to fit the resulting 2D scattering data.

### **3.2.8 X-Ray Diffraction (XRD)**

X-ray diffraction (XRD) was performed on a PANalytical X'pert Pro system equipped with an X'Celerator detector.

### **3.2.9 Pt deposition experiment**

Electrochemical deposition of Pt was accomplished through Potential Step Voltammetry (Electrochemistry Powersuite PARSTAT2272, from Princeton Applied Research Co.) of a 0.1 M solution of  $\text{H}_2\text{PtCl}_6$  (duty cycle of 0.000 V vs. Ag/AgCl for 5 seconds followed by -0.300 V vs. Ag/AgCl for 10 seconds) inside nanoporous films deposited upon a Pt or fluorine-doped tin oxide electrode using the same synthesis procedure used for producing films for DNA translocation experiments. A three electrode system composed of Pt or fluorine-doped tin oxide substrates (as working electrode), a Pt flat sheet (as counter electrode) and a Ag/AgCl wire (as reference electrode) was mounted in a home-made electrochemical cell device to conduct the experiment. The electrochemical deposition of Pt controlled by pulse voltammetry mode was continued until the charge was accumulated to 0.075C.

### **3.2.10 Contact angle measurement**

A video contact angle system (VCA 2000, AST Inc.) was used to measure the contact angle of water on the surfaces of mesoporous thin films.

### 3.3 DNA translocation experiments

#### 3.3.1 DNA design

There are a few prerequisites when we choose the DNA in our experiments: 1) for dsDNA, because our pore size range (sub 3nm) only allows linear phase of DNA to pass through the pores, we need to use specific digest enzyme to cleavage the DNA if they come in circular forms; 2) for ssDNA, we use homopolymers such as poly(dA)<sub>100</sub> in order to avoid duplex, hairpin and other forms of secondary structures; 3) we will be able to get DNA with different length so that we can investigate the DNA translocation characteristics as a function of polymer length<sup>70, 71, 114</sup>.

We used pUC19 vector (a commonly used plasmid cloning vector of double-stranded circle with 2,686 pairs in length) and  $\Phi$ X174 RF I ( double –stranded, covalently closed, circular form with 5,386 base pairs in length) ordered from New England Biolabs. The digest enzymes used to cleavage the above circular DNA were also ordered from the same company. Normally we use EcoR1 with one specific digest site on pUC19 to cleavage into a linear dsDNA with 2,686 base pairs in length (using 1.5  $\mu$ l enzyme for each 5  $\mu$ g DNA in 50  $\mu$ l of reaction system, 5 $\mu$ l NE buffer was also added before filled with DI water).

For  $\Phi$ X174 RF I, we had used Xmn I enzyme which has three restriction sites along circular form to cleavage DNA into three sizes of fragments (4126bp, 974bp and 286bp).

The agarose gel electrophoresis stained with ethidium bromide showed three clearly separated bands with lengths consistent to the correspondent restriction sites,

indicating successful cleavage of  $\Phi$ X174 RF I into three fragments with different lengths. To collect DNA fragments of different lengths, we cut the gel into three pieces under UV light so each piece only contained one DNA fragment. Then we used QIAquick gel extraction kit (from Qiagen) combining with microcentrifuge to extract and purify DNA fragments from agarose gel.

Besides the above DNA cleavage approach using restriction enzyme, DNA fragments with specific lengths can also be obtained by Polymer-Chain-Reaction (PCR) amplification which has the following advantages: 1) by specifically designing the primers (forward and reverse) for PCR reactions, we can obtain DNA with any lengths; 2) PCR amplification allows us to produce DNA fragments with comparatively large amount; 3) because PCR amplification avoids the step of DNA separation using agarose gel electrophoresis, especially the step of staining DNA with ethidium bromide, the resulting DNA fragments have higher purity than those made by DNA cleavage approach.

We used pUC 19 plasmid as the DNA template to make dsDNA with different lengths. First, we designed the forward and reverse primer following the rules as below: 1) primer length 18-25 bp; 2) GC content 40-60%; 3)  $T_m$  of the two primers should not differ more than 5°C; 4) one primer should not be complementary over greater than 3-4 bases to any region of other primer (or even the same primer). Some oligomer manufacturing companies provide primer design service on their website (like IDT). Public software like mfold can be used to check the complementary bases within one primer or between two primers. However, to ultimately determine if the designed primers are appropriate, gel electrophoresis after PCR amplification has to be run. A single band on electrophoresis corresponding to the expected polymer length is the only way to prove

the successful design of the primers as well as the amplification of DNA fragments with identical lengths. Otherwise, either the forward and/or reverse primers are not designed appropriately or the PCR conditions are not the optimum conditions.

Second, optimum PCR conditions have to cope with the specific PCR process (depends on the DNA template, pre-designed primers, etc) to obtain DNA fragments with high purity. The optimum PCR conditions in our experiments are determined as:

- 1) 94C 2min (initial denaturation);
  - 2) 94C 30sec (cycle denaturation);
  - 3) 60C 30sec (primer annealing);
  - 4) 68C 1min (primer extension);
- repeat step 2-4 for 34 cycles
- 5) 68C for 5min (substrate clearance).

Based on the above principles, we successfully made dsDNA fragments with the lengths of 270bp and 950bp with pUC19 plasmid as the DNA template, as evidenced by the sole DNA band after agarose gel electrophoresis. A 100bp ladder from New England Biolabs was used to determine the length of the sole DNA fragment. Forward and reverse primers were ordered from IDT. AccuPrime Taq DNA polymerase kits were ordered from Invitrogen for PCR amplification. PCR amplifications were conducted in a Peltier Thermal Cycler (PTC-200, MJ Research) from MJ research. After PCR amplifications, QIAquick PCR purification kits from Qiagen were used to purify dsDNA from amplification reactions.

To demonstrate ssDNA translocation through our nanopore array system, we used 150b ssDNA with a sequence described in Kasianowicz's paper<sup>21</sup>. After DNA

translocation experiment, the solution from –trans side was collected and sent for PCR amplification using pre-designed primers. Then gel electrophoresis was conducted to determine if a sole band appeared at 150b position.

All DNA solutions were store at -20°C for storage.

### **3.3.2 DNA solution**

Concentrated ssDNA and dsDNA solutions were in TE solution (10 mM Tris, 1 mM EDTA, pH8.0) for storage.

Before DNA translocation measurement, concentrated ssDNA and dsDNA were diluted in the autoclaved buffer solution (10 mM Tris-HCl, 1 mM EDTA, 1M KCl, pH 8.0) to the required concentrations (2 nM for dsDNA and 2 µg/ml for ssDNA). Then the diluted DNA solution was loaded in –cis chamber and buffer solution was loaded in –trans side before DNA translocation. The concentration of DNA solution was determined by Nanodrop 3300 from Thermo Scientific.

For gel electrophoresis, TBE buffer were used to dissolve agarose from which gel network was made.

### **3.3.3 Patch clamp instrumentation**

Data acquisition system of the patch clamp recording is composed of patch clamp amplifier (Axonpatch 200B), Digitizer (Digidata 1440A), Filter (Model 2582—dual pass 8-pole Bessel filter), Oscilloscope, Faraday cage (FC-0 model), Computer with pCLAMP 10 software, Headstage with Ag/AgCl Electrodes, Micromanipulator, Isolation table, and Microscope. The electrical and magnetic noise and vibration noise from the floor can be

screened using the Faraday cage and isolation table. The Headstage and Electrodes are placed in the Faraday cage. The signal from the Electrodes is acquired into the computer through the following route: Headstage→ Patch clamp amplifier → Filter→ Digitizer→ Computer. The signal can also be monitored using the Oscilloscope.

### **3.3.4 Electrochemical cell device**

The membrane with nanopore array is mounted into a novel electrochemical cell device before DNA translocation experiment. The electrochemical cell is made of teflon and composed of two separate chambers with capacities up to 1 ml. As shown in Figure 3.4, the membrane is mounted between the two chambers in a way that the window on the membrane where mesoporous thin film was spanning aligns with the holes on both chambers through identical axis so that molecules from one chamber can go to the other chamber through the membrane. The chamber with DNA solution is called –cis side and the chamber with buffer solution is called –trans side. Two O-rings are placed on each side of the membrane during membrane mounting to achieve tight sealing. Ag/AgCl electrodes connected to an amplifier (Axopatch 200B, Axon Instruments, USA) are placed in both chambers to give the applied voltage and measure the ion flux across the membrane.

### **3.3.5 Experimental procedure**

Before the SiNx membrane with nanoporous array is mounted between the two chambers and sealed with O-rings, the film is treated with an oxygen plasma for a short time to fully hydroxylate its surface, and then rinsed in isopropanol for 20min. DNA

solution is placed in –cis side and buffer solution is placed in –trans side. Ag/AgCl electrodes connected to an amplifier (Axopatch 200B, Axon Instruments, USA) are placed in both chambers to measure the ion current at applied voltages ranging from 120mV to 500mV (Figure 3.4). Current signal is digitized at 200KHz (1440A digitizer) and low-pass filtered with a cutoff frequency of 10KHz. Before performing DNA translocation measurements, we wait for the current to become stable. All experiments were run under room temperature.

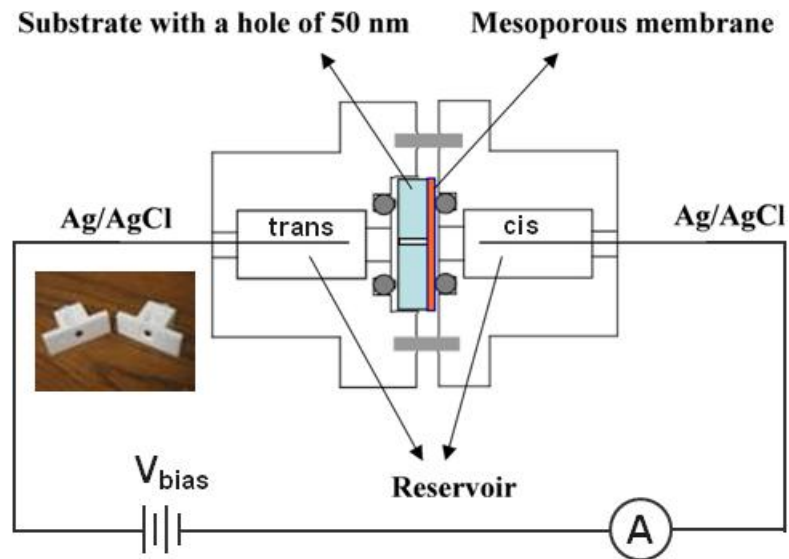


**Figure 3.4** Schematic of electrochemical cell for performing voltage driven DNA translocation experiments. Inset photo shows two half cell device.

## **Chapter 4**

### **Results and Discussion I: Fabrication of nanopore array by EISA**

In this chapter, our main focus is on the fabrication of our unique solid-state nanopore array platform that will be applied to DNA translocation. Therefore, critical issues related to DNA translocations such as thin film symmetry, pore size distribution and pore trajectory will be addressed in this chapter by a wide variety of structure characterization methods.

#### **4.1 Synthesis and characterization of ultrathin mesoporous silica film with Brij 56 as surfactant on a solid substrate**

As described in the experimental chapter, ultrathin mesoporous silica film was obtained by adopting the recipe of bcc thick film developed in our group<sup>96</sup> with 8x dilution of original sol by ethanol. With regard to DNA translocation, thin films are important because: 1) a shorter contour length increases the likelihood that the channel is continuous and spans the membrane; 2) decreased thickness provides a greater field strength within the membrane, thereby imparting greater momentum to DNA in overcoming the potential of mean force needed to translocate the pore; 3) modification of the pore surface by post-grafting or atomic layer deposition (ALD) becomes more efficient when the contour length of the channel is shorter.



### 4.1.1 X-ray diffraction

As shown in Figure 4.1a X-ray diffraction data shows that interplanar d-spacing of our ultra-thin silica film is reduced after template removal by calcination, indicating significant uniaxial film shrinkage along the direction perpendicular to the substrate surface. The periodic interference fringes observed in the XRD data indicate the extreme thinness and homogeneity of the film. Film thickness derived from interference fringes data is estimated to be 28 nm, as shown in Figure 4.1b.

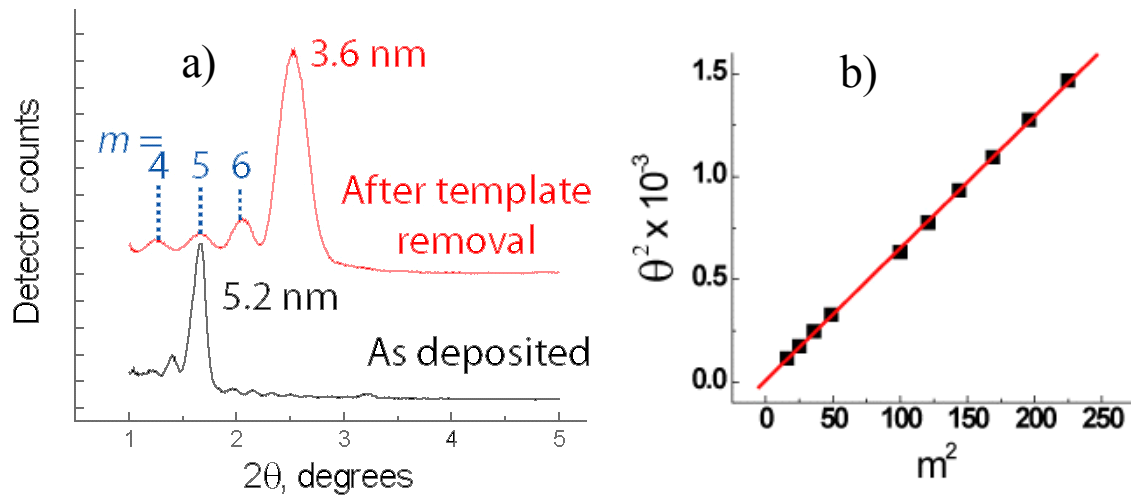


**Figure 4.1** a) XRD data before and after removal of the Brij 56 template by calcination, showing the Bragg reflection shifted after calcination (5.2 nm before calcinations and 3.6 nm after calcinations) due to the uniaxial film shrinkage along the direction perpendicular to the substrate, as well as interference fringes (order labeled in blue) arising from the extreme thinness of the film; b) Data derived from interference fringes, showing the plot of  $m^2$  vs.  $\theta^2$  used to estimate the film thickness, with  $m$  being the reflection order.

### 4.1.2 GISAXS characterization of ultra-thin mesoporous silica film

Grazing-incidence small angle x-ray scattering (GISAXS) was used to characterize the structure of the periodic thin film mesophase. In GISAXS, a x-ray beam is incident upon a sample at an angle greater than the critical angle of the film but less than that of the substrate (typically ca.  $0.2^\circ$ ), maximizing the scattering volume of the beam within the film. Use of a 2D detector enables collection of both in- and out-of-plane scattering data for comparison of the pattern to a hypothesized nanostructure<sup>113</sup>. Figure 4.2 contains typical GISAXS data for a ca. 30 nm film synthesized in an identical manner to the films used for DNA translocation experiments. We find data consistent with the presence of two separate but related mesophases: a [001]-oriented face-centered orthorhombic phase with unit cell parameters  $a = 82 \text{ \AA}$ ,  $b = 122 \text{ \AA}$ , and  $c = 73 \text{ \AA}$ ; this unit cell is an equivalent description of a [110]-oriented  $Im-3m$  (body-centered cubic, bcc) phase with  $a = 82 \text{ \AA}$ , contracted by ca. 37 % in the direction perpendicular to the substrate from uniaxial film shrinkage<sup>115, 116</sup>, and a [001]-oriented 3D hexagonal  $P6_3/mmc$  with unit cell parameters  $a=b=67 \text{ \AA}$  and  $c = 73 \text{ \AA}$ . The in-plane domain size was estimated through line width analysis to be 200 nm and 125 nm for the  $Fmmm$  and  $P6_3/mmc$  phases, respectively. These unit cell parameters, along with typical Brij 56 micelle dimensions (ca. 4-5 nm), conform to the existence of micellular-type (as opposed to minimal surface) bcc and hexagonally close-packed (hcp) mesophases.

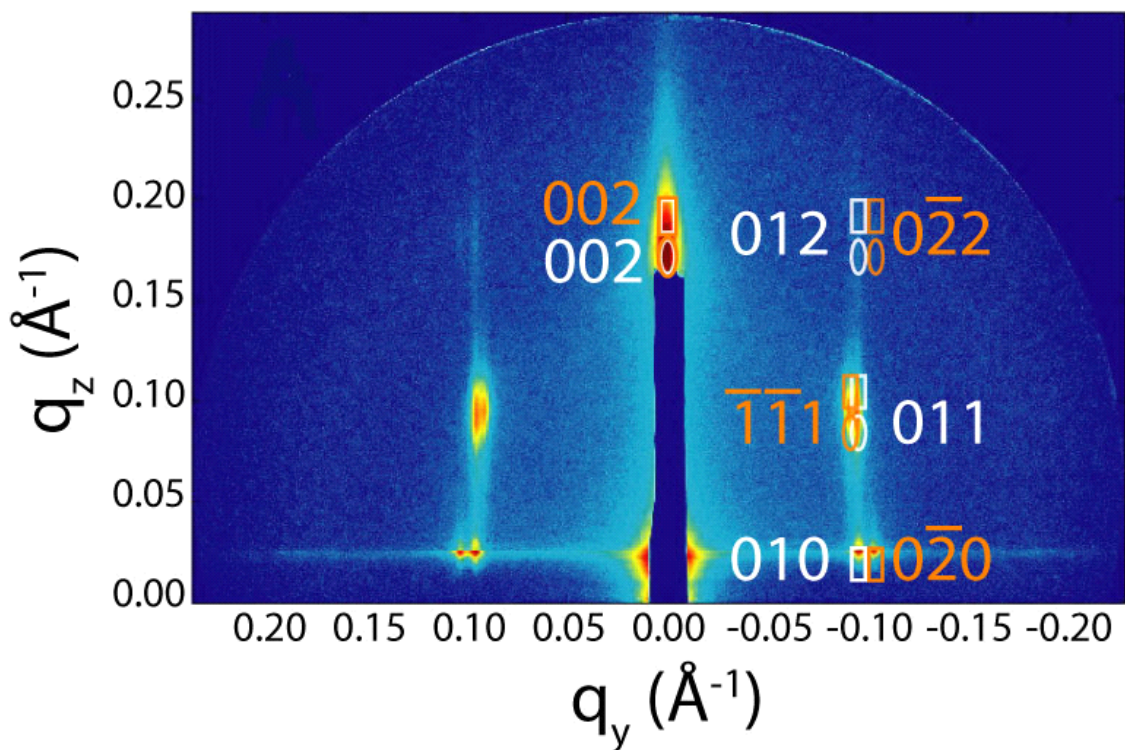


**Figure 4.2** Typical 2D GISAXS data for a self-assembled porous silica film (ca. 30 nm thick) as used for DNA translocation experiments, showing the presence of two phases, described by  $Fm\bar{3}m$  (in orange) and  $P6_3/mmc$  (in white) symmetry. Unit cell parameters are given in the text. Ovals and rectangles signify the predicted positions of diffraction from the incident and reflected beam, respectively.

Figures 4.3 contain an illustration of the  $Fm\bar{3}m$  unit cell (**a**), as well as a schematic of the overall DNA translocation pathway through the film (**b**). Although the precise shape and connectivity of pores within the film is not known, we place a sphere at each lattice point of the  $Fm\bar{3}m$  structure that corresponds to bcc packing to represent the likely positions of pores, and connect these pores in (**b**) using the standard eight-fold bcc coordination of each lattice point. The shortest pathway through the film, highlighted in red, presents a tortuosity of ca. 1.5 (the whole pore length divided by film thickness).

DNA translocation through other pathways is unlikely as the electric field is strongest in this direction. Also, pore connectivity of pathways parallel to the plane of the film may be limited due to larger pore-to-pore spacing.

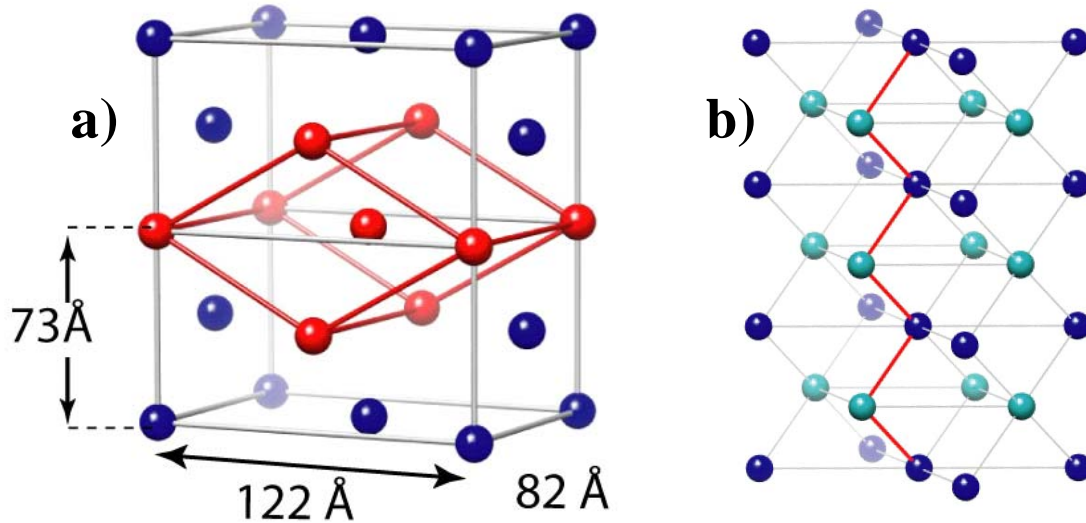


**Figure 4.3** a) Two unit cells of the *Fmmm* phase, showing the unit cell dimensions determined from the fit to the GISAXS data in Figure 4.2 as well as the relationship of *Fmmm* to the “distorted” *Im-3m* unit cell (shown in red); b) Schematic of the [001]-oriented *Fmmm* phase, showing lattice points (here representing the positions of pores) in alternate planes signified by color and the 8-fold coordination characteristic of bcc packing indicated by grey lines. The shortest kinked pathway through the lattice is labeled in red.

The unit cell for the [001]-oriented hcp phase (space group  $P6_3/mmc$ ) simulated in Figure 4.2 is shown in Figure 4.4a, along with a schematic of the overall DNA translocation pathway through the film (b). Again, although the precise shape and connectivity of pores within the film is not known, we place a sphere at each lattice point of hcp packing to represent the likely positions of pores, and connect pores in (a) using

the standard twelve-fold coordination between lattice points found in hcp packing. The related hcp structure has the same tortuosity of ca. 1.5 (shown in red in Figure 4.4b) as *Fmmm* structure, indicating DNA passes through an identical pore length through the film thickness in both *Fmmm* and *P6<sub>3</sub>/mmc* mesophases.

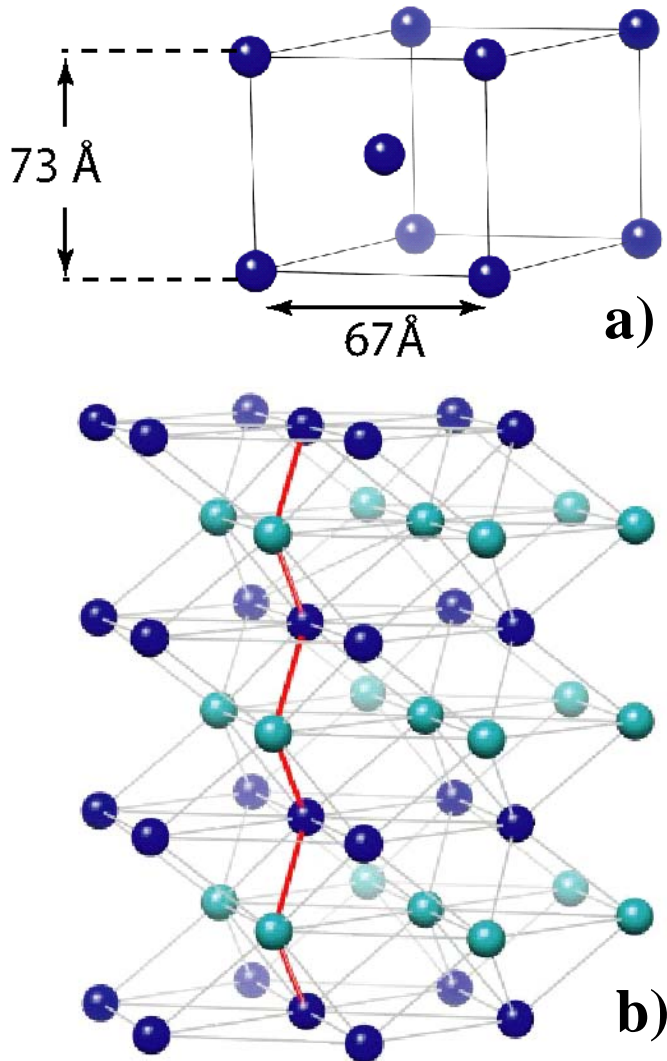


**Figure 4.4** a) Unit cell dimensions for the hcp phase fit to the GISAXS data in Figure 4.2. b) Schematic of the [001]-oriented hcp phase, showing lattice points (here representing the positions of pores) in alternate (001) planes signified by color and the 12-fold

coordination characteristic of hcp packing indicated by grey lines. A direct pathway through the lattice is labeled in red.

To further verify that the observed *Fmmm* and hcp mesophases are related, we run GISAXS experiments for a thicker (300 nm) Brij 56 templated film synthesized under similar conditions as used for ultrathin films. As shown in Figure 4.5, the scattering pattern is indexed to the space group *Fmmm* with unit cell parameters  $a=82\text{\AA}$ ,  $b=116\text{\AA}$ , and  $c=64\text{\AA}$ , with the *c* axis perpendicular to the substrate. This is consistent with distorted bcc packing of micelles, aligned with [110] perpendicular to the substrate, with  $a = 82\text{\AA}$  and ca. 45% shrinkage along the *z*-axis. In-plane line width analysis shows a feature width limited by the resolution of the GISAXS instrumentation, indicating a lower bound for domain size of ca. 600 nm. Along the *z*-axis (through the thickness of the film), a lower limit of the packing domain size is estimated to be 125 nm. Also present in this GISAXS image is a diffuse halo; from the position of this halo along the *y*-axis ( $q < q_{\text{bcc}}$ ), we posit that this diffuse scattering arises from defects in the bcc phase that indicate a nascent transformation to hcp. This transformation becomes more and more obvious when we keep reducing film thickness by diluting the original sol with ethanol, as evidenced by the final two separate *Fmmm* and hcp mesophases in the ~30 nm thick films. XRD data of ~30 nm thick film (Figure 4.1) shows only one set of Bragg peaks (with  $d = 36\text{\AA}$ ), reinforcing the presence of identical interplanar spacing for the two related structures found inside this film.

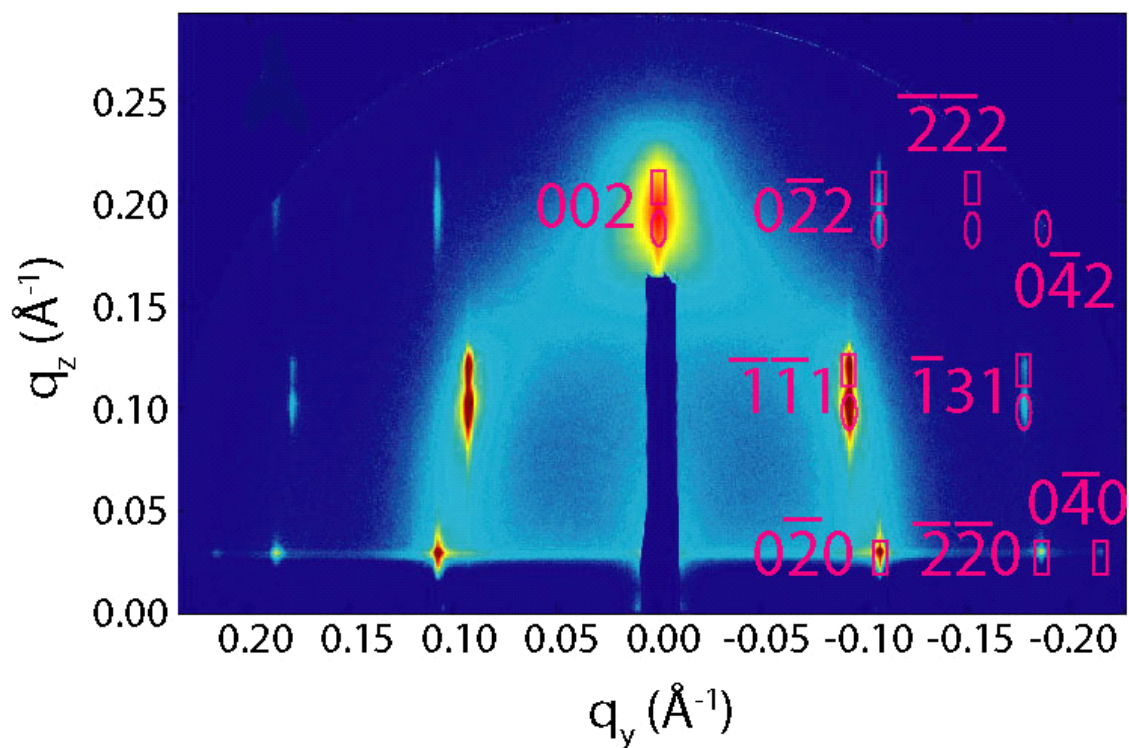


**Figure 4.5** Typical GISAXS data for a self-assembled porous silica film (ca. 300 nm thick), showing the presence of a highly-oriented predominantly *Fmmm* phase (distorted bcc) along with a diffuse scattering ring arising from domains that are not highly oriented with respect to the plane of the substrate or from regions with globular micellar packings with structural order intermediate to distorted bcc and hcp structures. Ovals and rectangles signify the predicted positions of diffraction from the incident and reflected beam, respectively.

For experimental convenience, the face-centered orthorhombic (fco) space group *Fmmm* was used to simulate the bcc phase in both thin and thick nanoporous films<sup>117</sup>; this space group can describe [110]-oriented bcc taking into account the uniaxial shrinkage perpendicular to the substrate seen in all EISA-derived films that results from drying stresses as well as silica condensation during film processing.

Finally, as illustrated in Figure 4.6, a diffusionless transformation model is applied to relate bcc and hcp packing<sup>118</sup>. Although it is uncertain if the hcp phase seen in our ultrathin nanoporous films is derived from the bcc phase in this manner, the identical interplanar spacing between the two structures, as well as the relative orientation of the bcc and hcp lattice, are consistent with this mechanism. The hcp phase obtained by this transformation is not true hcp in the sense that  $c/a \neq 1.57$ ; this distortion is further intensified by drying and condensation stresses during film assembly and template removal. Also, the micelles in this phase are not close packed. Nonetheless, we use the label ‘hcp’ as the pore arrangement and packing type (AB stacking of 2D hexagonal planes) are identical to true hcp.



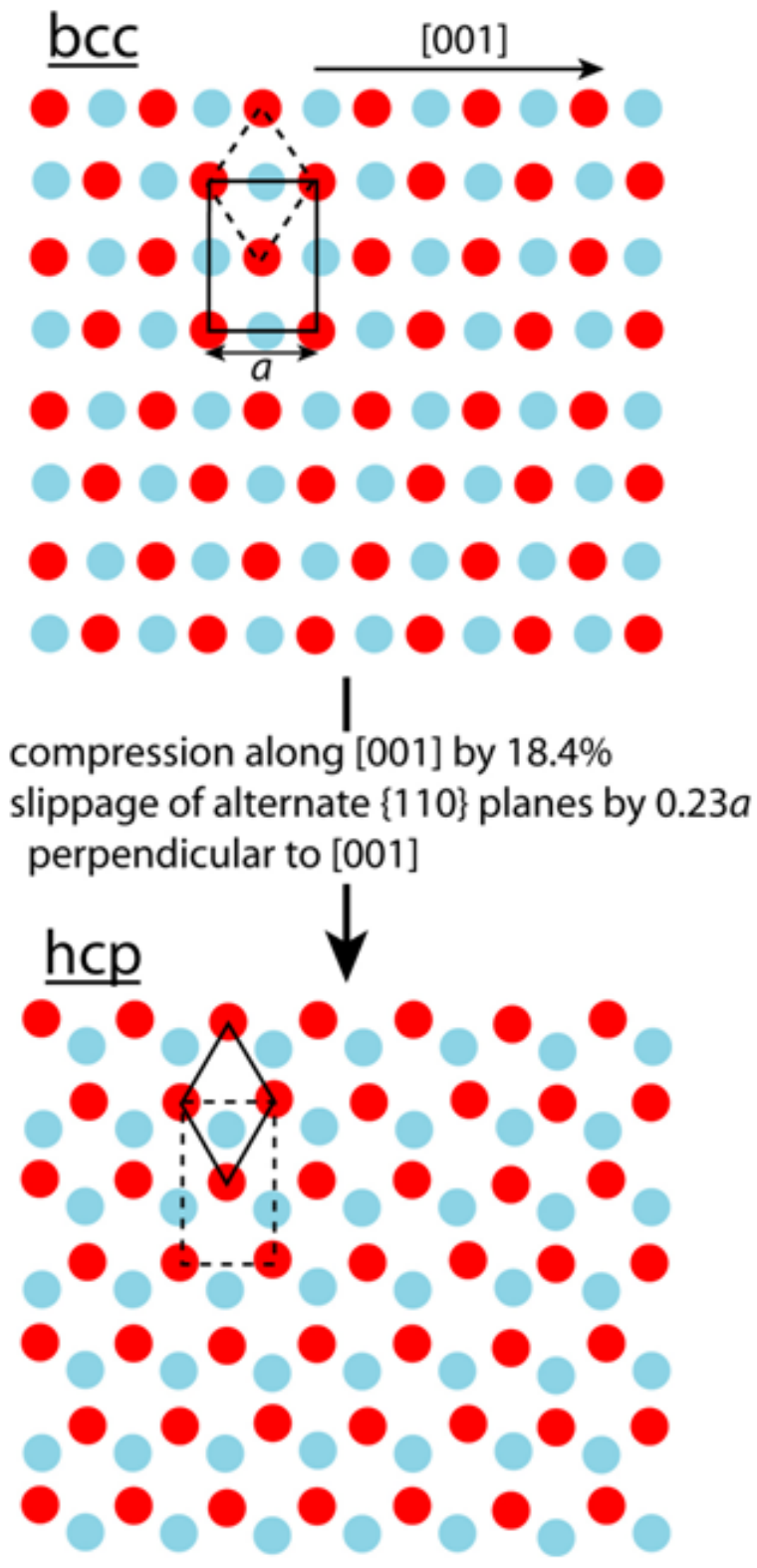


**Figure 4.6** Schematic of the relationship between bcc and hcp packing (plan view) as described in the text. Rectangular and hexagonal unit cells are outlined in black to clarify the relation between the two structures. Note that the red sites are in the plane while the blue sites are  $0.5 b$  lower in the  $b$ -direction.

### 4.1.3 TEM

Figure 4.7 and figure 4.8 contain the TEM cross-sectional and plan view images of a film prepared in an identical manner as to the film analyzed in Figure 4.2. The plan view in Figure 4.8 shows the (001) plane of the  $Fmmm$  structure; the unit cell parameters  $a$  and  $b$  calculated from the fast fourier transform (see inset) are 8.4 nm and 12.1 nm respectively, consistent with results simulated from GISAXS data. Also the  $a/b$  ratio is close to the  $1:\sqrt{2}$  in-plane ratio that is described by the (001) plane of our  $Fmmm$  thin film structure<sup>115, 116</sup>. Consistent with GISAXS analysis, plan view TEM images of hexagonal (the (001) plane of  $P6_3/mmc$ ) or mixed packing were also observed (see Figure 4.9). The cross section in Fig. 4.7 shows the (110) plane of the  $Fmmm$  structure, with an overall film thickness of ca. 30 nm (the most likely tortuous pore pathway through the film is highlighted in black). Interplanar distance measured from cross-sectional TEM image is 3.7 nm, consistent with d-spacing value obtained from XRD data (Figure 4.1) and  $c/2$  value from GISAXS data (figure 4.2).

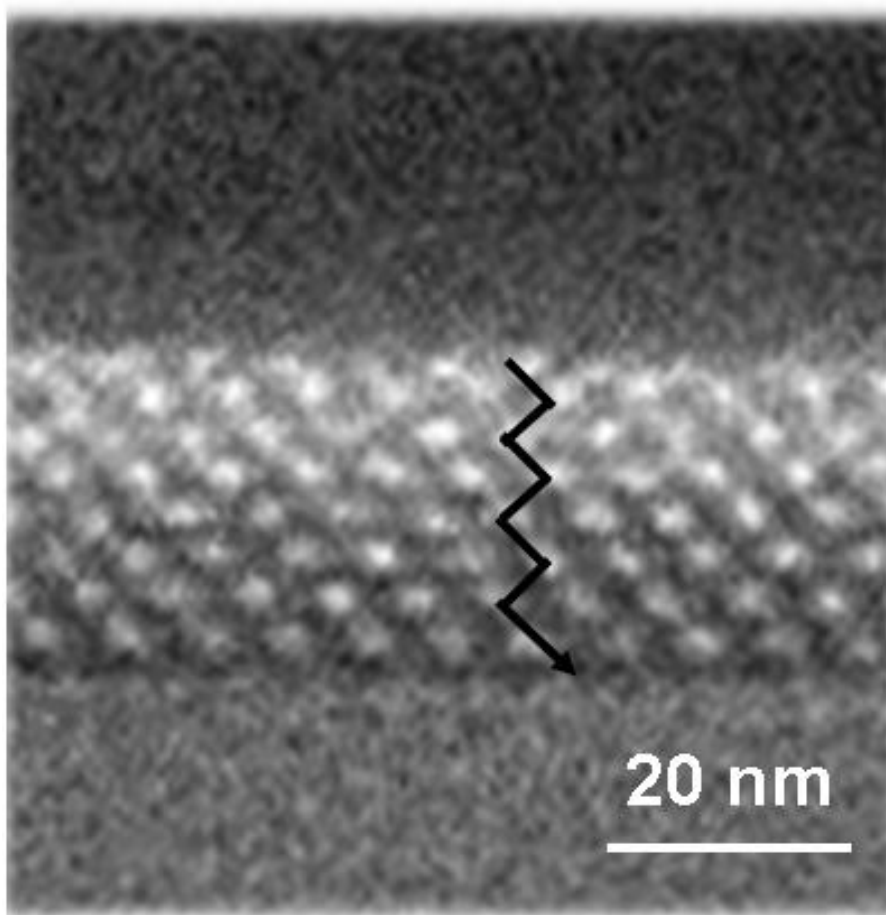


**Figure 4.7** TEM cross-sectional image along [110] for an *Fmmm* mesoporous film, deposited on an oxidized silicon substrate and calcined at 400°C, suggesting a kinked pore pathway through the film.

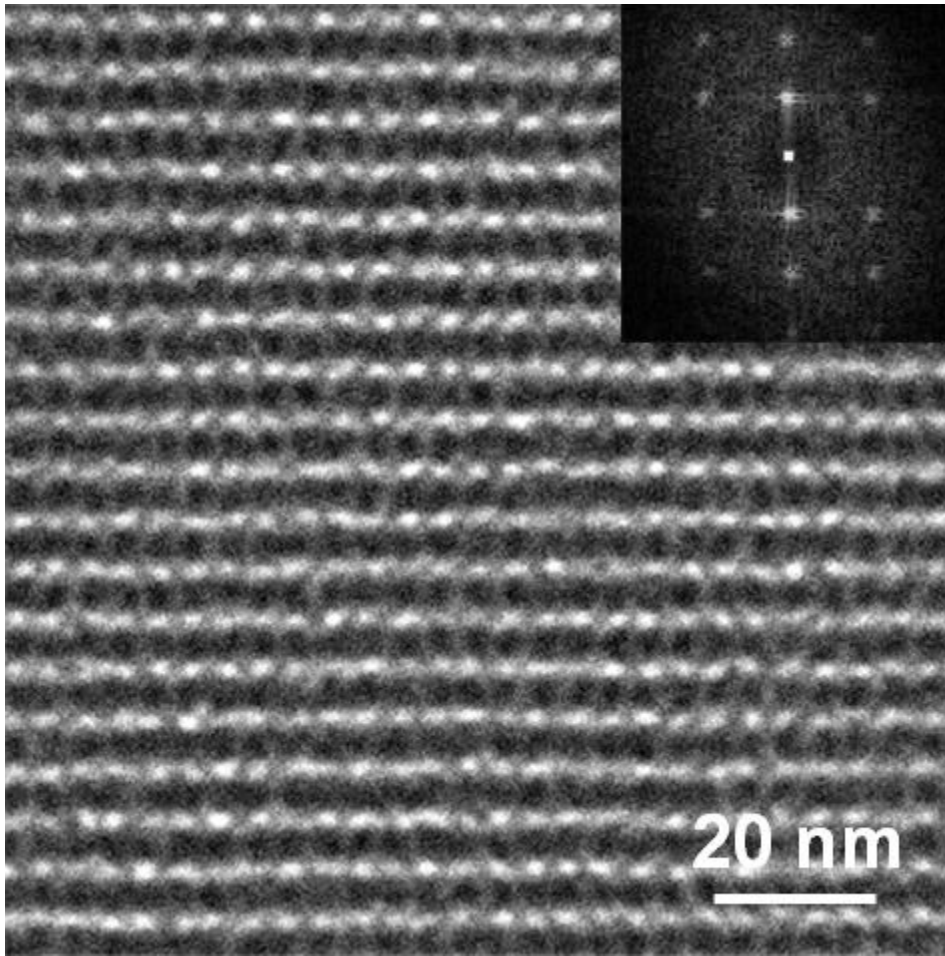


**Figure 4.8** TEM plan view image along [001] of the same ultra-thin nanoporous silica film as in Figure 4.7; the inset contains a fast fourier transform of the bright field image.

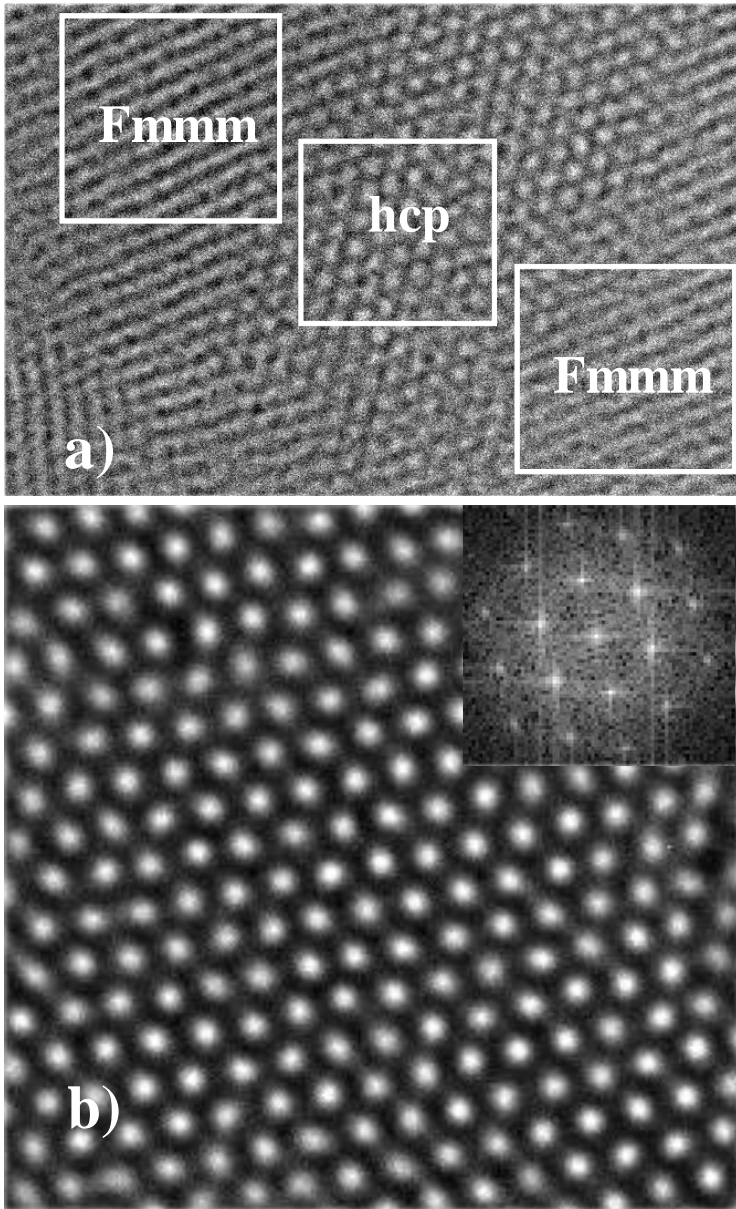


**Figure 4.9** TEM plan view showing a) coexistence of distorted bcc mesophases (*Fmmm*) and hcp mesophases and b) a (001) orientated hcp region (with FFT inset).

Using JEMS simulation program, we conducted TEM image simulation based on the values of  $Fm\bar{m}m$  unit cell parameters and the simulation result for  $Fm\bar{m}m$  structure along [110] orientation (Figure 4.10) is consistent with the TEM cross-sectional image (Figure 4.7), indicating the simulation results from GISAXS data is representative of the true structure of our ultra-thin film.



**Figure 4.10** TEM simulation result of  $Fm\bar{m}m$  structure along [110] orientation.

However, from the above TEM plan view and cross-sectional images of mesoporous silica thin film, it is difficult to visually view the pore trajectory, as predicted from  $Fm\bar{m}m$  and hcp packing (Figures 4.3 and 4.4). Also, pore size distribution, which is important for DNA translocation study is not available from the above characterization.

In the following section, Pt replica was introduced into the void mesopores of our thin film structure by electrochemical deposition to better estimate pore size and to examine the pore connectivity across the film.

## **4.2 Determination of pore size and pore tortuosity**

### **4.2.1 Surface-Acoustic-Wave (SAW) method**

N<sub>2</sub> adsorption-desorption isotherm, acquired directly on the thin film using a surface acoustic wave (SAW) technique<sup>119</sup>, shows a typical type IV isotherm with H1-type hysteresis; the average BJH pore diameter calculated from this data is 2.6nm (fwhm=0.2 nm) (Figure 4.11). Type H1 is often associated with porous materials to consist of agglomerates or compacts of approximately uniform spheres in comparatively regular array, and therefore to have narrow distributions of pore size<sup>120</sup>. Also, type H1 hysteresis had been reported to represent ink-bottle-type connected pores<sup>121</sup> or bicontinuous channel-like pores<sup>122</sup>. Overall, the appearance of the H1 hysteresis loop on the adsorption isotherm indicates a high degree of pore size uniformity and facile pore connectivity<sup>123</sup>. Based on adsorption isotherm, we obtain the porosity of thin film as 62% and surface area as 669 m<sup>2</sup>/g. We employed adsorption data rather than desorption data because it will avoid artifacts and improve the accuracy of the pore size distribution<sup>123</sup>. However, the reliability of current computational methods to calculate PSDs is yet to be improved since both BJH method<sup>124</sup> and DFT method<sup>123</sup> had encountered argument of the accuracy in determining pore size, e.g., it had been reported that BJH method underestimates pore sizes by more than 20%<sup>124</sup>. Therefore, Pt replication was employed

to fill the pores by electrochemical deposition method to visually determine the pore size and pore connectivity.

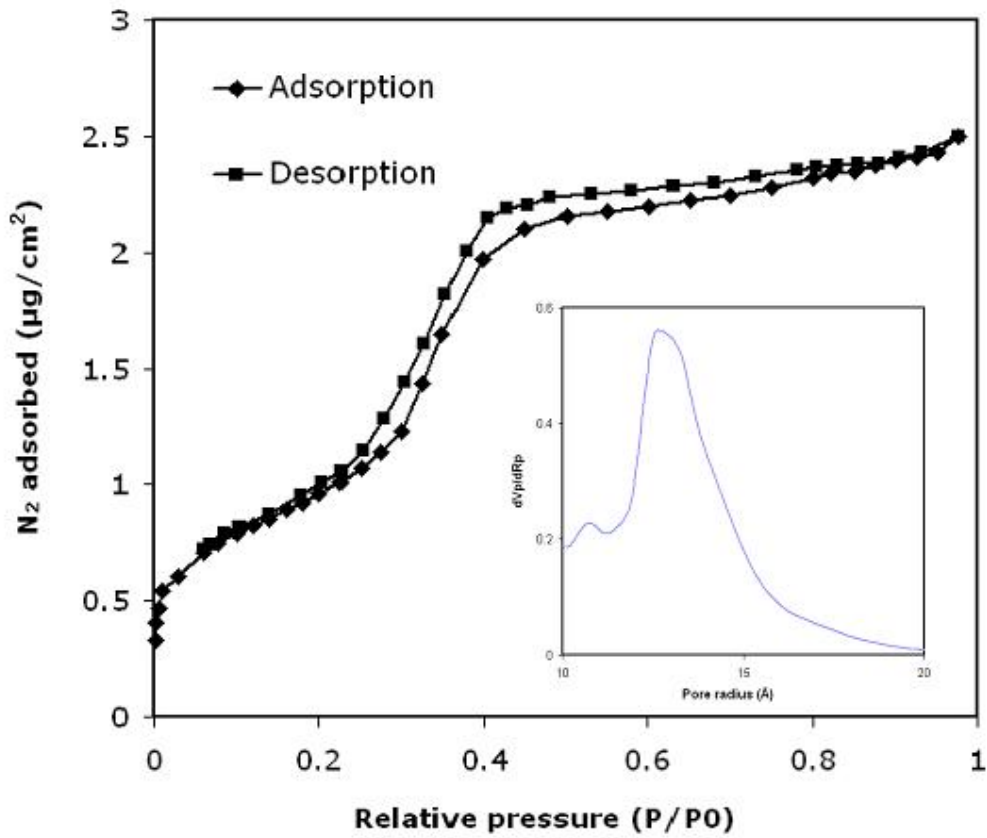


**Figure 4.11** Nitrogen sorption isotherm acquired for thin film mesophase using SAW technique and pore size distribution calculated by the BJH method based on the adsorption branch of the isotherm.

#### 4.2.2 Synthesis of Pt replica in mesoporous structure



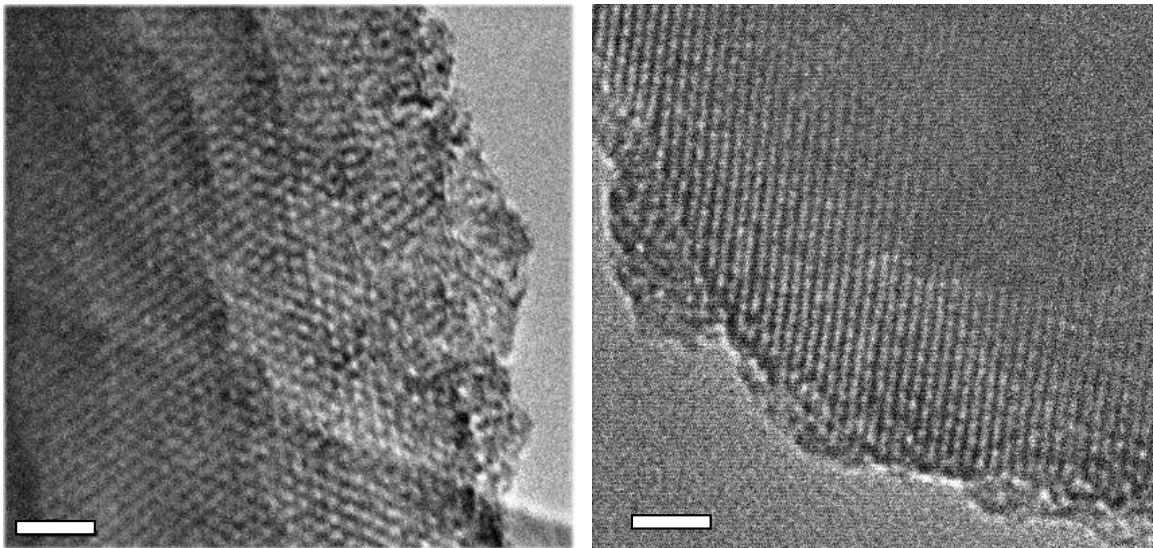
#### 4.2.2.1 Pt impregnation in solution

Calcined ultra-thin film with substrate was emerged in aqueous solution of tetraammineplatinum(II) nitrate ( $\text{Pt}(\text{NH}_3)_4(\text{NO}_3)_2$ , Aldrich) for multiple times (each time for 2hrs) to let Pt precursor impregnate into pores as much as possible. After being completely dried at 373 K, the thin film sample impregnated with  $\text{Pt}(\text{NH}_3)_4(\text{NO}_3)_2$  was put inside an oven where  $\text{H}_2$  gas with a constant flow rate passed through to create a reduction environment. The Pt compound was reduced to Pt(0) in the presence of  $\text{H}_2$  when the temperature in the oven was changed from room temperature to 383 K over 1 hr, maintained at 383 K for 1 hr, then increased from 383 to 573 K over 2 hrs, and finally maintained at 573 K for 2 hrs. The resultant Pt/SiO<sub>2</sub> composite sample was exposed to air after the oven was cooled to room temperature. The Pt/SiO<sub>2</sub> sample was washed with 2 wt % hydrofluoric acid until silica framework was completely removed.

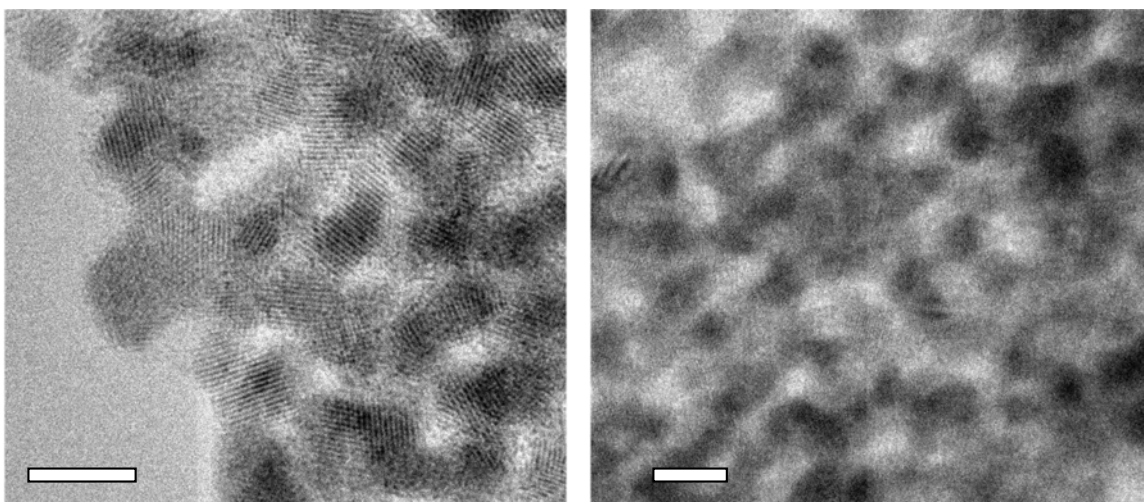
TEM images of Pt/SiO<sub>2</sub> sample before washed with hydrofluoric acid (Figure 4.12) show that silica thin film structure was well maintained after Pt impregnation. TEM images of the same sample after removal of silica with hydrofluoric acid (Figure 4.13) demonstrate the formation of Pt network. Although it is very clear of the formation of Pt network, very ordered Pt network comparable to Pt/SiO<sub>2</sub> structure before hydrofluoric acid treatment as in Figure 4.12 was not observed. Two possibilities might explain this: 1) The Pt precursor did not completely fill the whole pores of original silica framework so that the resulting Pt network did not completely represent the pore connectivity in the original framework; 2) The Pt network had been distorted by external forces during hydrofluoric acid treatment or during scratching before transferring the sample flake to

the TEM grid. To investigate the Pt network in more detail, we made cross-sectional Pt/silica sample. From TEM cross-sectional image of Pt/silica sample (Figure 4.14) it is clear Pt network has a lack of continuity along the whole film thickness. Meanwhile, the fact that the Pt precursor had been impregnated all the way to film/substrate interface indicates that our ultra-thin silica thin film has pore connectivity throughout the film thickness.

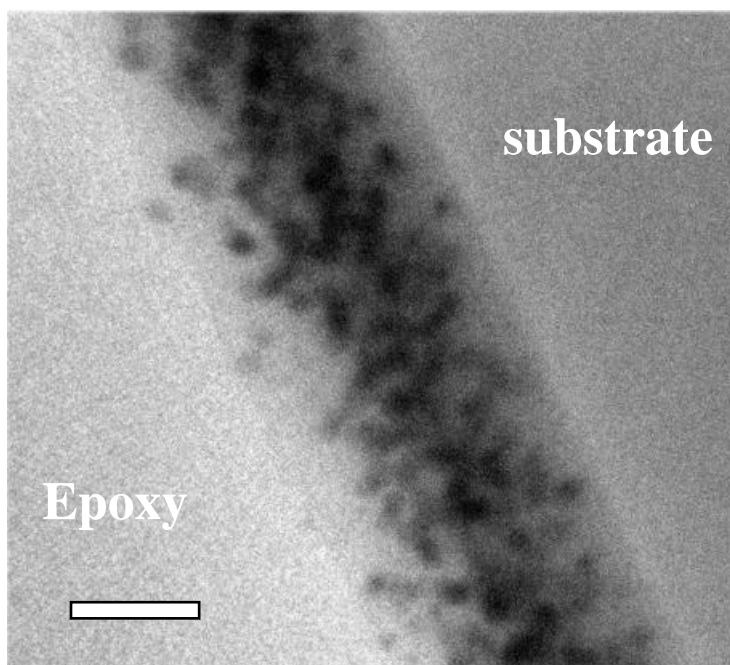
The schematic in Figure 4.15 shows that the Pt precursor is not completely deposited along the whole pore length. The lack of continuity may arise from: 1) the uneven nucleation or crystallization of the Pt particles along the pore length during Pt reduction at high temperature; 2) the more limited diffusion of the Pt precursor near the film/substrate interface compared to that near the film/bulk solution interface.



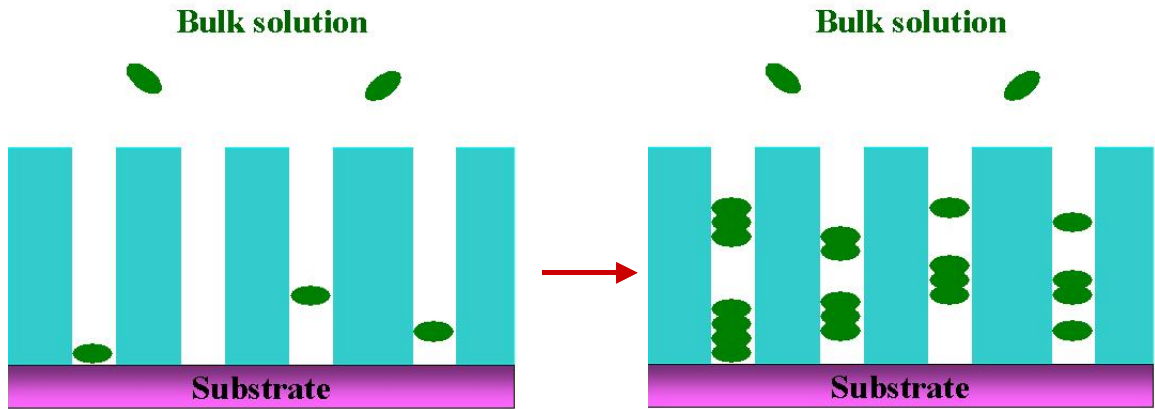
**Figure 4.12** TEM plan view of silica thin film structure after Pt impregnation in precursor and Pt reduction in H<sub>2</sub> afterwards (20 nm in scale bars).



**Figure 4.13** TEM plan view of Pt network after removal of silica framework in 2% HF solution (5nm in scale bars).



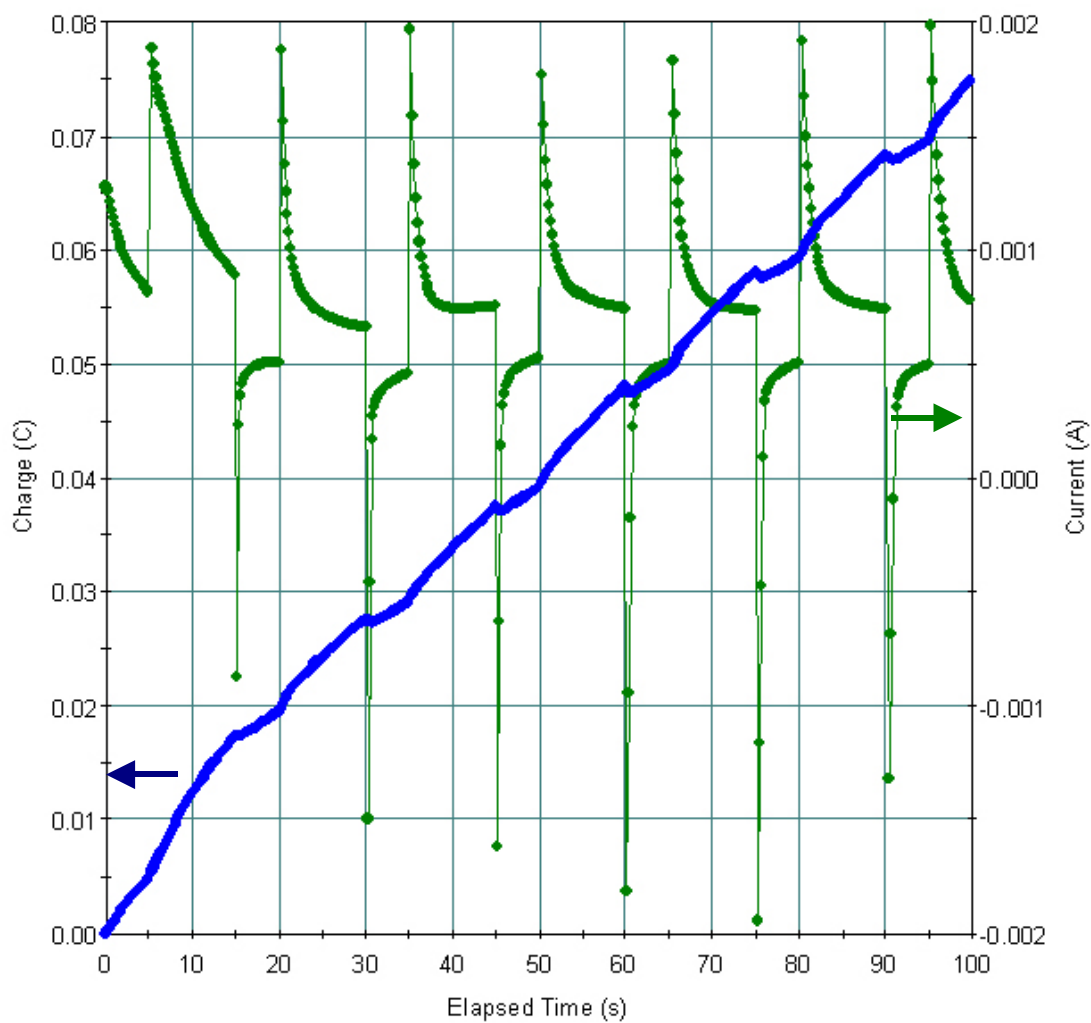
**Figure 4.14** TEM cross-sectional image of silica thin film structure after Pt impregnation in precursor and Pt reduction in  $H_2$  afterwards (20 nm in scale bars).



**Figure 4.15** Schematic of mechanism of Pt impregnation in our silica thin film structure (the Pt precursor shown in green).

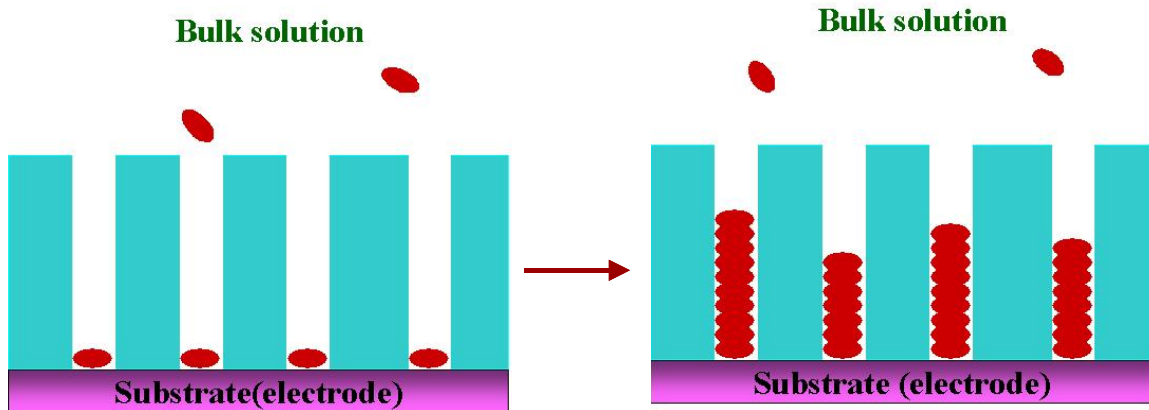
#### 4.2.2.2 Electrochemical deposition

Figure 4.16 shows the in-situ current and charge changes as a function of time during the pulsed potentiostatic Pt deposition. The charge was continuously increased with time, indicating Pt deposition was continuously built-up in the pores of silica thin film.



**Figure 4.16** In-situ charge (blue curve) and current (green curve) change as a function of time during Pt deposition under pulse voltammetry mode.

The mechanism of electrochemical deposition of Pt in our silica thin film structure can be described by the following schematic as in Figure 4.17.



**Figure 4.17** Schematic of mechanism of electrochemical deposition of Pt in our silica thin film structure (the Pt precursor shown in red).

In contrary to Pt impregnation in solution by sole diffusion, electrochemical deposition approach has the following advantages for Pt deposition in thin film structure:

1. The reduction of  $\text{H}_2\text{PtCl}_6$  precursor starts at film/substrate interface as the substrate is also the working electrode. In this way Pt has to build up from substrate until it fills the pore all the way up to the top of the film. Therefore it avoids the problem of the other approach that Pt deposition is not continuous along the pore pathway simply because Pt reduction as well as nucleation may occur at any part of pore pathway, impeding the diffusion of Pt precursor from bulk solution into the pore and causing the pore clogging;
2. Because the precursor used in electrochemical deposition is charged electrolyte, the diffusion of precursor from bulk solution to pores is enhanced during electrochemical deposition by the applied field;
3. After electrochemical deposition, Pt has been reduced to zero valence (as shown in following TEM images Pt element is actually in crystalline form after deposition),

therefore avoids the step of thermal treatment as in the other approach which might cause uneven Pt nucleation and growth in pores and possible damage to silica framework or Pt network by the heat.

After electrochemical deposition, the thin film surface was covered by continuous dark Pt network, which can be visually seen. TEM plan view of the scratched sample on holey carbon grid clearly shows that Pt replica was successfully impregnated into silica thin film structure on a large area and highly ordered silica thin film structure was maintained after Pt deposition (Figure 4.18). TEM cross-sectional image of the same film along (110) orientation of  $Fmmm$  structure shows Pt replica through the whole film thickness. The result is consistent with the cross-sectional images in Figure 4.7, which indicates that Pt was deposited from film/substrate interface and built-up throughout the film to become a network. The pattern of Pt network is comparable to the pore-to-pore pattern of original cross-sectional thin film sample, indicating that:

1. There is pore connectivity through the film thickness so electrochemical deposition can build up Pt from film/substrate interface to film surface;
2. Pt replica was built up exactly along the pore pathway so that it can be used to precisely represent the true pore connectivity and pore size in the original silica thin film.

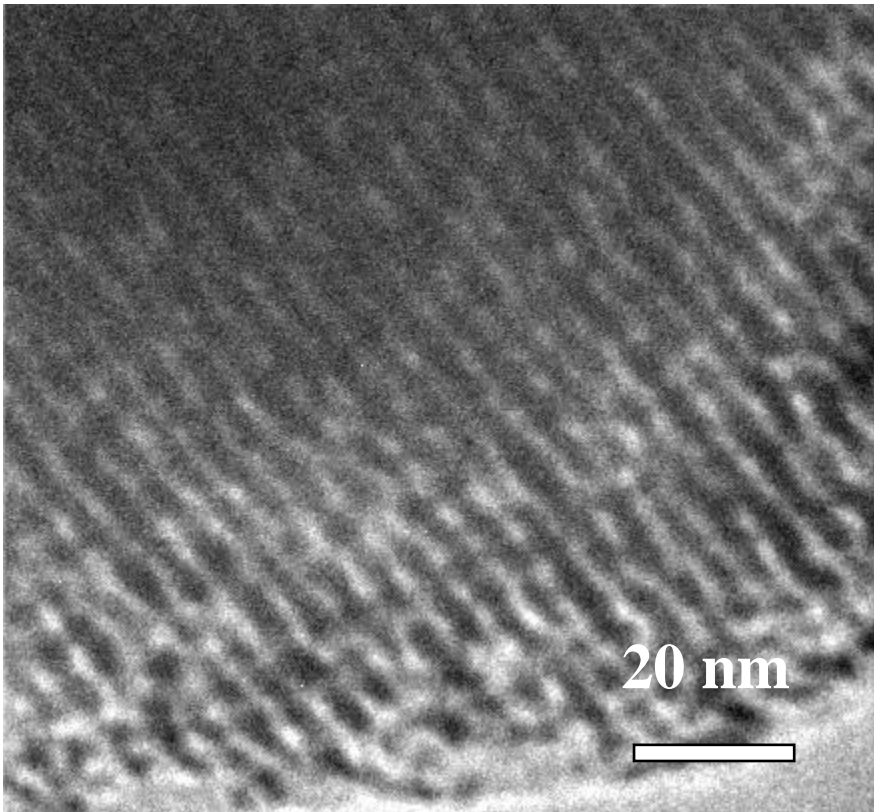


**Figure 4.18** TEM plan view along [001] of *Fmmm* silica thin film structure after electrochemical deposition of Pt, showing Pt was successfully impregnated into mesoporous silica thin film.



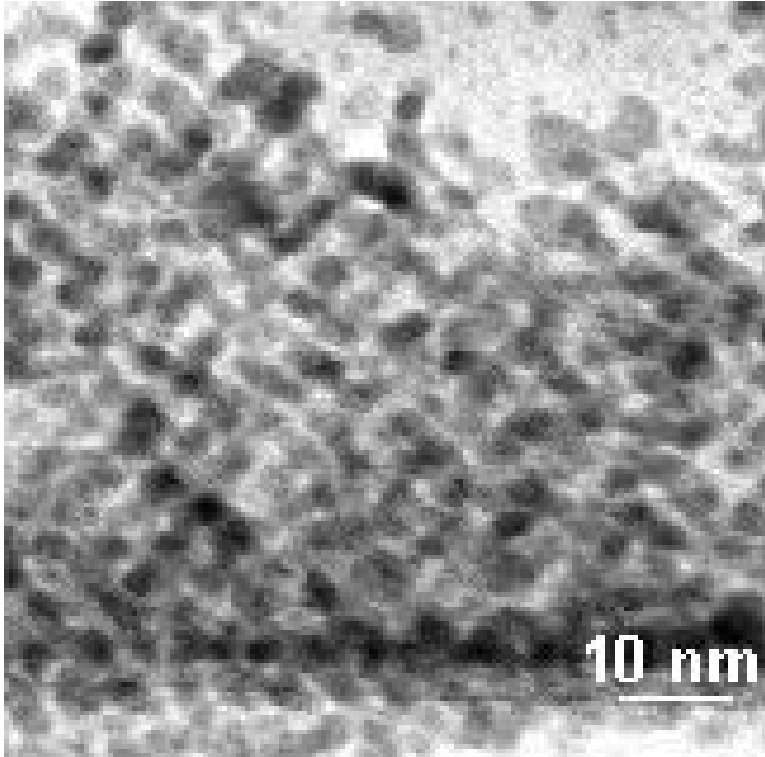


**Figure 4.19** TEM cross-sectional image along (110) of Pt network (without removing silica framework).

High resolution TEM of the Pt replica (Figure 4.20) shows crystalline lattice fringes of Pt with alternating wide and narrow regions corresponding to templated pores and the necking between them, respectively, giving estimated dimensions of ca. 4 nm for the pore diameter and ca. 2.6 nm for interpore necks. This suggests that, pore-to-pore connectivity provides the transport-limiting barrier to DNA translocation. Therefore, we assign 2.6 nm as the “effective pore diameter” to refer to the transport limiting pore

dimension. Additionally, the cross-sectional TEM image of the Pt replica in Figure 4.20 suggests preferential pore-to-pore connectivity in the through-thickness direction, while pore connectivity within the plane is limited.

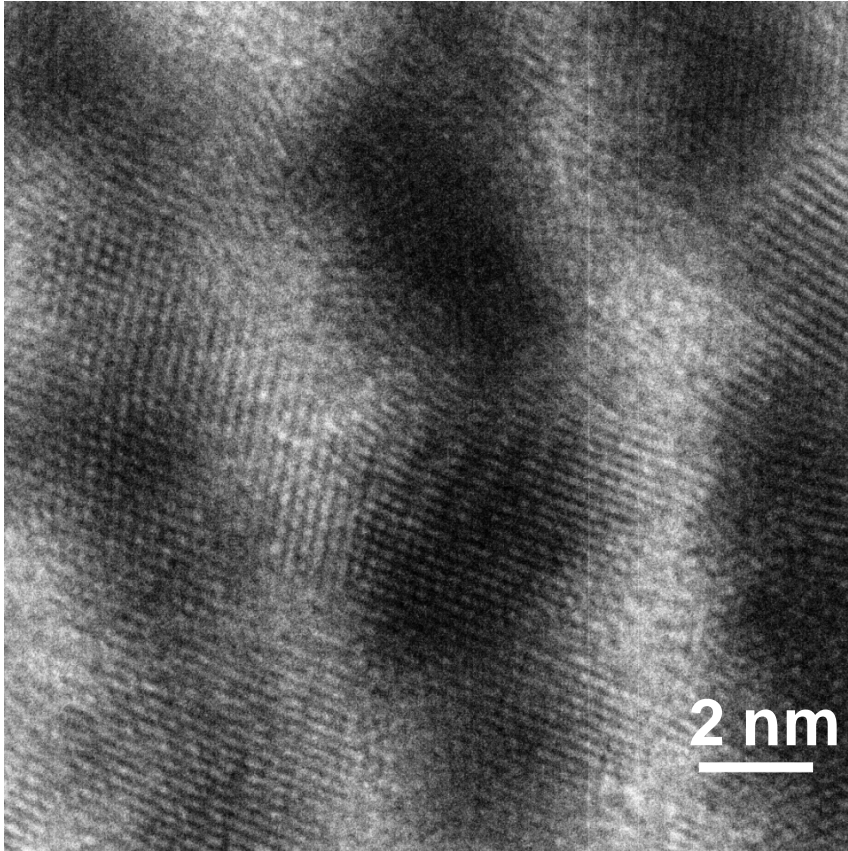


**Figure 4.20** High-resolution cross-section image of the Pt replica, showing the crystalline structure of the deposited Pt.

Figure 4.21 shows high-resolution image of the Pt replica deposited on hcp structure along [001] orientation, consistent with the coexistence of *Fmmm* and hcp mesophases in our silica thin film structure.

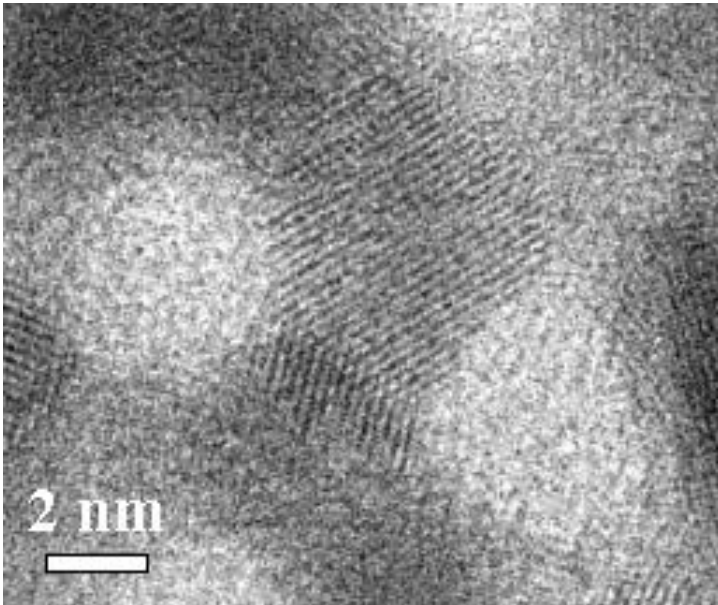


**Figure 4.21** TEM plan view of Pt replica along (0 0 1) of hcp mesophase.

As a result, from TEM characterization of Pt replica of our silica thin films, pore size and pore trajectory of original silica thin film are well investigated and therefore address a few important issues regarding DNA translocation through our mesoporous thin film:

1. Combining TEM cross-sectional images of our film with the pore pathway through the lattice predicted from *Fmmm* and hcp packing, we conclude that in original silica thin film there are no straight through pores in the direction perpendicular to the substrate. This tortuous pore-to-pore connectivity is different from any other reported nanopore systems (including biological nanopores and solid-state nanopores) used for DNA

translocation and therefore becomes an interesting system to investigate the influence of pore tortuosity on DNA translocation;

2. The effective pore diameter of our Brij 56 ultra-thin films is determined to be 2.6 nm based on Pt replica data and N<sub>2</sub> adsorption data, which is big enough to allow both ssDNA and dsDNA to transport through the film.

After synthesis and characterization of our thin film on Si substrate, we will integrate our thin film on porous substrates, especially substrates with single FIBed aperture before apply them in DNA translocation experiments.

### 4.3 Fabrication of novel nanopore array

#### 4.3.1 Fabrication of sub 100nm single pore on SiN substrate by FIB

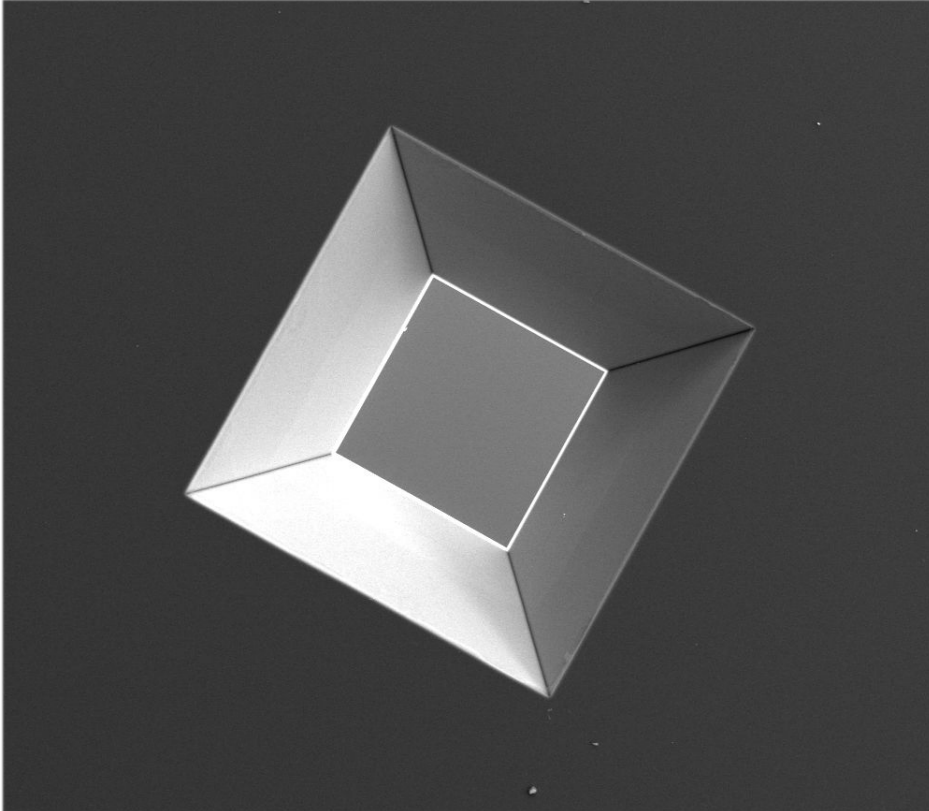


**Figure 4.22** SEM of SiN membrane on  $250\mu\text{m} \times 250\mu\text{m}$  window (smaller square in image) with supporting Si being etched away from a  $1\text{cm} \times 1\text{cm}$  Si wafer.

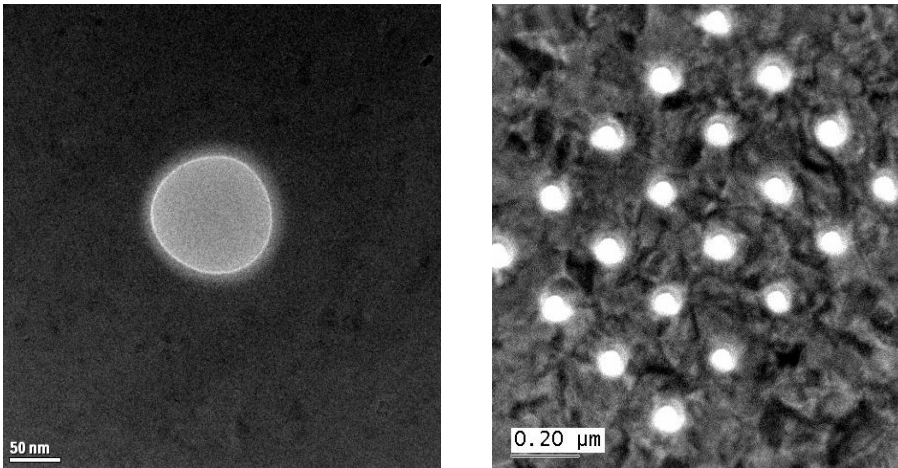


**Figure 4.23** TEM images of a single sub-100nm pore (left) and a sub-100nm pore array (right) drilled on 200 nm thick SiN membrane as shown in Figure 4.22.

### 4.3.2 Fabrication of self-assembled nanopore array

#### 4.3.2.1 Operation conditions to make thin film spanning porous substrates

##### 1. Coating methods:

##### Aerosol-assisted deposition:

This method has been proven very effective in making uniform thin films spanning porous substrates (especially coarse-pore ceramic substrates like Anodic Alumina Membrane, AAM)<sup>109</sup>. The schematic of the set-up had been shown in Figure 3.1 (adopted from G. Xomeritakis's paper).

##### Spin-coating:

Dip-coating method had been used to achieve confined assembly of mesoporous structures inside the porous substrates such as AAM<sup>107, 125</sup>. Because of the hydrophilic nature of AAM substrate, sol can be easily soaked into pores when the substrate is immersed into sol during dip-coating. So we applied spin-coating to intentionally avoid sol penetrating into the pores on the substrates. We also mount the porous substrates on a non-porous substrate like dense Si wafer so the non-porous substrate separates the porous substrate from direct contact with vacuum pump to avoid the aspiration of sol into the pores. We also use dynamic spin-coating (drop the sample on substrate during spinning) other than stationary spin-coating (drop the sample on substrate before spinning) to obtain better quality of the films that span the porous substrates.

## 2. Surface treatment:

This includes two parts: making the substrate surface hydrophilic; and making the surface inside the pores of the substrates hydrophobic. Hydrophilic substrate surface is required to obtain homogenous thin film structures completely covering the whole substrate including the pore area. Hydrophobic surface inside the pores can help preventing sol from penetrating into the pores. When we used our sol solution to measure the contact angle on a dense substrate surface, the contact angle on hydrophobic solid surface is ca. 20°, while the contact angle on hydrophilic solid surface is ca. 0°. The contact angle difference is not as huge as that when using DI water to make the contact angle (90° on hydrophobic surface instead of 20° for sol solution) because EtOH, the major component in sol composition, is amphiphilic. However, hydrophobic surface does

provide higher surface tension than hydrophilic surface, especially for substrates of hydrophilic nature (AAM etc).

To achieve the hydrophilic substrate surface and in the meantime the hydrophobic surface inside pores, we first immersed the porous substrates inside 6% Hexamethydisilazane (HMDS) in Hexane solution @ 50°C for 48hrs. Then the substrate was treated in O<sub>2</sub> plasma for 2 mins under vacuum. Because the mean free path of plasma particles under vacuum is » 0.1 µm, which is the scale of the pores in our substrates, we expected the plasma specifically generated the hydrophilic functional groups (-OH) on substrate surface and pore entrance area, while the surface inside the pores were still hydrophobic.

4.3.2.2 Anodic Alumina Membrane (AAM) as porous substrate:



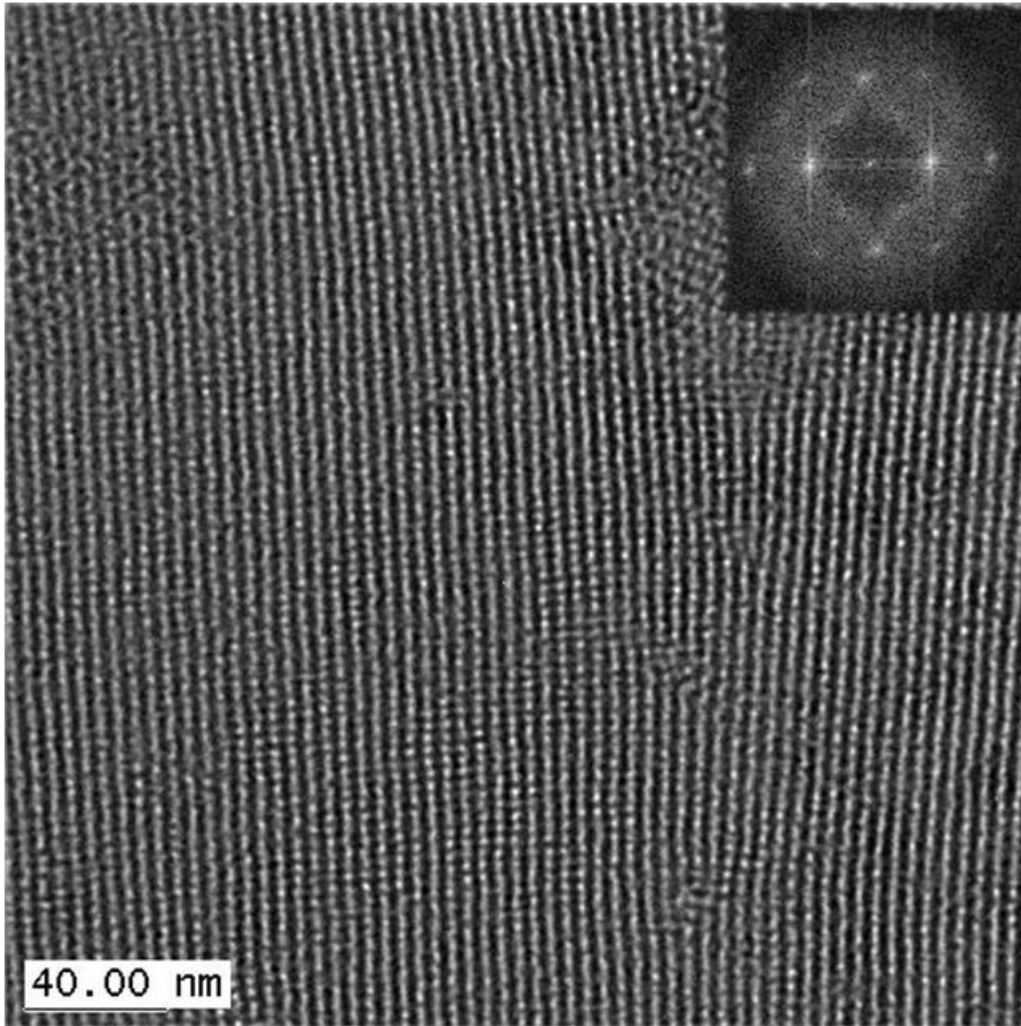


**Figure 4.24** TEM plan view image for a Fmmm thin film along [001]; the sample was scratched off AAM substrate with 100nm pore diameter; the inset contains a fast fourier transform of the bright field image.

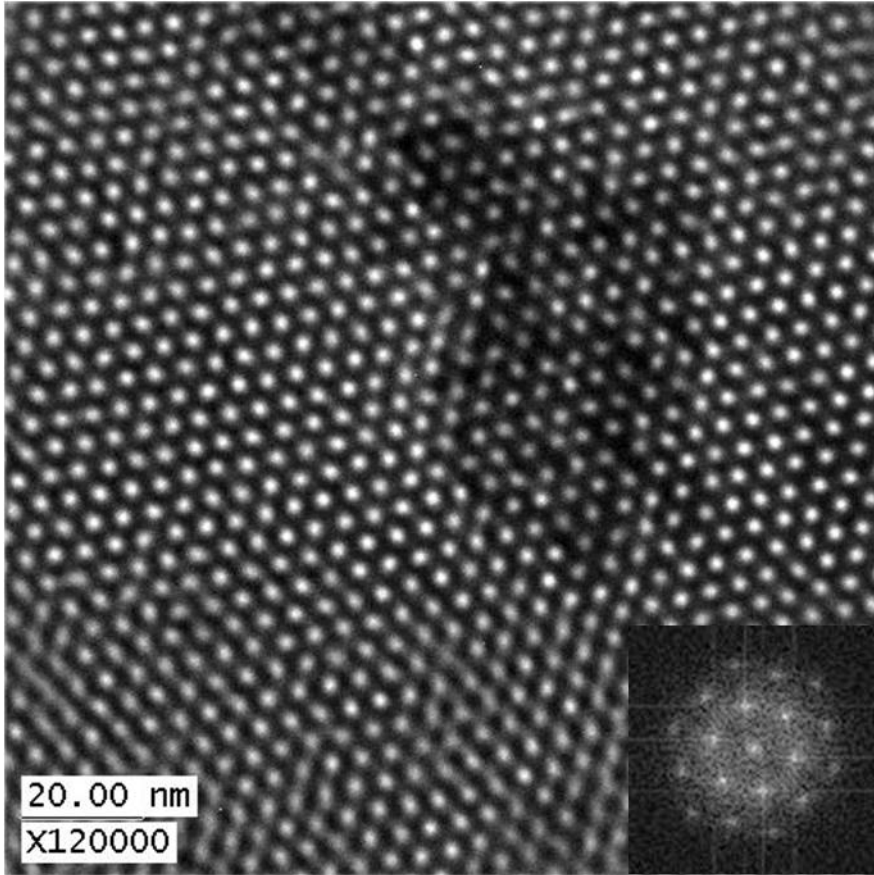


**Figure 4.25** TEM plan view image of a thin film along [001] of  $P6_3/mmc$  mesophase; the sample was scratched off AAM substrate with 100 nm pore diameter; the inset contains a fast fourier transform of the bright field image.

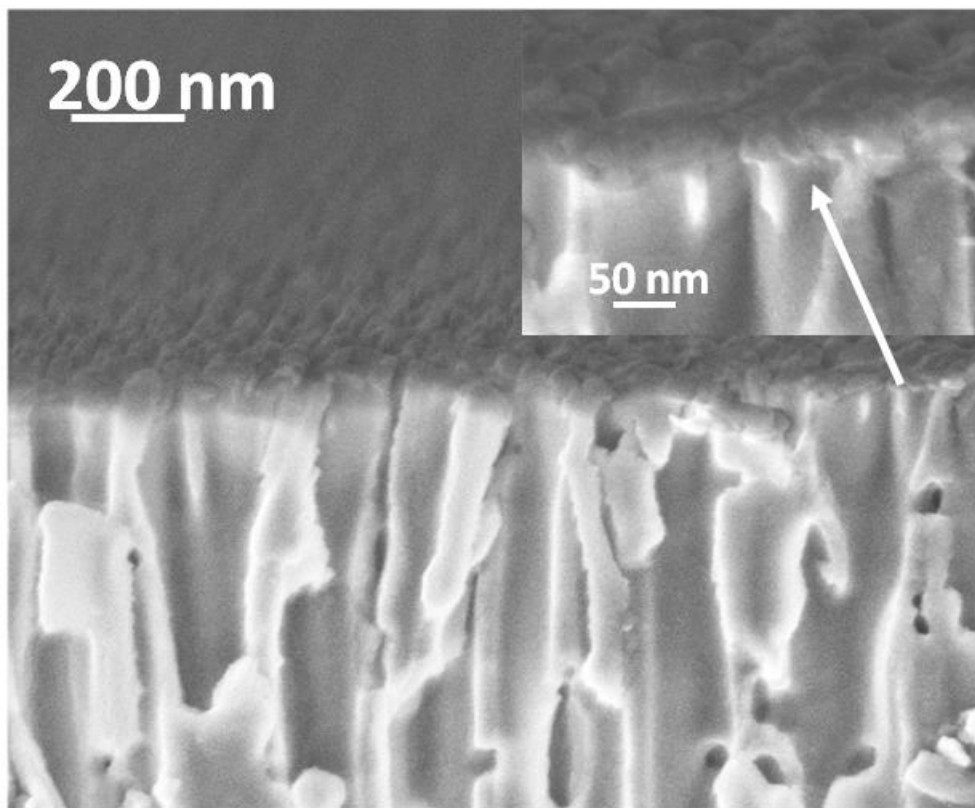


**Figure 4.26** SEM cross-sectional image of ultra-thin mesoporous silica film spanning 200 nm pores of anodic aluminum membrane. Inset is SEM with high magnification, showing thin film structure uniformly spans the porous substrate without penetrating into the pores.

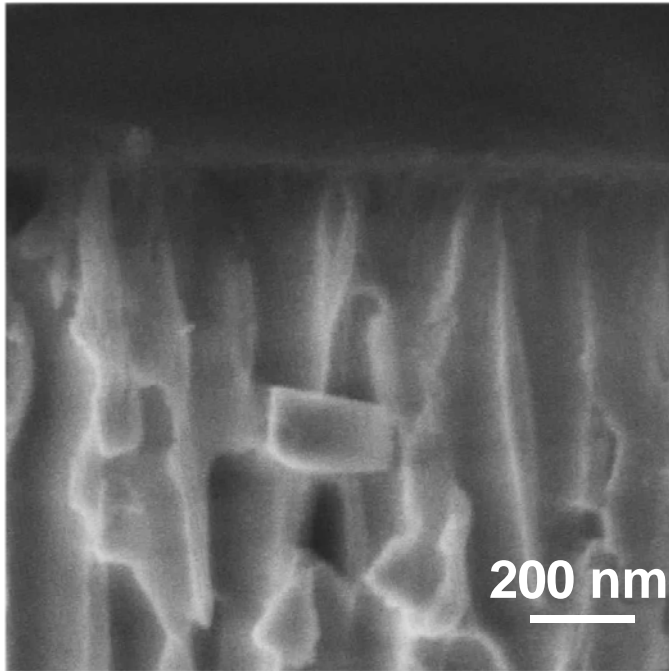


**Figure 4.27** Other SEM cross-sectional images showing mesoporous thin film spans 200nm anodic aluminum membrane pores.

4.3.2.3 Integration of ultra-thin mesoporous silica film on sub 100nm single pore on SiN substrate by FIB

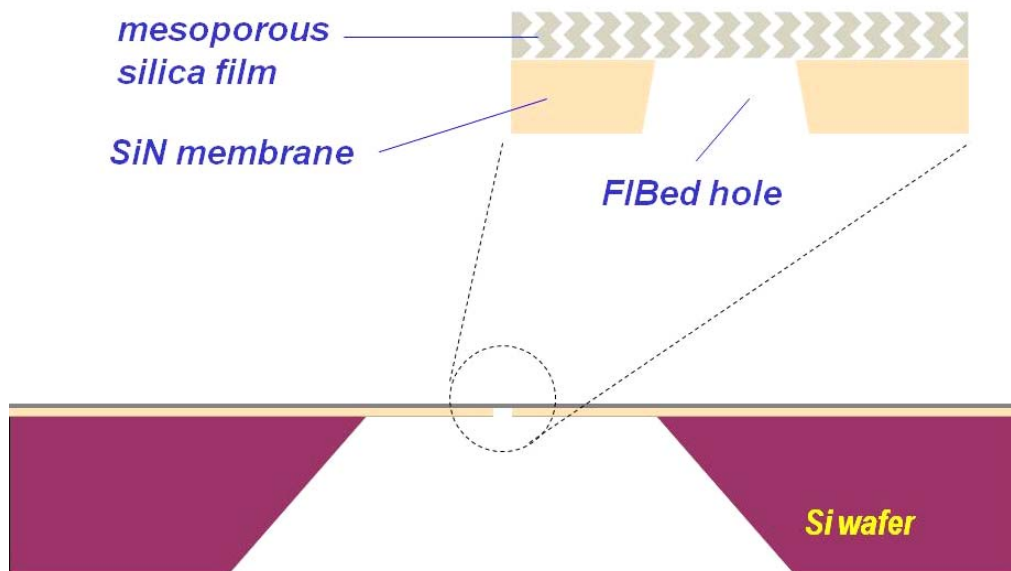


**Figure 4.28** Schematic of mesoporous thin film spanning SiN membrane with a single hole made by FIB

In chapter 4.1, we have applied GISAXS along with further TEM analysis to identify the mesophases in our ca. 30nm mesoporous silica thin films deposited on solid Si substrate as a mixture of the related body-centered cubic ( $Fm\bar{3}m$  space group) and 3D hexagonal phases ( $P6_3/mmc$  space group), with each mesophase sharing identical (002) spacing. Although it is difficult to characterize our thin film structures on porous substrates with GISAXS (most likely the coarse-pore substrate dramatically affects the incidence angle of x-ray striking on the film so no clear scattering pattern can be obtained), we expect the mesophases in our ultra-thin mesoporous silica films deposited on porous substrates are a mixture of the related  $Fm\bar{3}m$  and  $P6_3/mmc$  mesophases, as had been demonstrated by TEM images of the thin films deposited on AAM porous substrate (Figure 4.24 and Figure 4.25). TEM plan view images of our mesoporous silica thin films

spanning the single FIBed aperture also show [001]-oriented  $Fmmm$  phase (Figure 4.29) as well as [001]-oriented  $P6_3/mmc$  phase (Figure 4.30), consistent with the results obtained from the thin films deposited on solid Si substrates and AAM substrates. Fast fourier transform patterns in the insets of Figure 4.29 and 4.30 further verify the observed mesophases are  $Fmmm$  and  $P6_3/mmc$  mesophases respectively. More interestingly, Figure 4.31 shows the coexistence of  $Fmmm$  and  $P6_3/mmc$  mesophases above the same FIB aperture. These TEM plan view images clearly demonstrate that, the thin films spanning sub 100nm aperture have the same structure as those on the solid substrates. Therefore the established structure model and pore tortuosity calculation in chapter 4.1 are also applicable to the thin film structure on the porous substrates.

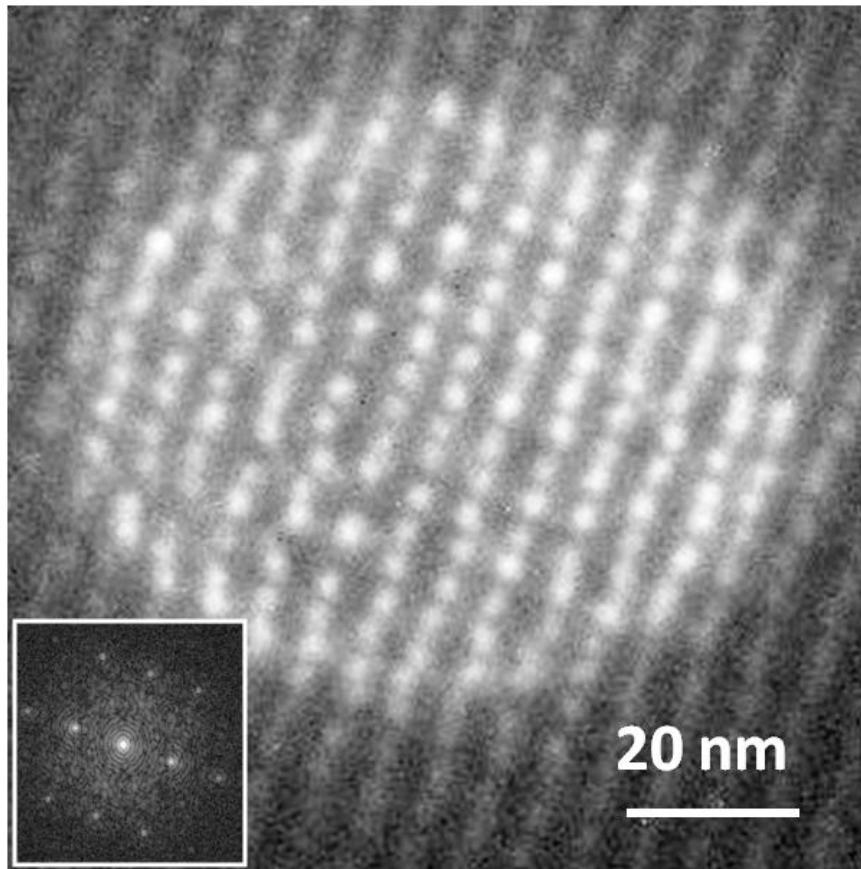


**Figure 4.29** TEM plan-view image of free-standing *Fmmm* film suspended over a sub-100-nm diameter aperture formed by FIB. The orientation is along  $[0\ 0\ 1]$ . The inset contains a fast fourier transform of the bright field image.

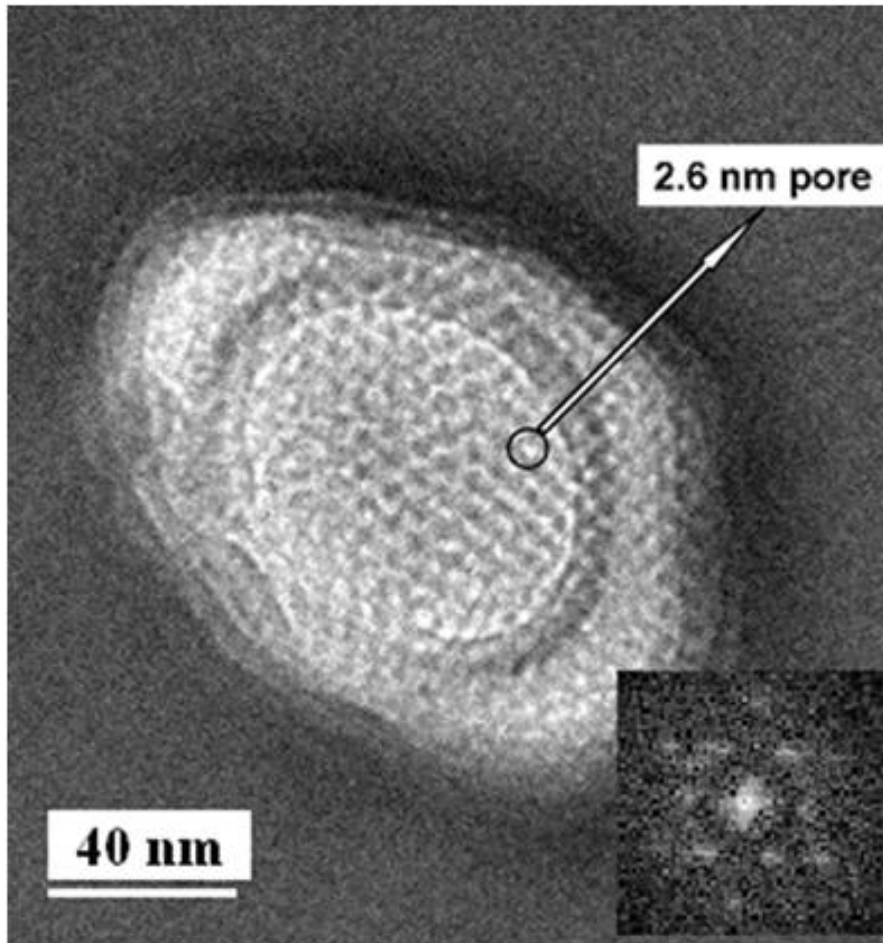


**Figure 4.30** TEM plan-view image of free-standing  $P6_3/mmc$  film suspended over a sub-100-nm diameter aperture formed by FIB. The orientation is along  $[0\ 0\ 1]$ . The inset contains a fast fourier transform of the bright field image.



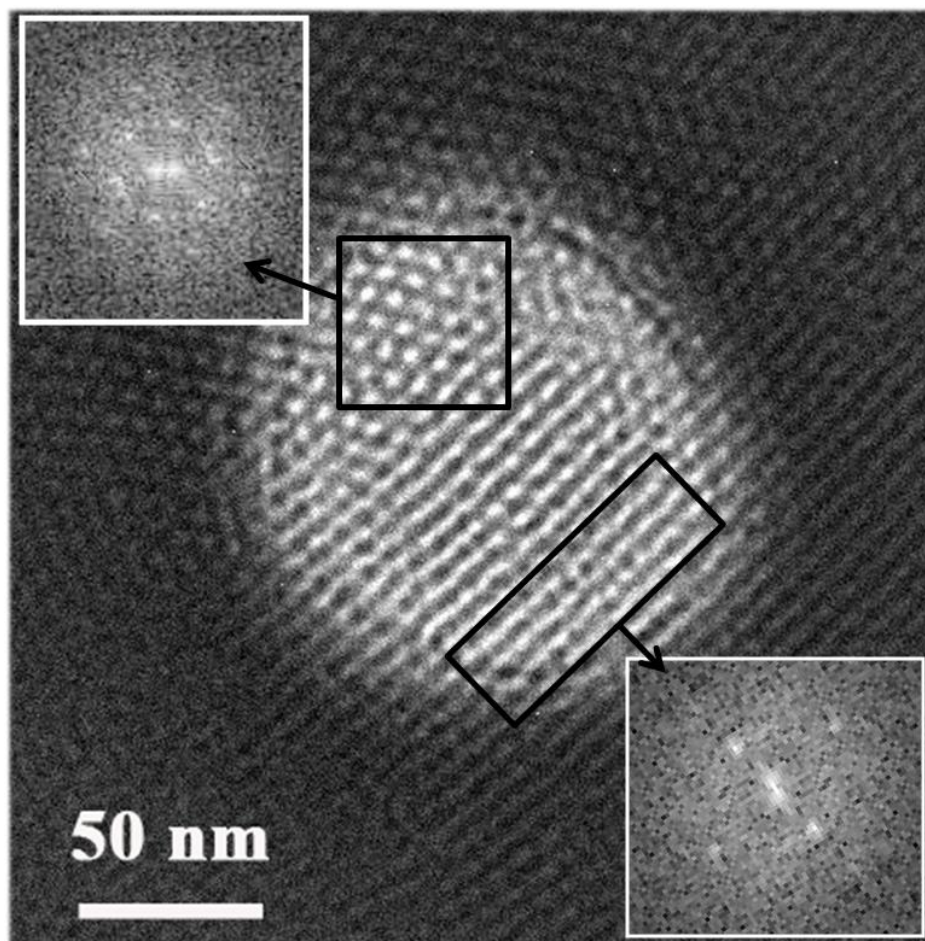


**Figure 4.31** TEM plan-view image of free-standing film suspended over a sub-100-nm diameter aperture formed by FIB. The thin film exhibits coexistence of  $Fmmm$  along  $[001]$  and  $P6_3/mmc$  along  $[001]$  on the single FIBed aperture. The insets contain fast fourier transforms of the bright field images of the two mesophases.

#### 4.3.2.4. Selective nanopores blocking by focused-electron-beam

This application is useful when we need to achieve the presence of single or small amount of pores on the nanopore array fabricated above. Because there is residual carbon resource in the chamber of TEM, we can locate focused electron beam on the area of sample where we want the nanopores to be erased (see Figure 4.32), then a thin layer of carbon is deposited at the area of electron beam while the surrounding area is not affected. As shown in Figure 4.32d, we demonstrate the presence of single nanopore after all other nanopores on the FIBed aperture had been smeared out.

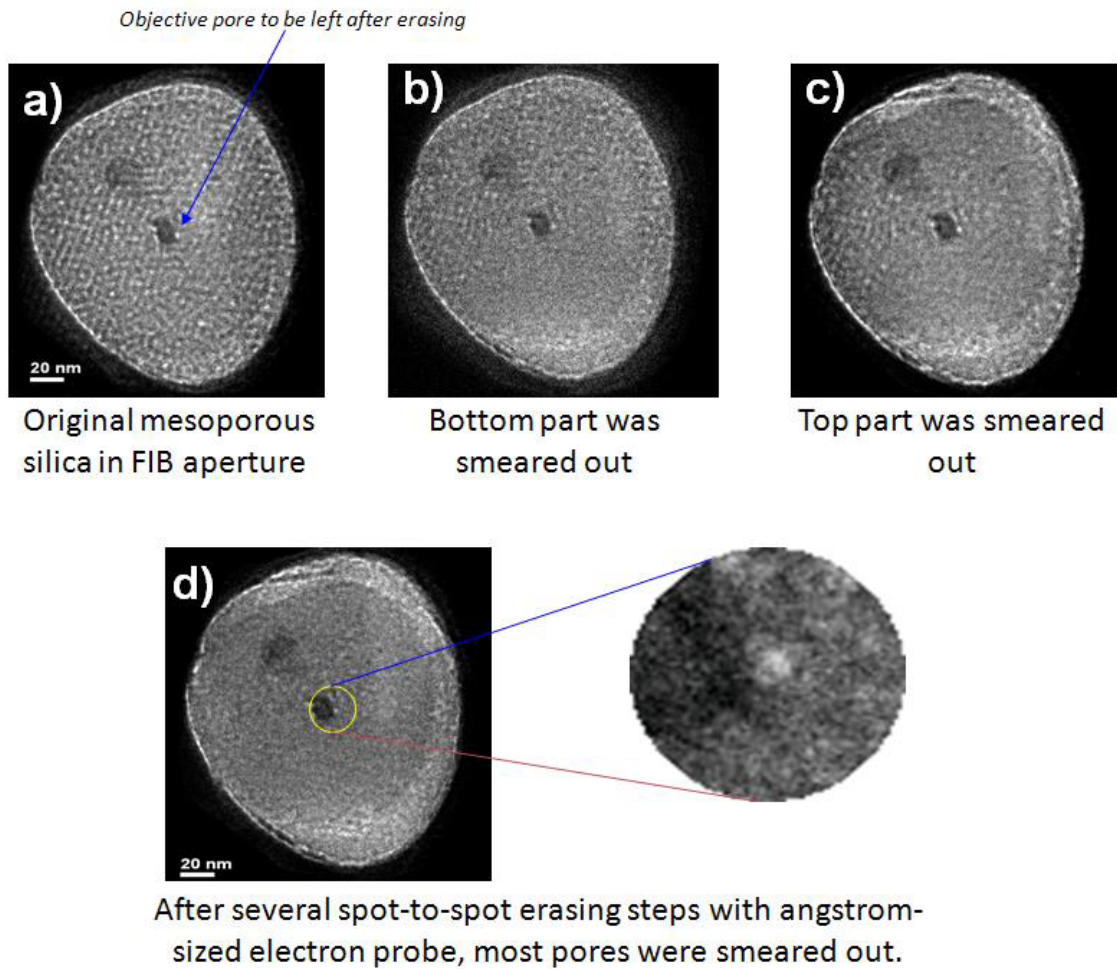


**Figure 4.32** TEM plan view images of mesoporous thin film on FIBed aperture with the progression of focused electron beam treatment to smear out most of nanopores above FIBed aperture (from a to d). The inset shows only one nanopore is left after the treatment. The black spot near the nanopore in d) is used to locate the nanopore place.

In conclusion, we had made  $\sim 30$  nm thick mesoporous silica thin film structure and had successfully integrated this thin film structure on substrate with a single sub-100 nm aperture. The resulting nanopore array presents effective pore diameter of 2.6 nm and tortuous pore shape with  $\sim 1.5$  tortuosity along film thickness and is ready for DNA translocation experiments.

## **4.4 Surfactant removal**

Because our mesoporous thin film is applied for DNA translocation, surfactant and any organic groups inside the pores must be removed before DNA translocation experiments. Therefore it is worth to discuss different methods for surfactant removal and their influence on mesoporous thin film structures.

### **4.4.1 Thermal treatment**

Thermal treatment is the most popular method to remove surfactant while retaining the inorganic framework. TGA and DTA were used to establish the appropriate temperature window enabling complete surfactant removal without silane decomposition. Figure 4.33 shows that, for thin film sample with Brij 56 as surfactant, the maximum derivative weight loss of thin film sample occurs at 400°C, indicating decomposition of Brij 56 surfactant is most efficient at this temperature. Therefore, for thermal treatment, we let the sample stay at 400°C for 1 hr to remove the surfactant.

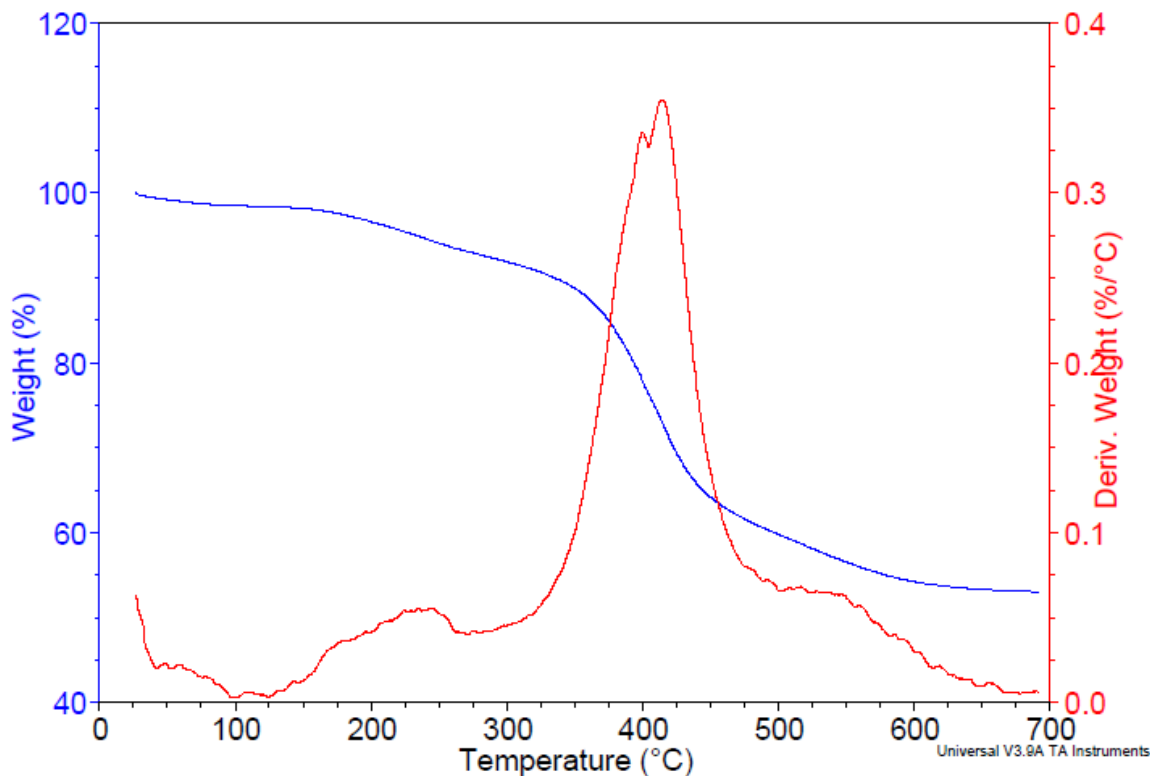


**Figure 4.33** TGA and DTA data indicate appropriate temperature window for surfactant removal.

At temperature above 400°C, the surfactant can also be removed completely. However, the porous silica film may be under the risk of decomposition at very high temperature and film structure may also encounter dramatic change due to the uniaxial shrinkage perpendicular to the substrate. When calcination temperature increases, the primary diffraction peak of the film on XRD spectroscopy right-shifts to higher 2-theta value, indicating higher degree of film shrinkage.

#### **4.4.2 Other treatment for surfactant removal**

	Thermal treatment		UV ozone treatment		Extraction		Piranha treatment	
	Before	After	Before	After	Before	After	Before	After
Thickness (nm)	53	39	53	39	53	46	39	35.5
Reflex Index	1.37	1.17	1.37	1.22	1.37	1.26	1.36	1.27

**Table 4.1** Comparison of film thickness and refractive index before and after a variety of treatments for surfactant removal.

Besides thermal treatment, there are other options to remove surfactant, as shown in Table 4.1. UV ozone treatment is conducted in a reaction box with film facing up and 0.5” away from UV light. Treatment time is 70 mins. Extraction is conducted in 1N HCl/EtOH solution with constant temperature of 78°C for 12 hrs. Fresh piranha solution is prepared before each treatment and the piranha treatment is conducted on a mildly heated hot plate for 20 mins. Thickness and refractive index were obtained from ellipsometry instrumentation. Because amorphous SiO<sub>2</sub> solid gives refractive index of 1.5 and the air gives refractive index of 1.0, the value of refractive index of thin film can be used to calculate the porosity of porous structure based on the lorentz-lorentz equation, hence to evaluate whether surfactant had been removed from the pores. The lower the

refractive index, the more complete the surfactant removal. The results of Table 4.1 show that thermal treatment is the most efficient method to remove surfactant. However, thermal treatment also causes biggest uniaxial shrinkage of film thickness, followed by UV ozone, extraction and piranha treatment with gradually decreased influence on film thickness. XRD data also shows that the shift of primary diffraction peak regarding 2-theta after thermal treatment is largest, while piranha treatment causes the smallest shift of primary peak.

## Chapter 5

### **Results and Discussions II: Atomic-Layer-Deposition (ALD) for the modification of pore size and pore surface chemistry**

As described in Chapter 1.6, because mesoporous silica thin film by EISA provides plenty of –OH group on pore surface, it allows a lot of precursors to react on pore surface for pore size and pore surface chemistry modification. Because of the small pore size (2.6 nm) in our mesoporous system, a more efficient surface modification method is required. As a self-limiting, highly conformal, layer-by-layer deposition process with resolution of angstrom level, thermal ALD had been demonstrated to achieve more effective and conformal deposition in a porous system with very small pore size, as compared to other possible approaches like CVD, post-synthesis grafting<sup>103</sup> etc.

Plasma-assisted ALD is another powerful method for fine tuning mesopores<sup>126</sup>. Different from thermal ALD with conformal deposition inside pores, plasma ALD preferentially induced deposition near the pore entrance. However, in this dissertation, we are more interested in getting conformal deposition inside mesopores. Therefore, the following ALD processes are all referring to thermal ALD.

#### **5.1 TiO<sub>2</sub> ALD**

##### **5.1.1 TiO<sub>2</sub> ALD to fine tune the pore size**

Standard thermal- ALD using TiCl<sub>4</sub> and H<sub>2</sub>O as precursor had demonstrated a conformal coating on the surface of nanopores by penetrating into the internal porosity of



the whole mesoporous structure, which ensures the identical pore size reduction of all pores on the films<sup>126</sup>. During single layer deposition, we applied multi-exposure of  $\text{TiCl}_4$  without introducing  $\text{H}_2\text{O}$  to ensure that the  $\text{TiO}_2$  monolayer covers the whole surface area.

Table 5.1 lists refractive index data measured by spectroscopic ellipsometry for thin nanoporous silica films before and after one and two layers of thermal  $\text{TiO}_2$  ALD, and the corresponding volume percentage and thickness of  $\text{TiO}_2$  calculated from this data using a Bruggeman Effective Medium Approximation (EMA)<sup>127</sup> (calculated using  $n_{\text{SiO}_2} = 1.46$ , and  $n_{\text{TiO}_2} = 2.00$ ), in combination with Brunauer-Emmett-Teller (BET) film surface areas obtained from  $\text{N}_2$  adsorption data ( $290 \text{ m}^2/\text{g}$  for the film before ALD, and  $286 \text{ m}^2/\text{g}$  after one layer of ALD). Although the estimated volume fraction of  $\text{TiO}_2$  is dependent on the value of the refractive index for  $\text{TiO}_2$  used in the EMA calculations, variation of  $n_{\text{TiO}_2}$  over the range of 1.90 to 2.10 (typical for non-crystalline titania) modifies the volume fraction by only ca. 10%. The calculated thickness of  $1.7 \text{ \AA}$  for the first ALD layer, and  $1.5 \text{ \AA}$  for the second layer are consistent with the expected thickness per deposition step of ca.  $1.6 \text{ \AA}$ <sup>128</sup>, indicating one and two layers of  $\text{TiO}_2$  ALD deposition inside the silica nanoporous film results in pore diameter reduction of approximately  $3.4 \text{ \AA}$  and  $6.4 \text{ \AA}$  respectively. Therefore, for our original thin film with a  $2.6 \text{ nm}$  “effective pore diameter” determined by the BJH calculation in combination with high resolution TEM of the Pt replica, the approximate pore diameter after one and two layers of  $\text{TiO}_2$  ALD are  $2.3 \text{ nm}$  and  $2.0 \text{ nm}$  respectively.

	Refractive Index	Pore volume fraction	Volume fraction of TiO <sub>2</sub>	TiO <sub>2</sub> thickness (Å)	$\sigma$ (Å)
Before ALD	1.260	0.42	--		
1 Layer TiO <sub>2</sub> ALD	1.305	0.37	0.05	1.7	3.4
2 Layer TiO <sub>2</sub> ALD	1.350	0.33	0.09	3.2	6.4

**Table 5.1** Refractive index, pore volume fraction, and TiO<sub>2</sub> volume fraction calculated using a Bruggeman EMA, and the corresponding thickness of TiO<sub>2</sub> and pore size reduction ( $\sigma$ ) for one and two layers of TiO<sub>2</sub> ALD deposition inside a silica nanopore film.

As discussed above, we derive pore diameter reduction after TiO<sub>2</sub> ALD from refractive index data with Bruggeman EMA by taking both SiO<sub>2</sub> bulk framework and monolayer or double-layer of TiO<sub>2</sub> thin film into consideration. Because TiO<sub>2</sub> layer is very thin compared to SiO<sub>2</sub> bulk framework, here we can apply the Lorenz-Lorenz equation to calculate the porosity after TiO<sub>2</sub> ALD by only taking  $n_{\text{SiO}_2}$  into account (that is to say, the measured difference of bulk refractive index after TiO<sub>2</sub> ALD is attributed to the volumetric reduction after TiO<sub>2</sub> ALD rather than the contribution of the higher  $n_{\text{TiO}_2}$  compared to  $n_{\text{SiO}_2}$ , which is a reasonable assumption especially when the deposited TiO<sub>2</sub> layer is amorphous, as evidenced by the fact that the XRD diffraction patterns of ALD treated sample don't fit the diffraction patterns of any crystalline forms of TiO<sub>2</sub>). Then by

comparing the porosity before/after ALD assuming pores are cylinder-shaped with conformal deposition, we can estimate the pore diameter reduction after each ALD layer (see Table 5.2). Table 5.2 shows that, the calculated pore diameter reduction after one and two layers of TiO<sub>2</sub> ALD are ca 3.2 Å and 6.8 Å respectively, consistent with the approximation results obtained from Bruggeman EMA and 1.55 Å /cycle of TiO<sub>2</sub> growth rate reported elsewhere at similar ALD operating conditions<sup>128</sup>.

	Refractive Index	Porosity (%)	$\sigma$ (Å)	$\sigma/2$ (Å)
Before ALD	1.260	40.2	--	
1 Layer TiO <sub>2</sub> ALD	1.305	30.7	3.2	1.6
2 Layer TiO <sub>2</sub> ALD	1.350	21.4	6.8	3.4

Table 5.2 Refractive index, porosity calculated from Lorenz-lorenz equation, and corresponding thickness of TiO<sub>2</sub> ( $\sigma/2$ ) and pore size reduction ( $\sigma$ ) for one and two layers of TiO<sub>2</sub> ALD deposition inside a silica nanopore film.

Also, the BJH pore diameters calculated from the N<sub>2</sub> adsorption isotherm before and after one layer of TiO<sub>2</sub> ALD show a ca. 3 Å decrease of pore diameter (see Figure 5.1), which is close to that calculated from the refractive index data (Tables 5.1 and 5.2); although the BJH method can be subject to large errors in the determination of absolute pore size, errors in relative measurements are expected to be significantly lower.

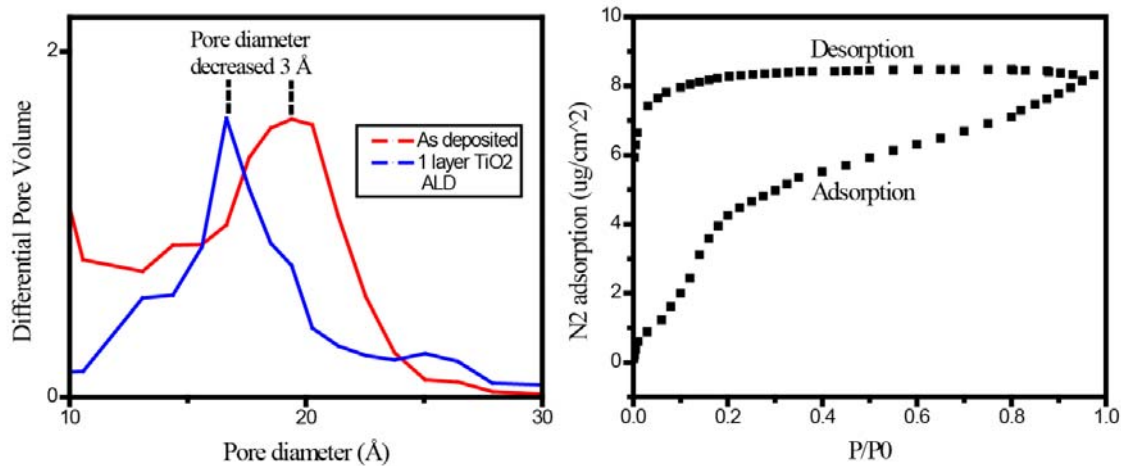


**Figure 5.1** Pore size distribution of as deposited Brij 56 film and the same film after 1 layer of TiO<sub>2</sub> ALD calculated from adsorption branch of the N<sub>2</sub> adsorption data using a BJH model, showing ~ 3 Å pore size reduction after ALD (left); and the SAW acquired N<sub>2</sub> adsorption isotherm of Brij 56 film after 1 layer of TiO<sub>2</sub> ALD, showing extensive hysteresis on desorption branch, which is consistent with a constricted micropore network<sup>129</sup> (right).

In Figure 5.2 (adopted from Jiang YB. et al.<sup>126</sup>), we show that thermal ALD of TiO<sub>2</sub> gives conformal deposition of TiO<sub>2</sub> layers inside mesopores and the deposited TiO<sub>2</sub> is in amorphous form.

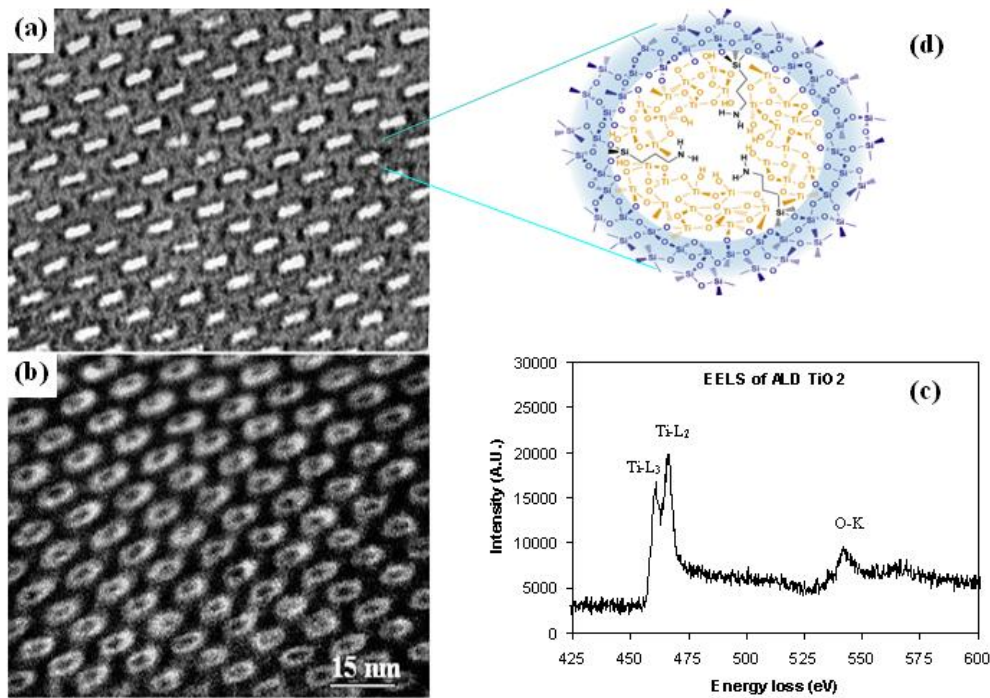


**Figure 5.2** a) Cross-sectional TEM image: uniform deposition & conformal coating; b) corresponding Ti-map; c) EELS spectrum of the sample: confirming that deposition is amorphous  $\text{TiO}_2$ ; d) Schematics of  $\text{TiO}_2$  ALD inside silica nanopores (adopted from Ying-Bing Jiang<sup>126</sup>).

As shown in Figure 5.3, applying 1 layer of  $\text{TiO}_2$  thermal ALD didn't affect the mesoporous silica thin film structure spanning the FIBed hole.

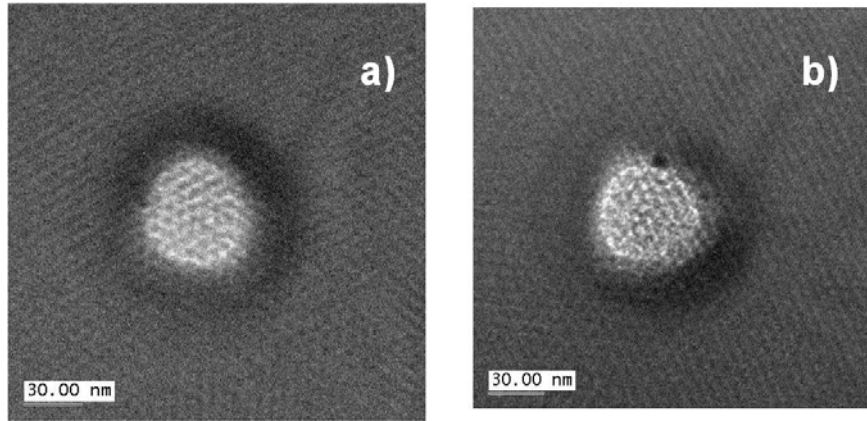


**Figure 5.3** TEM plan views of silica thin film on FIBed hole, a) before, and b) after 1 layer of thermal TiO<sub>2</sub> ALD.

### **5.1.2 TiO<sub>2</sub> ALD to enhance the stability of silica thin film in high ionic solution**

When we apply our silica thin film in DNA translocation, enhancing the stability of silica thin film in high ionic solution is important because most previous experiments of DNA translocation were conducted in buffer solution with high ionic concentration (1M KCl etc). In Figure 5.4, both film thickness and refractive index of the film can sustain high ionic solution (7.5% KCl) much longer after 2 layers of TiO<sub>2</sub> ALD.

As shown in Figure 5.5, the Bragg reflection pattern was almost completely diminished after putting original silica thin film in high ionic solution for 4.5 hrs. On the

contrary, the Bragg reflection pattern for 2-layer TiO<sub>2</sub>-ALD silica thin film was still remained after emerging the sample in high ionic solution for over 22 hrs.

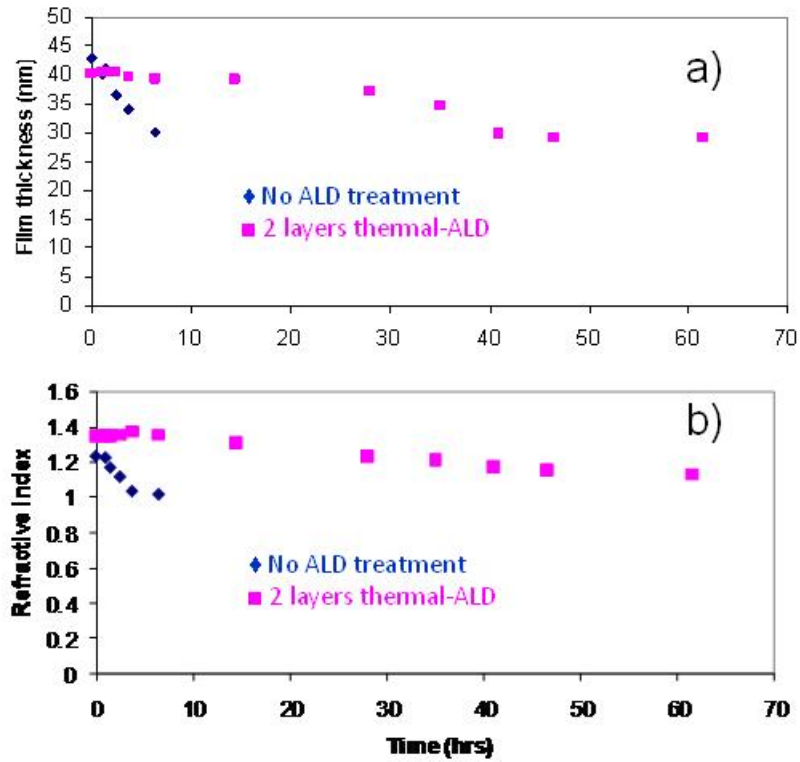


**Figure 5.4** Comparison of film stability regarding film thickness and refractive index as a function of time after emerging film in 7.5% KCl aqueous solution before and after 2 layer of TiO<sub>2</sub> thermal ALD.

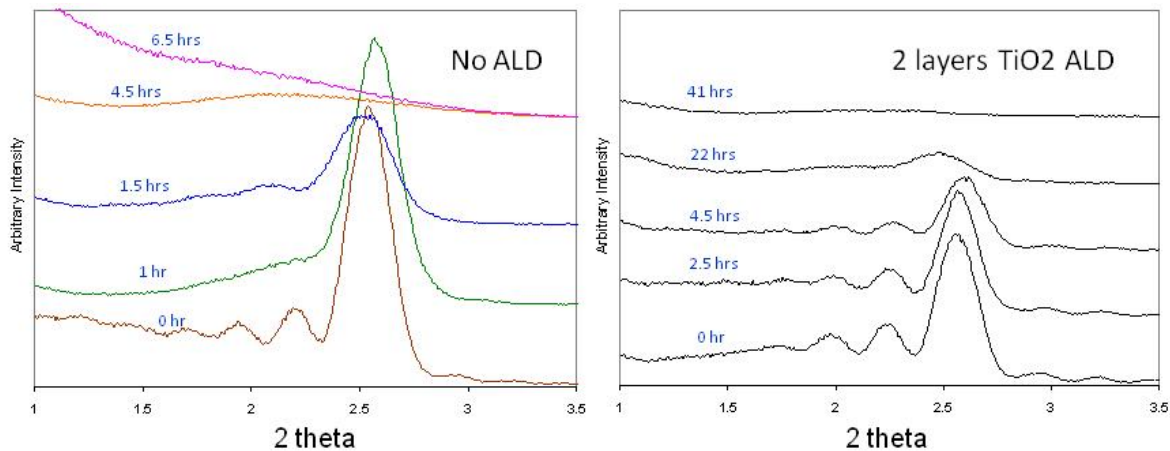


**Figure 5.5** Comparison of film stability a) before, and b) after 2 layers TiO<sub>2</sub> ALD by measuring 1-D low angle x-ray diffraction pattern of the same thin film after emerging in 7.5% KCl aqueous solution for different amount of time.

## 5.2 Aminopropyl trimethoxysilane ALD

We also applied ALD to form a coherent aminopropyl silane monolayer, using aminopropyl trimethoxysilane (APTMS) as a precursor. Successive cycles of APTMS and H<sub>2</sub>O favors condensation reactions between alkoxy silane groups on APTMS and silanol groups on the pore surface or between alkoxy silane groups of nearby APTMS, resulting in an aminopropyl silane monolayer as opposed to a multilayer<sup>130</sup> (see Figure 5.6). The Fourier-transform infrared (FTIR) spectrum (Figure 5.7) after one cycle of APTMS/H<sub>2</sub>O shows two new vibrational bands appear attributable to N-H bending (scissoring) of primary amines (around 1650 cm<sup>-1</sup>) and C-H stretching of alkyl chains (around 2900 cm<sup>-1</sup>) respectively, consistent with an APTMS monolayer.



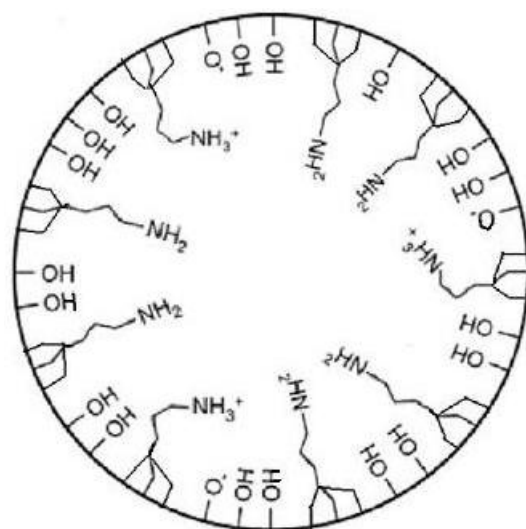


**Figure 5.6** Hypothetical schematic of the pore cross-section after successive ALD half cycles of APTMS and water.

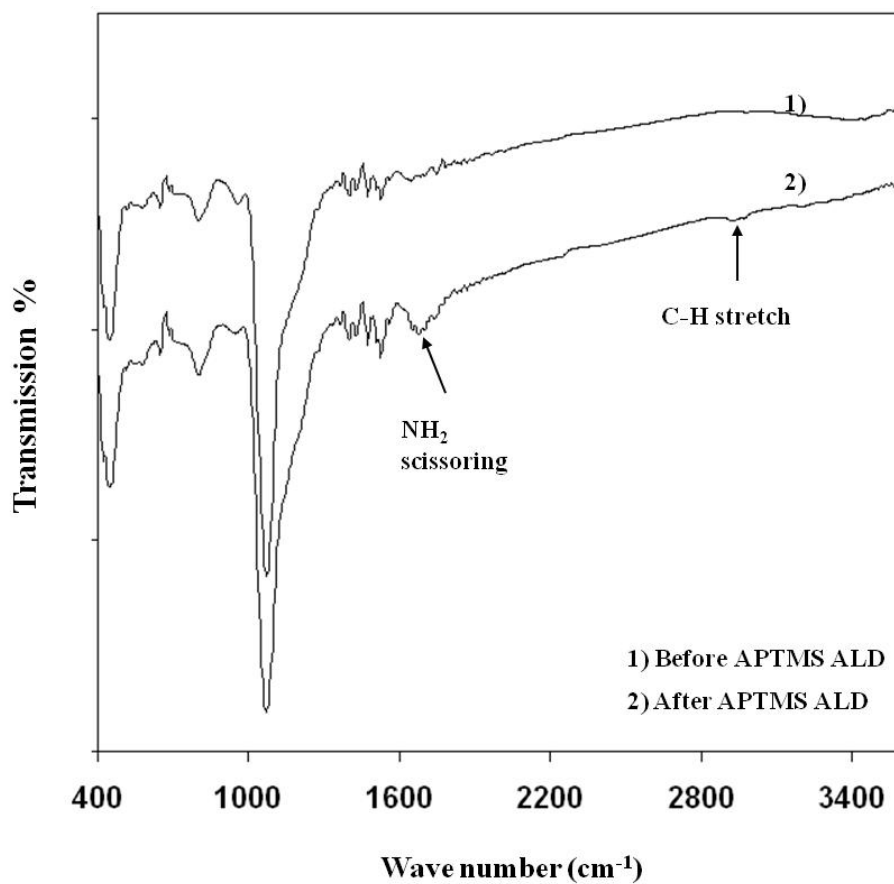


**Figure 5.7** FTIR spectrum of mesoporous silica thin film before and after ALD of APTMS.

APTMS ALD is interesting in this research for DNA translocation experiments because it provides some unique features compared to TiO<sub>2</sub> ALD: 1) Based on ellipsometric measurements of the thickness of the corresponding film deposited by ALD

on a solid silica support, we estimate that one layer of APTMS reduces the pore diameter ca. 1.2-nm, which means, for our 2.6-nm nanopore array system, the final pore diameter after one layer of APTMS is ca. 1.4 nm, comparable to that of  $\alpha$ -hemolysin; 2) The partial positive surface charge of the aminopropyl groups ( $\text{NH}_3^+$ ) introduces an attractive electrostatic DNA-pore interaction during DNA translocation, a factor which had been reported to enhance DNA translocation<sup>131</sup>.

### 5.3 Piranha treatment

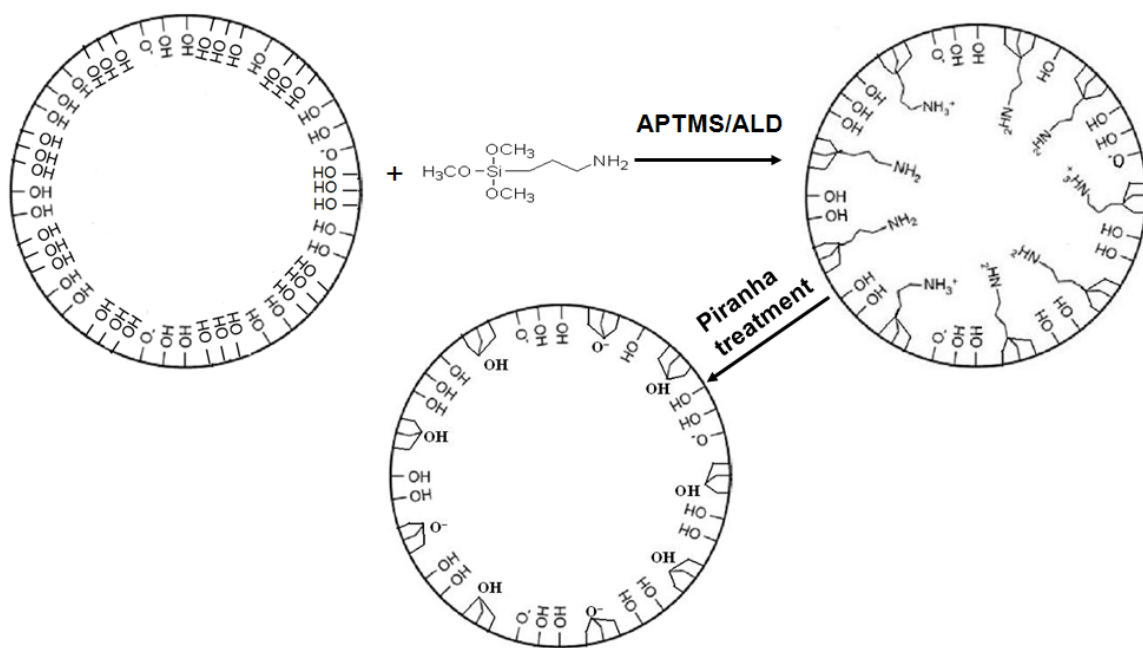


**Figure 5.8** Schematic of surface chemistry of nanopores before/after APTMS modification, followed by piranha treatment.

Piranha solution had been reported to effectively remove the organic groups<sup>132</sup>. Figure 5.8 shows that the organic part of APTMS is removed after piranha treatment, replaced by the hydroxyl groups that are attached to the silica surface. FTIR data of

APTMS-modified thin film after piranha treatment (Figure 5.9) verifies that C-H stretching vibration band of alkyl chain (around  $2900\text{ cm}^{-1}$ ) disappears, while broad O-H stretching vibration band ( $3200\text{-}3600\text{ cm}^{-1}$ ) appears after piranha treatment, indicating the removal of organic ligands and the generation of many silanol groups on pore surface. Contact angle data (not shown here) show that the membranes are more hydrophilic after piranha treatment, consistent with FTIR data of more silanol groups. One advantage of piranha treatment over calcination method for organics removal is that the silica structure doesn't shrink after piranha treatment. Ellipsometry and X-Ray-Diffraction (XRD) data (see Figure 5.10 and Table 5.3) show that piranha treatment doesn't change film thickness and d-spacing, while calcination dramatically shrinks the film. Highly ordered film structure is maintained in both cases.

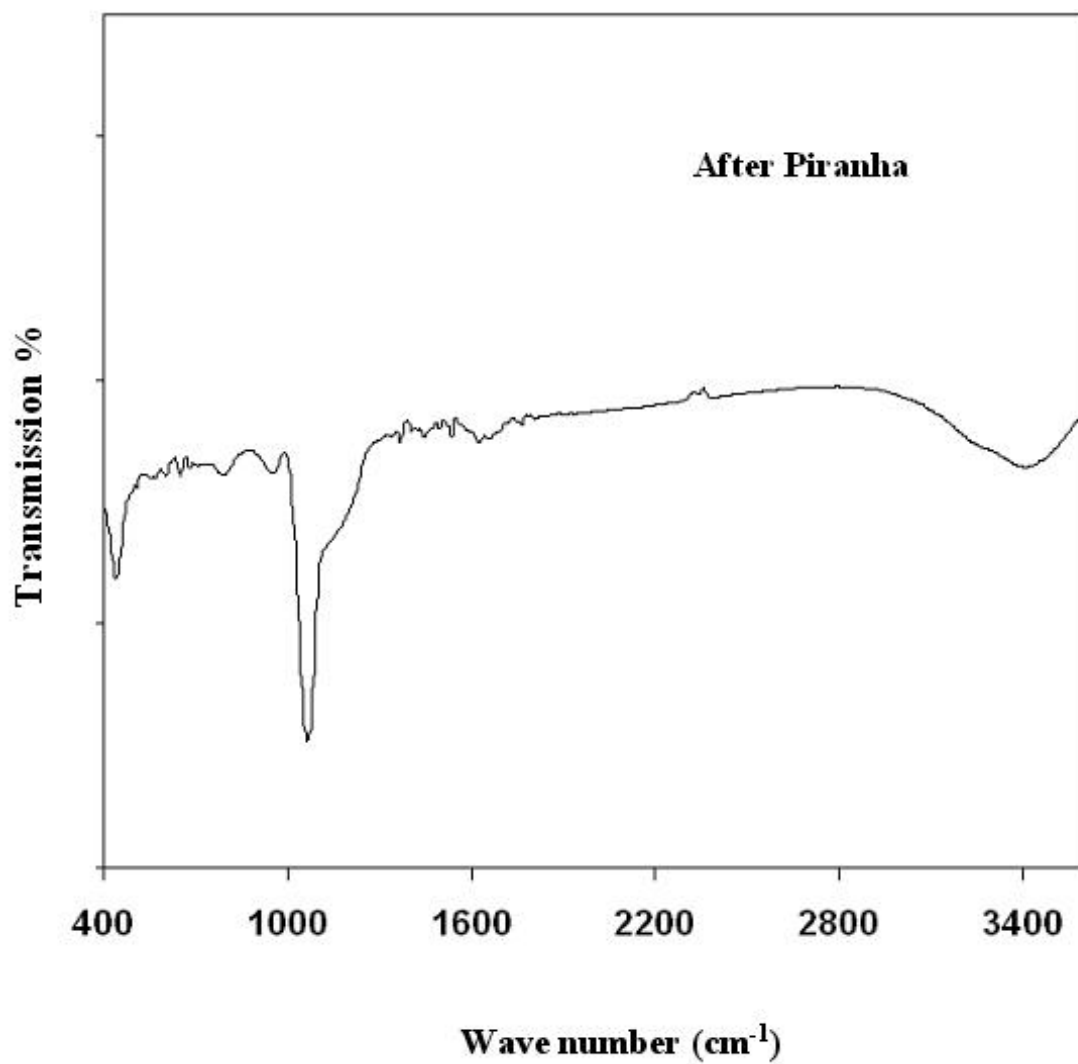


**Figure 5.9** FTIR of APTMS-modified silica thin film after piranha treatment.

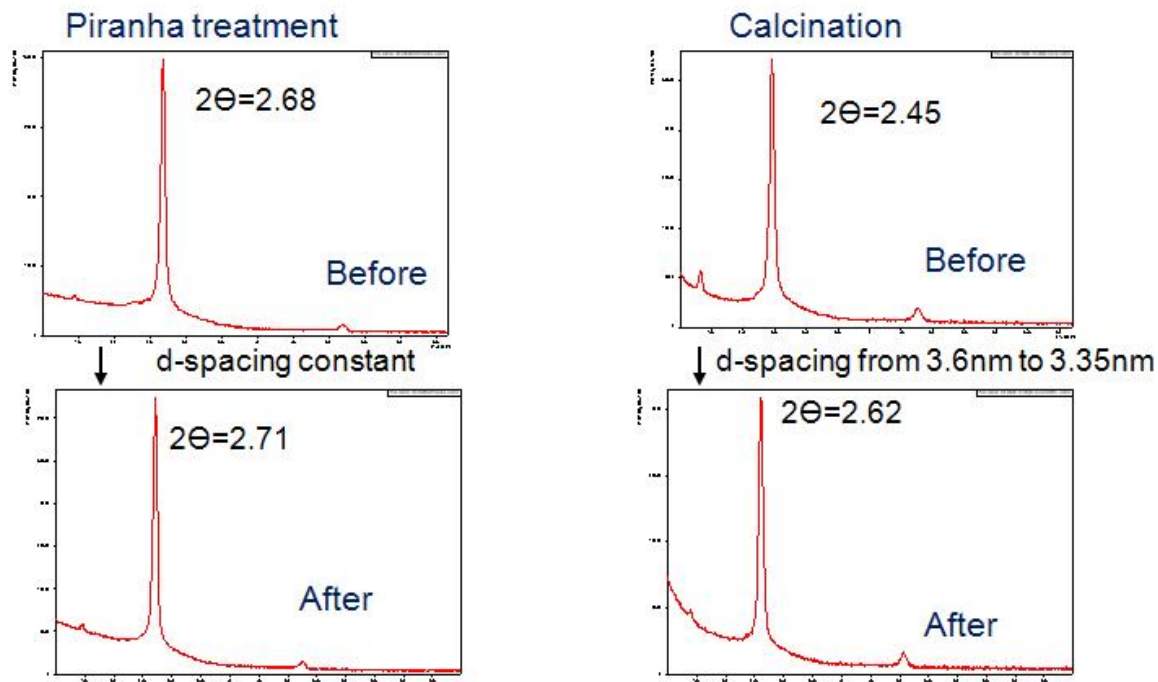


**Figure 5.10** Low angle 1D-XRD data of stabilized mesoporous thin films (pretreated at 400°C to remove the surfactant) treated in piranha solution for 20 mins and at 400°C for 3hrs respectively, showing piranha treated sample maintains the same d-spacing, while calcination treated sample shrinks. Both samples remain the highly ordered mesoporous structure, indicated by the intense primary peak of low-angle XRD.

	Film thickness (nm) (before)	Film thickness (nm) (after)
Piranha treatment For 20min	280	285
400C calcination 3.0hrs	275	232

**Table 5.3** Film thickness data obtained from ellipsometer measurement, showing piranha treatment does not change film thickness (within measurement error), while calcination dramatically shrinks the film.

Therefore, piranha treatment is a good approach to remove the organic groups that had been introduced to the pore surface by ALD. With the porous structure well maintained after piranha treatment, we can resume the original pore size and pore surface chemistry after APTMS ALD. In another word, surface modification by APTMS ALD becomes a reversible process, which can be used to demonstrate some interesting features of DNA translocation, as will be discussed in the next chapter.

## Chapter 6

### Results and Discussions III: DNA translocation

#### 6.1 dsDNA translocation through 2.6nm nanopore

A representative ionic current versus time trace for voltage-driven dsDNA translocation through a 2.6-nm diameter silica nanopore array is shown in Figure 6.1a. In this experiment, 2.7kbp dsDNA was introduced to the *-cis* side of the cell and a potential of +200mV was applied to the *-trans* side. A series of current blockage events are observed. Reversing the voltage bias or replacing dsDNA with blank buffer solution suppressed all current blockage events, implying the observed blockages are caused by dsDNA translocation. The background current (~23000pA) represents the collective ion current through all the nanopores on the aperture (estimated to be ~80 pores in this case). Correspondingly, it is greater than that of a single nanopore system<sup>133-135</sup> and scales with the size of the aperture and number of pores in the array. However, the current blockage amplitude (~200pA @200mV) per event is comparable to that reported previously for single nanopores<sup>136</sup>. We claim that each current blockage represents a single event of one dsDNA molecule passing through an individual pore, while the overall current blockage frequency is the sum of the dsDNA translocation events on all nanopores supported over the FIBed aperture. Because the translocation time  $\tau$  (<1ms) is short compared to the event frequency (0.5-1 sec/event), the probability of two events coinciding is very rare, implying that in our array, dsDNA translocation characteristics of individual pores can still be detected and interpreted as for single nanopore systems.



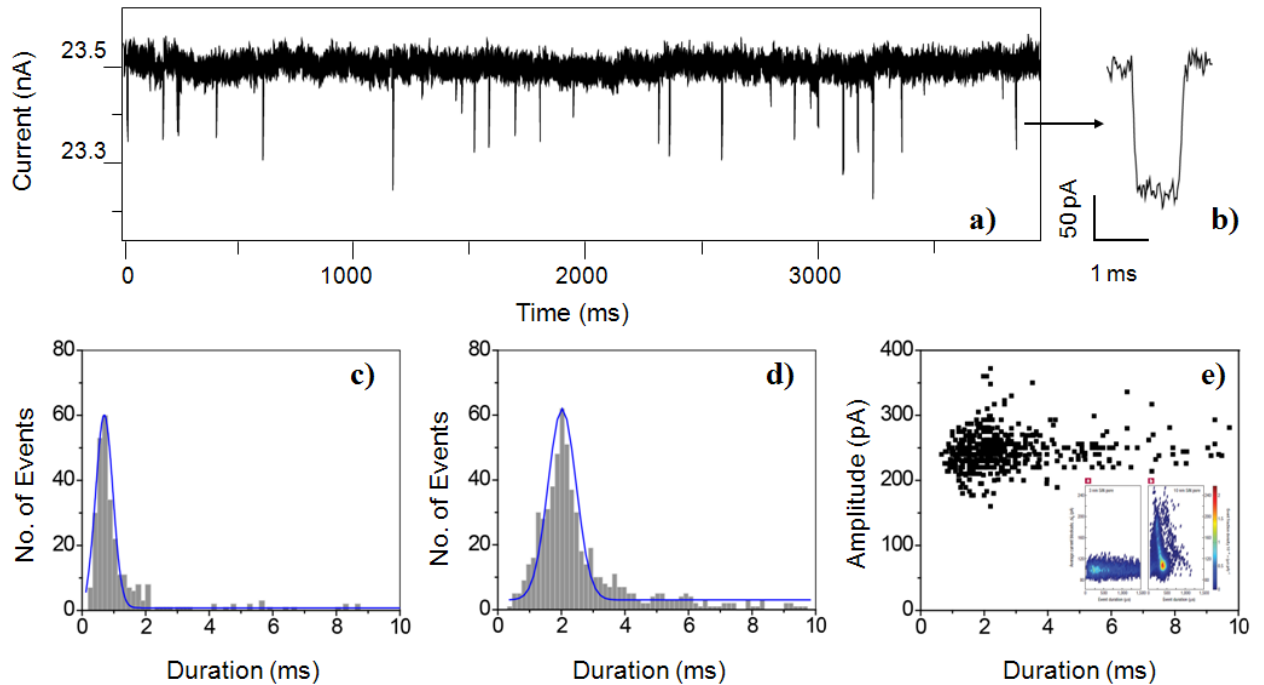


**Figure 6.1** a) A typical trace of current as a function of time during dsDNA translocation, showing a series of current blockages; b) Magnification of a single current blockage event; c) Duration histogram of 2.7k bp DNA translocation events for 2.6-nm diameter silica nanopore array; d) Duration histogram of 2.7k bp DNA translocation events for the silica nanopore array as in (c) after one cycle of thermal TiO<sub>2</sub> ALD which reduces the pore diameter to about 2.3-nm; e) A typical event scatter diagram of amplitude and duration for 560 current blockage events for the nanopore array after 1 cycle of TiO<sub>2</sub> ALD as in (d); the inset contains the event scatter diagrams of amplitude and duration for a 3 nm pore (left) and a 10 nm pore (right) in other solid-state nanopore system (adopted from Li et al.<sup>134</sup>). Applied voltage is 200 mV for all experiments. Events with duration longer than 10ms were also observed but not displayed in the histogram.

Figure 6.1c shows that the most probable dsDNA translocation time  $\tau$  in 2.6 nm pores is 0.7 ms, corresponding to a velocity of 1.3mm/sec, calculated from  $v = L_{\text{DNA}}/\tau$ <sup>136, 137</sup>, in which  $L_{\text{DNA}}$  is the polymer length, almost an order of magnitude less than that reported elsewhere using larger solid-state nanopores<sup>134, 136-138</sup>. One cycle of TiO<sub>2</sub> ALD reduces the pore diameter by  $\sim 0.3$ -nm (to  $\sim 2.3$ -nm) and further reduces the velocity by

about a factor of 3 ( $\sim 0.45$  mm/sec) (Figure 6.1d). This large dependence of velocity on pore size is consistent with a strong polymer-pore interaction<sup>71, 139, 140</sup> (see further discussion below).

Meanwhile, as shown in Figure 6.1e, a typical event scatter diagram of amplitude and duration for our nanopore array after 1 cycle of TiO<sub>2</sub> ALD is compared with the event scatter diagrams for a 3 nm pore (left diagram of the inset) and a 10 nm pore (right diagram of the inset) reported in another solid-state nanopore system<sup>134</sup>. The results show that the event scatter diagram for our 2.6 nm nanopore array system is similar to that for the other 3 nm solid-state single nanopore system: both have wider distribution of duration and narrower distribution of current blockage amplitude. On the contrary, the event scatter diagram for the other 10 nm solid-state single nanopore system shows narrower distribution of duration but wider distribution of current blockage amplitude, which is reasonable because both single-level events and multi-level events are allowed to translocate through a 10 nm pore. Because only events with duration in the range of 0 – 1.5 ms were shown for the other 3 nm solid-state single nanopore system, there is not enough information about the exact distribution of duration in that case. However, we suggest that the wide distribution of duration for our 2.6 nm nanopore array is representative to the transport characteristics in a very small pore system arising from the increased frictional force in the pore, even though it is reasonable to assume the nanopore array may show a wider distribution of duration compared to single nanopore due to the tiny difference (pore size and pore shape) of individual pores in the array.

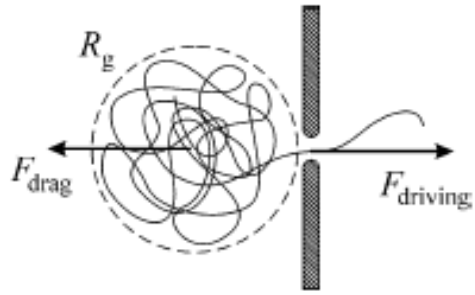


**Figure 6.2** The balance between the two dominating forces determines the dynamics of DNA translocation through a nanopore (adopted from Storm et al.<sup>114</sup>).

According to Storm et al.'s model<sup>114</sup>, the driving force derived from the potential drop (due to applied voltage) inside the pores is balanced with drag force as shown in Figure 6.2. DNA polymer can sense the potential drop because of the electronic charge on DNA. The driving force can be estimated to be maximally equal to  $F_{drive}=2eV/a$ , where  $e$  is the elementary charge,  $V$  is the applied voltage and  $a$  is the distance of nearby nucleotides, assuming the potential drop to completely apply inside the pore. Although screening effects will greatly reduce the effective charge on the DNA, and thereby the driving force, DNA translocations are strongly driven, as compared to the diffusive contributions. On the other hand, drag force is composed of hydrodynamic friction inside the pore and hydrodynamic drag on the untranslocated part of the polymer outside of the pore. In sufficiently shallow solid-state pores with comparatively large pore diameter, hydrodynamic friction on the part of the polymer outside the pore is the dominant force counteracting the driving force. Accordingly, Storm's model predicts a power-law relation between the dwell time  $\tau$  and the contour length of DNA  $L_0$ :  $\tau = l^\alpha$ . Experimental

results for the translocation of DNA fragments from 6557 to 97000 base pairs DNA in 10nm diameter nanopore show  $\tau \sim l^{1.27}$ , which is consistent with the prediction from the model.

In contrast, for dsDNA translocation through our 2.6 nm nanopore array system, the translocation time  $\tau$  scales linearly with polymer length  $l$ , as shown in Figure 6.3a. Such linear dependence of  $\tau$  on DNA length had also been reported by Kasianowicz<sup>21</sup> and Meller<sup>71</sup> for  $\alpha$ -hemolysin biological pores. This can be explained if hydrodynamic friction within the pore dominates the transport dynamics. In this case, the constant driving force  $F$  experienced by the polymer within the pore ( $F = 2eV/a$  where  $e$  is the elementary charge,  $V$  is the potential difference, and  $a$  (= 0.4-nm) is the spacing between nucleotides) is balanced by the hydrodynamic friction within the pore  $= \xi_{\text{eff}}v$ , where, ignoring any specific DNA-pore interactions,  $\xi_{\text{eff}}v = 2\pi\eta L_{\text{pore}}rv/(R-r)$  (where  $\xi_{\text{eff}}$  is effective friction constant,  $R$  is the pore radius,  $r$  is the ds-DNA cross-sectional radius,  $\eta$  is the solvent viscosity,  $L_{\text{pore}}$  is pore length and  $v$  is the linear velocity of the polymer inside the pore). This implies the translocation velocity  $v$  to be constant with polymer length as we observe. For  $\alpha$ -hemolysin biological pores, it is speculated that significant specific interactions between pores and passing polymers occur, which is the possible reason for a large pore friction. For our nanopore array system, considering the geometric factor in the effective friction constant  $\xi_{\text{eff}}$ , the combined effects of the tortuous shape of the pores as well as the comparatively small pore size as to dsDNA possibly lead to pore-friction-dominated translocation.

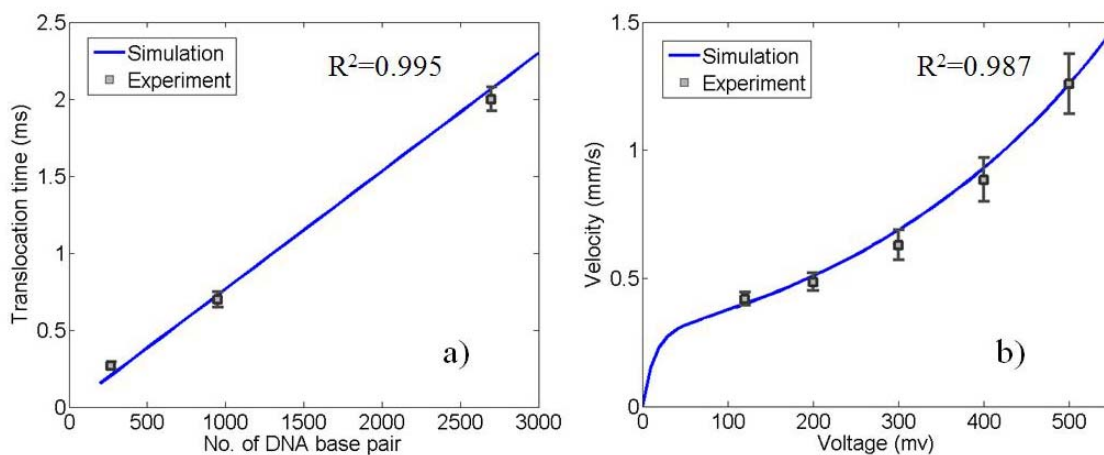


**Figure 6.3** a) Dependence of translocation time of dsDNA on size (270bp, 950bp and 2.7k bp respectively); b) Translocation velocity as a function of applied voltage for 950bp dsDNA. The error bars denote standard deviation evaluated from dwell-time histograms. Simulated data (as shown in blue) is based on a 1D drift-diffusion model, as described in the transport model part. Coefficient of determination ( $R^2$ ) provides a measure of how well the experimental data are likely to be predicted by the model.

Additionally, because ALD deposition is conformal and changes the pore size but not its shape, we can use the above force balance to estimate the velocity ratio  $v_1/v_2$  in reducing the pore radius from  $R_1$  to  $R_2$  at a constant driving potential. Reducing  $2R$  from 2.6 to  $\sim 2.3$ -nm (Table 5.1 and 5.2) should reduce  $v$  by a factor of about 2. Experimentally we observe a factor of 3, suggesting additional frictional forces arising from specific polymer-pore interactions or, more likely, the tortuous pore shape defined by the micellular mesophase<sup>114</sup>. A second cycle of  $\text{TiO}_2$  ALD reduces the pore diameter to 1.9-2.0-nm, below that of dsDNA, and, as expected, we observe no measurable dsDNA translocation (for driving potentials less than 500mV where we expect there to be no denaturation).

A final dynamical feature of our nanopore system is the approximate quadratic relationship between velocity and voltage (Figure 6.3b). Once again, this is similar to transport characteristics of protein nanopores<sup>71</sup>, but different from those reported for straight through solid-state nanopores with comparatively large pore size<sup>136</sup>.

The transport characteristics of the kinked nanopore arrays we describe above are distinct from other solid-state nanopores<sup>114, 140</sup> and more similar to protein nanopores. For example, Storm *et al* observe the translocation time in 10-nm diameter solid-state nanopores to vary with dsDNA length as a power law,  $\tau \sim l^{1.27}$ , which they attribute to the condition where hydrodynamic drag imposed by the untranslocated polymer on the *cis* side dominates the friction within the pore. In fact they conclude that the essential difference between solid-state and protein pores is that, for sufficiently shallow solid-state pores, the effect of friction within the pore is negligible. In comparison, for ssDNA translocation through  $\alpha$ -hemolysin<sup>21, 71, 141</sup> Kasianowicz<sup>21</sup> and Meller<sup>71</sup> found the translocation time to vary linearly with polymer length, consistent with pore-friction-dominated translocation due to the small 1.4-nm diameter pores plus possible specific DNA-pore interactions.

## **6.2 ssDNA translocation through 1.4-nm nanopore after monolayer ALD of amino ligand**

As described above, the transport characteristics of the kinked nanopore arrays are distinct from other solid-state nanopores<sup>114, 140</sup> and more similar to protein nanopores. This encourages us to emulate protein nanopores by modifying our 2.6 nm nanopores to comparable pore size of protein nanopores. As demonstrated in Chapter 5.2, one layer of

APTMS ALD allows us to reduce the pore diameter from 2.6 nm to 1.4 nm, which is comparable to  $\alpha$ -hemolysin nanopores with 1.4 nm pore diameter at restriction area. Additionally, the partial positive surface charge of the aminopropyl groups ( $\text{NH}_3^+$ ) introduces an attractive electrostatic DNA-pore interaction, a factor which had been reported to enhance DNA translocation<sup>131</sup>.

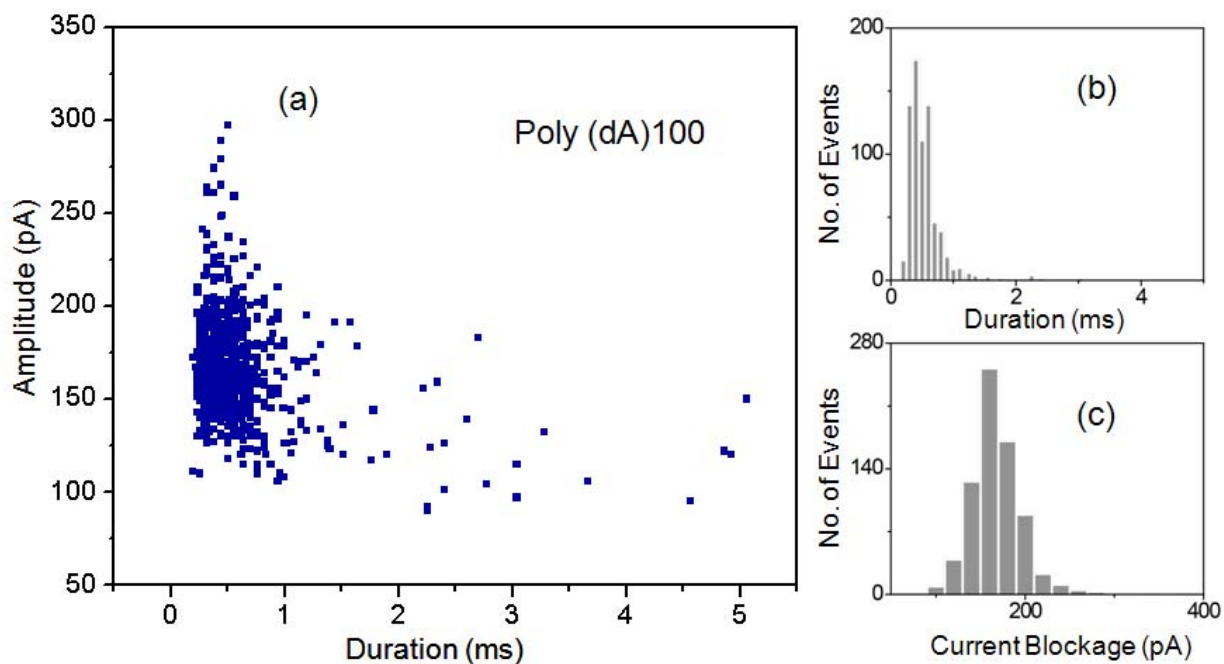


**Figure 6.4** Event diagram of poly(dA)<sub>100</sub> in our nanopore array system after APTMS ALD treatment, given -400mV on *-cis* side (a) and corresponding duration histogram (b) and current blockage histogram (c).

For the APTMS-modified nanopore array, no current blockages were observed for 2.7Kbp dsDNA. For pure poly(dA)<sub>100</sub> current blockage events were observed, and the corresponding translocation times and current blockages are shown in the histogram in

Figure 6.4a. When poly(dA)<sub>100</sub> was added to 2.7Kbp dsDNA, current blockages were again observed and the duration and current blockage histograms were similar to those of pure poly(dA)<sub>100</sub>, indicating the observed current blockages were caused by the translocation of poly(dA)<sub>100</sub>. To further verify the selectivity of ssDNA over dsDNA is due to the APTMS modification on nanopores, we treated the above ALD treated sample in piranha solution with gentle heating for 20 mins to remove the organic groups that had been introduced on pore surface by ALD. After the removal of organic ligands on APTMS, current blockages were observed when pure 2.7Kbp dsDNA was added in –cis side, as plotted in red in Figure 6.5. However, comparing the event scatter diagram of pure 2.7K bp dsDNA translocating through piranha treated sample and that of pure poly(dA)<sub>100</sub> translocating through APTMS modified sample (black spots represent poly(dA)<sub>100</sub> translocation events in APTMS modified film and red spots represent dsDNA translocation events in piranha treated film, same voltage was applied), we found that amplitude of current blockage of poly(dA)<sub>100</sub> case is considerably lower than that of dsDNA case. Two issues might contribute to this observation: 1) Because both ssDNA and dsDNA translocate through the pores in linear manner, ssDNA expels fewer ions than dsDNA during translocation due to its smaller cross section diameter, resulting in smaller conductance decrease; 2) As APTMS ALD reduces the pore diameter from 2.6nm to 1.4nm, the ionic mobility is dramatically decreased due to the increased confinement, therefore causing the decrease of conductivity in nanopores which scales with ionic mobility in high ionic solution<sup>83</sup>. Compared to the transients of 2.7Kbp DNA in original 2.6nm nanopore membrane, the transients of 2.7Kbp DNA in piranha treated membrane have comparable current blockage amplitude, but longer duration (most



probable translocation time is between 1-2 ms compared to 0.7ms in 2.6nm membrane). One explanation is that after removal of the organic ligands by piranha solution, the siloxane bonds formed on pore surface during ALD are still remained, which result in a pore diameter smaller than 2.6nm. As shown in Chapter 5.3, piranha treatment will not change the periodic ordering and pore diameter of mesoporous silica thin film, indicating it is a good method to remove the organic groups from the inorganic framework without destroying its structure.

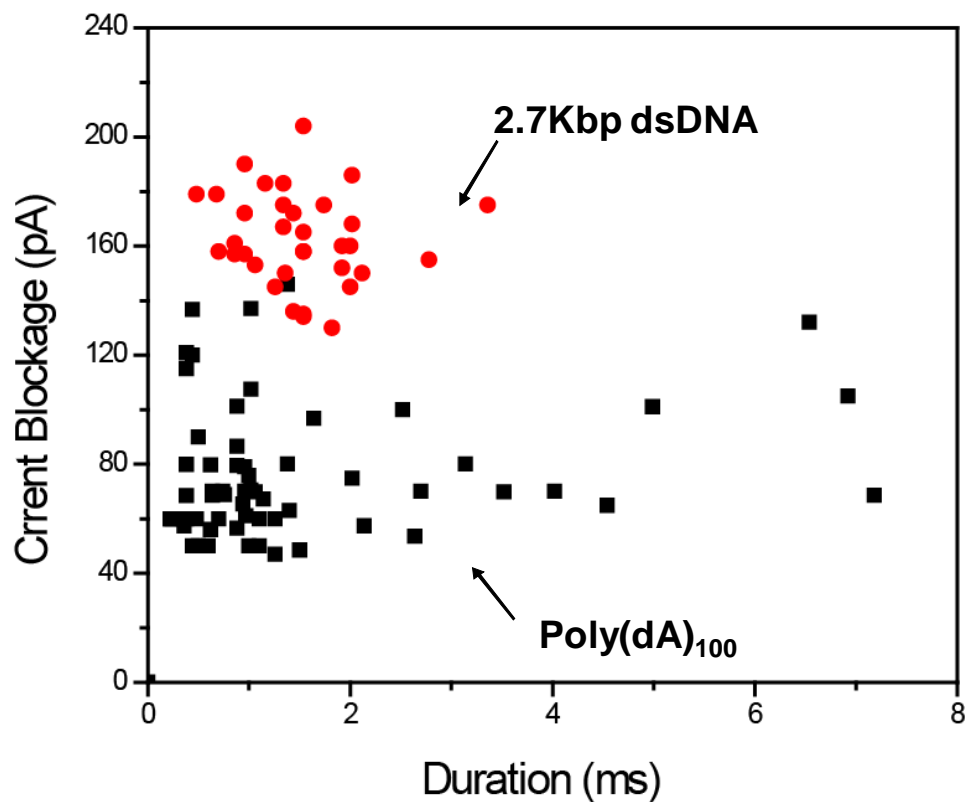


**Figure 6.5** Event diagram of poly(dA)<sub>100</sub> before piranha treatment (in black) and event diagram of 2.7Kbp linear dsDNA after piranha treatment (in red), when  $-200\text{mV}$  was applied on  $-cis$  side.

The above results strongly support that, after APTMS ALD, our nanopore array can achieve nearly perfect selectivity of ssDNA over dsDNA, verified by using quick electrical measurement and PCR. Meanwhile, treating APTMS modified sample with piranha solution removes the APTMS organic groups on pore surface, therefore destroys the selectivity of ssDNA over dsDNA. This further verifies that the interesting feature of perfect selectivity of ssDNA over dsDNA in our nanopore array system is achieved by introducing APTMS organic group on pore surface, which changes both the pore size and surface chemistry. By reversibly switching the dsDNA/ssDNA selectivity on/off with simple ALD and piranha treatment, as demonstrated above, our nanopore array system may find more opportunities as molecular sensor/manipulator in real-world applications.

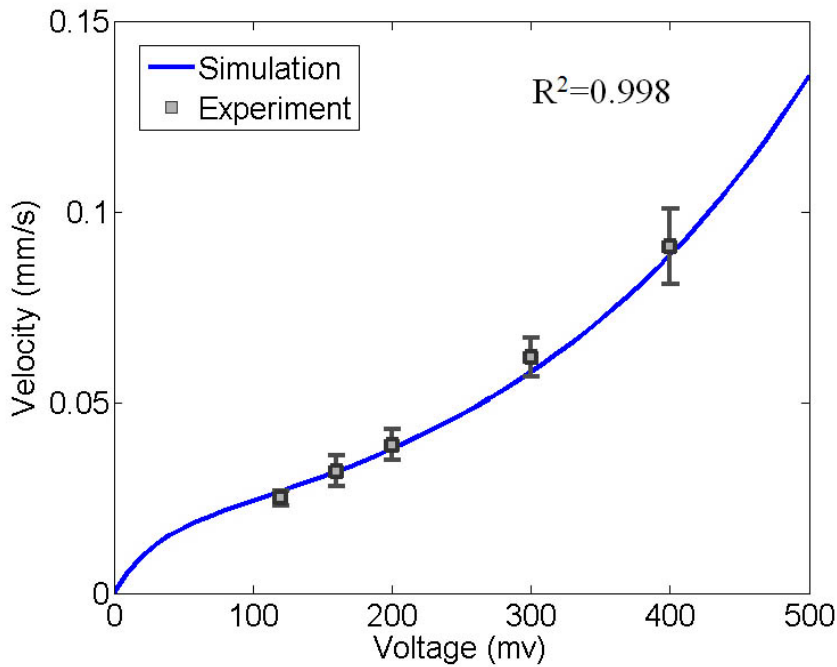


**Figure 6.6** poly(dA)<sub>100</sub> translocation velocity as a function of applied voltage for the APTMS modified pore. The error bars denote the standard deviation evaluated from dwell-time histograms. Simulated data (as shown in blue) is based on a 1D drift-diffusion model, as described in the transport model part. Coefficient of determination ( $R^2$ ) provides a measure of how well the experimental data are likely to be predicted by the model.

Figure 6.6 shows the velocity of poly(dA)<sub>100</sub> as a function of applied voltage in the APTMS-modified nanopore array. The velocity was calculated from the blockade duration half-life  $\tau$  (the time over which the current blockade increases and decreases by 50% of its maximum value) according to  $L_{DNA}/\tau$ , which is the appropriate relation for the condition where the polymer length  $L_{DNA} \cong$  the pore length  $L_{pore}$  (film thickness (30-nm) x tortuosity (1.5))<sup>71</sup>. We observe an approximate quadratic relationship between velocity and applied voltage similar to that reported for poly(dA) translocation through  $\alpha$ -hemolysin<sup>70, 71</sup>. However direct comparison of the translocation time of poly(dA)<sub>100</sub> through the APTMS-modified nanopore and  $\alpha$ -hemolysin under identical conditions (22°C, 120mV)<sup>23</sup> shows ~ 5x longer translocation time (1.6ms compared to 0.3ms) and, correspondingly slower translocation velocity for the APTMS-modified nanopore. Since the pores are of comparable diameters, we attribute this difference to the more tortuous shape of our solid state nanopore, most likely due to a higher energy barrier derived from the pore kinkedness. Our transport model further verifies the higher energy barrier in our tortuous nanopores compared to that in straight-through pores and clarifies the physical characteristics of the parameters used in the simulation, whose values can all be well explained by strong interaction between polymer and kinked pores.

### **6.3 Polymerase chain reaction (PCR) analysis to show DNA translocation**

To unambiguously demonstrate the selectivity of ssDNA over dsDNA after chemically modifying pore surface with aminopropyl trimethoxysilane (APTMS) with ALD, we first applied membrane with no ALD treatment in our cell device and introduced specific dsDNA and ssDNA (in this case 950bp dsDNA amplified from

pUC19 plasmid and 150b ssDNA with sequence described in Kasianowicz's paper<sup>21</sup>) individually in the -cis side of our cell. After applying external voltage to drive DNA moving toward -trans side for 1 hr, we collected solution from -trans side for each experiment. Then, we applied APTMS modified membrane in our cell device and repeated the above experiments with exactly the same procedure. To ensure the translocated polymers are not lost or washed away, the volume of total solution on the -trans side was carefully collected, especially for the area close to the membrane and the electrode. A few rinsing steps were conducted and the rinsing solution was also collected. Before applying PCR amplification, we concentrated the DNA in the above -tran solution using a cold ethanol precipitation protocol. After PCR amplification with well-designed high-specificity primers, we run electrophoresis and the results are shown as in Figure 6.7. Lanes 1, 3 and 4 have single band after gel electrophoresis, representing the presence of one single length of DNA in each case after PCR (950bp for lane 1 and 150b for Lane 3 & 4). The results are consistent with DNA translocation results, showing dsDNA can only go through the pores before APTMS modification, while ssDNA can go through the pores before and after APTMS modification.

We also conducted control experiments to make sure no contamination of DNA in DNA translocation experiments by collecting solution from -trans side after DNA was introduced in -cis side but no external voltage was applied. For both ssDNA and dsDNA, no band was observed after PCR amplification of -trans solution followed by gel electrophoresis.

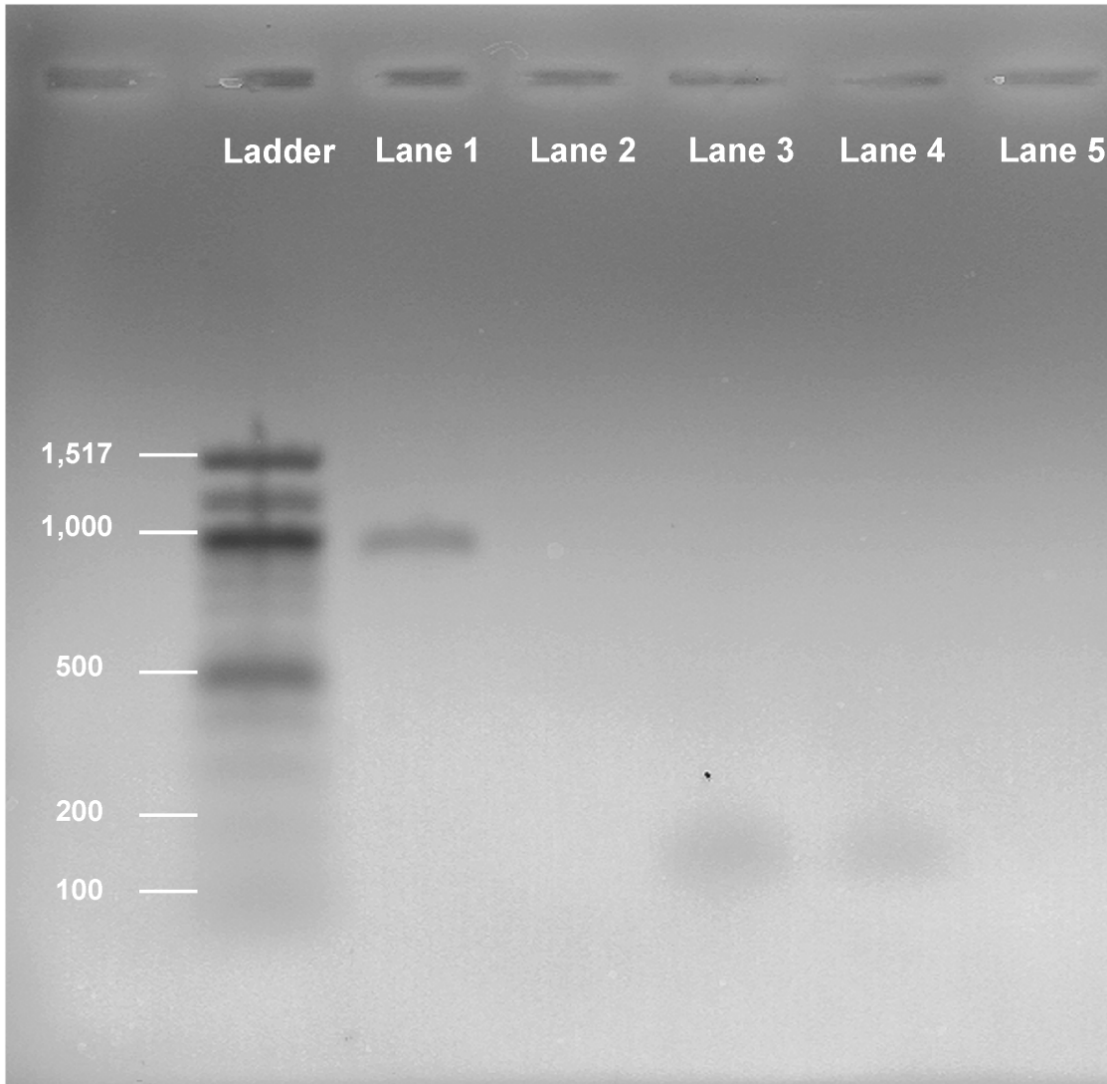


**Figure 6.7** Lane 1: -trans solution after 950bp dsDNA in -cis was driven through membrane with 2.6-nm pores; Lane 2: -trans solution after 950bp dsDNA in -cis was driven toward membrane with 1.4-nm pores (after APTMS ALD treatment); Lane 3: -trans solution after 150b ssDNA in -cis was driven through membrane with 2.6-nm pores; Lane 4: -trans solution after 150b ssDNA in -cis was driven through membrane with 1.4-nm pores (after APTMS ALD treatment); Lane 5: -trans solution when 150b ssDNA was present in -cis side but no external voltage was applied.

Polymerase chain reaction (PCR) analysis show that dsDNA translocation was successful in original nanopore array with ca. 2.6 nm pore diameter, but was rejected in

APTMS-modified nanopore array with ca. 1.4 nm pore diameter; ssDNA translocation was successful in both cases, consistent with the observation of translocation events from current blockage. These results strongly suggest: 1) with APTMS-modified nanopores, separation of ssDNA from dsDNA is achieved and can be sensed electronically; 2) pore size reduction by ALD occurs uniformly for all pores, allowing selectivity to be developed in an array format. Recently great efforts have been made to distinguish single- and double-stranded nucleic acid molecules using solid-state nanopores, which improve the prospects for using nanopore-based devices for DNA or RNA mapping<sup>142</sup>,<sup>143</sup>. Our work presented here, showing nearly perfect selectivity for ssDNA over dsDNA in ALD modified nanopores, could expand the range of potential applications of synthetic solid-state nanopores in biotechnology by narrowing down the pore size to a range in between the diameters of dsDNA and ssDNA.

#### **6.4 Transport model**

As mentioned before, Storm et al.'s model<sup>114</sup> fits well with DNA translocation data obtained from larger solid-state nanopores with straight pore morphology, but can not accurately explain the experimental data obtained from our kinked nanopore system with smaller pore size. On the other hand, inspired largely by the DNA translocation experiments conducted in  $\alpha$ -hemolysin biological pores, Lubensky et al.<sup>139</sup> proposed a simple microscopic model to explain the motion of a homopolymer threaded through a narrow pore with which it has strong interactions. In this 1-D drift-diffusion model, the role of polymer interactions with the pores is emphasized. As a result, it is argued that, in the presence of a force driving the polymer through the pores, there should be a regime in

which the polymeric degrees of freedom outside of the pore can be neglected, and the system is effectively one dimensional. In this part, we adopt this model and demonstrate that, the distinguishing transport characteristics of our kinked nanopore array, *viz.* linear dependence of translocation time on polymer molecular weight and quadratic dependence of translocation velocity on voltage, shared additionally by protein pores, are captured by a 1-D drift-diffusion model<sup>139</sup>:

$$\frac{\partial P}{\partial t} = D_0 \frac{\partial}{\partial x} \left[ \frac{\partial P}{\partial x} + \frac{1}{k_B T} \frac{\partial \Phi}{\partial x} P \right] \quad (1)$$

where  $P(x,t)$  is the probability that a length  $x$  of the polymer's backbone has passed through the pore at time  $t$ , and  $D_0$  is the diffusion coefficient, assumed to be  $10^{-8}$  cm<sup>2</sup>/s due to the confined environment<sup>144</sup>.  $\Phi$  is the potential due to the various interactions of the polymer with the pore and the applied voltage drop. The potential  $\Phi$  is approximated by the expression,

$$\Phi(x) = U(x) - Fx \quad (2)$$

where  $F$  is determined by the applied voltage drop, and  $U(x)$  represents the polymer's interactions with the pore.  $U(x)$  is assumed to be a sawtooth like potential, which is described by two dimensionless parameters, the peak height  $U_0 / k_B T$ , and the asymmetry parameter,  $\alpha$ . The value of  $\alpha$  depends on several factors including the pore geometry and  $U_0$  is the energy barrier DNA has to overcome, represented by the height of

the saw-tooth like potential, which also depends on several factors including the pore geometry and is typically of the order of several  $k_B T$ .

We have run extensive molecular dynamic (MD) simulations on DNA translocation through a smooth and kinked nanopore to understand the dependence of these two parameters on various interactions between DNA and the nanopore. In the case of the kinked pore, we varied the height of the kinkiness and small kinkiness (e.g. 0.1 nm) has a negligible effect on the pore length. Our simulations indicate that for DNA translocating through a kinked pore, as compared to a smooth pore, the energy barrier ( $U_0$ ) can be quite different. As shown in Figure 6.8 the energy barrier can be approximated by a saw-tooth like potential. Since the DNA-pore interaction is the dominant factor in determining DNA translocation in a small pore<sup>140, 145</sup>, this periodical barrier can be well explained from the interaction between DNA and the kinked pore. The saw-tooth-like force has also been observed while pulling a RNA/DNA through a nanopore<sup>146</sup> and unfolding single RNA molecules<sup>46</sup>. In the following discussion, prediction made by this 1D drift-diffusion model is compared with the experimental results to further demonstrate that it is reasonable to treat the interaction energy between DNA and nanopore as a saw-tooth-like potential.



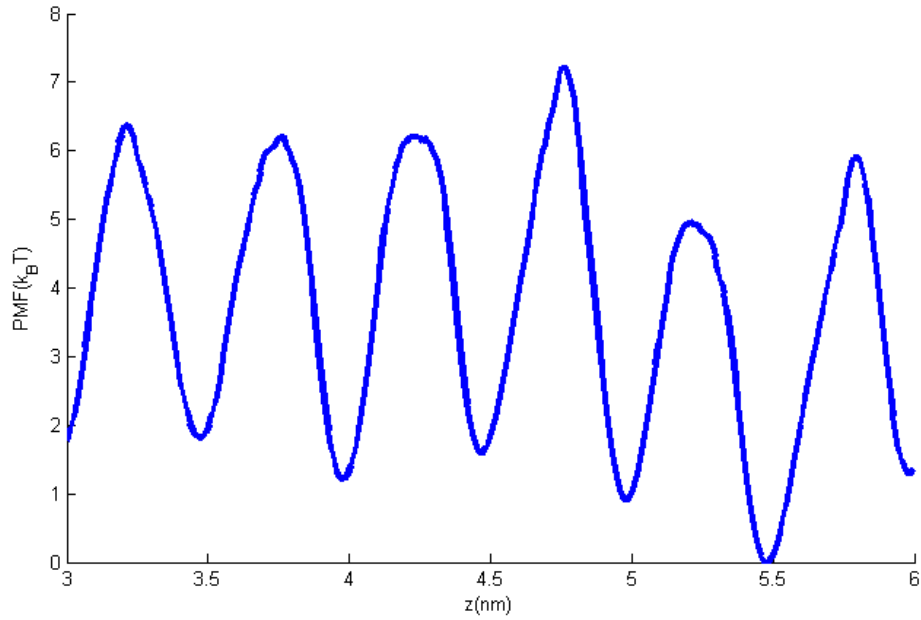


**Figure 6.8** Potential of mean force of DNA through a kinked nanopore obtained from MD simulations.

In the case of a strong polymer-pore interaction (characterized by a large  $U_0$ ), where diffusion can be described as hopping from one potential minimum to the next potential minimum, an approximate expression for the polymer velocity,  $v$ , can be obtained from Eq. (1) as<sup>139</sup>:

$$v \approx \frac{D_0}{aI_1^{(0)}I_2^{(0)}} \left[ \exp\left(\frac{\alpha Fa}{k_B T}\right) - \exp\left(-\frac{(1-\alpha)Fa}{k_B T}\right) \right] \quad (3)$$

where

$$I_1^{(0)} = \int_0^a \frac{1}{a} \exp\left(\frac{U(x)}{k_B T}\right) dx \quad \text{and} \quad I_2^{(0)} = \int_0^a \frac{1}{a} \exp\left(\frac{-U(x)}{k_B T}\right) dx$$

(4)

In our calculations for dsDNA, we assume  $a = 4 \text{ \AA}$ ,  $D_0 = 10^{-12} \text{ m}^2/\text{s}$ ,  $U_0 = 5.7k_B T$ , and  $\alpha = 0.04$ . Using these parameters, we compute the average velocity using Eq. (3).

The translocation time is then computed using the expression  $\tau = \frac{L_{DNA}}{v}$ , where  $L_{DNA}$  is the length of the DNA chain. In Figure 6.3 we compare our experimental results with predictions made by the 1-D drift diffusion model for dsDNA. We repeated the calculations for the poly(dA)<sub>100</sub> case using  $a = 4 \text{ \AA}$ ,  $U_0 = 9.7k_B T$ , and  $\alpha = 0.11$ . The calculations are compared with the experimental data in Figure 6.6. In the literature,  $U_0$  has been assumed to vary from 0 to 10  $K_B T$  and  $\alpha$  is assumed to vary from 0 to 1, where  $\alpha = 0$  when DNA is interacting with a reflecting boundary, and  $\alpha = 1$  when the DNA is interacting with an absorbing boundary<sup>147, 148</sup>. Our simulation results show that both  $U_0$  and  $\alpha$  values vary as a function of the kinkedness of the pore. For example, Lam et al. took  $U_0$  to be 4.5 $K_B T$  in a straight nanopore system and their results reasonably explained the experimental observations<sup>147</sup>. In our simulation,  $U_0$  value is higher for both dsDNA and ssDNA cases compared with the straight nanopore system. Since the DNA-pore interaction is the dominant factor in determining DNA translocation in a small pore<sup>140, 145</sup>, the higher energy barrier can be well explained from the stronger interaction between DNA and the kinked pore. Meanwhile, our simulation results show a comparatively low  $\alpha$  value. Since reflecting boundary is the case when the DNA is not able to pass through

the pore<sup>148</sup>, our result is consistent with the fact that as the kinkiness increases, the barrier increases, and the surface acts more like a reflecting boundary because the DNA has to adjust its orientation to climb over the wall (the kink). It is important to note that while these parameters are determined from the data of one single experiment, the same values are able to match data from a number of other experiments, suggesting the generality of these parameters for the DNA-nanopore interaction considered in our paper. The close correspondence of the experimental and predicted values emphasize that nanopore translocation can be adequately (although not explicitly) approximated through assignment of a potential that lumps together the physical and chemical features, pore size, shape, length, and interactions, that contribute to pore-friction dominated transport. It is reasonable to treat the interaction energy between DNA and the nanopore as a saw-tooth like potential. The potential we assumed is physically realistic, being within the range of  $U_o$  values determined by other authors to describe the barrier to permeation of ssDNA through  $\alpha$ -hemolysin.

## **6.5 Evaluation of noise level in nanopore array**

With all the promising features solid-state nanopores have offered for DNA and more broad polymer characterization, one limitation emerges as an obstacle for their utility as single-molecule detectors, as the electrical noise during ionic current measurement through solid-state nanopores is generally observed to be comparatively higher than  $\alpha$ -hemolysin biological pores<sup>149</sup>. To enhance the detection sensitivity that can be adversely affected by the noise and frequency response, great efforts had been made to explore strategies for improving the electrical performance. Regarding the high-

frequency noise associated with the relatively high capacitance of the SiN<sub>x</sub> membrane on the silicon support substrates (dielectric noise), Tabard-Cossa et al. demonstrated that curing polydimethylsiloxane (PDMS) on the nanopore support substrates can dramatically improve the dielectric properties of the support substrates by greatly reducing the dielectric noise. A most recent paper from Timp's group<sup>150</sup> presented four strategies to reduce the parasitic membrane capacitances using: (1) thick SiN<sub>x</sub> membrane; (2) miniaturized composite membranes consisting of SiN<sub>x</sub> and polyimide; (3) miniaturized membranes formed from metal-oxide-semiconductor (MOS) capacitors; and (4) capacitance compensation through external circuitry. Regarding the low-frequency current fluctuation with  $1/f^\alpha$  characteristics (flicker noise), by treating the SiN<sub>x</sub> pore with piranha solution<sup>149</sup>, or using surface chemical modification and control<sup>86, 151, 152</sup>, flicker noise can be largely suppressed. Meanwhile, extensive research on noise power as a function of salt concentration had been conducted<sup>150, 153, 154</sup>.

Regarding our nanopore array system, there is one more concern compared to single solid-state nanopore systems that having many pores in tandem only serves to increase the noise in the current signal. As overall current is proportional to the number of presented pores, it is reasonable to conduct noise vs. overall current relationship as a measure of pore number influence on noise level. We will demonstrate the noise level as a function of overall current as a means to address the above concern.

We conducted a series of experiments to record the current-time trace as we systematically increased the number of pores at open-state. To do this we first treated our film in 6% hexamethyldisilazane (HMDS) in hexane solution over night. The ionic

current was initially zero because the pores were hydrophobic preventing water and ion transport. Then, we removed the sample and exposed both sides to UV/ozone for a short time thereby converting hydrophobic trimethylsilyl groups to hydrophilic hydroxyl groups. This resulted in a measurable ion current. Repeating this process many times successively opens more pores, thereby resulting in proportional increased overall current. In doing so we observe that the current power spectral density (PSD) is not proportional to the overall current value, corresponding to the number of open pores. For example at 200mV, we obtained PSD versus frequency for overall current of 0, 185, 800, 2000 and 10000 pA, corresponding to 0, 1, 4, 10 and 50 open pores respectively (Fig 6.9). 1M KCl solution buffered at pH8.0 was used and current was recorded at a 100 KHz sampling rate with low-pass four-pole Bessel filter of 10 KHz. We found that the noise spectrum <1 kHz is more sensitive to the overall current value (or number of open pores) than the high frequency noise. For no open pore case (blue line), 1/f low-frequency noise is a few order of magnitude lower than one open pore case (red line). When more pores were open, 1/f low-frequency noise were only slightly increased and had no dramatic change when open pores were increased from 1 to 50. Meanwhile, we measured current noise from the current-time traces recorded under the same conditions as described in Figure 6.9 for the cases of 0, 185, 800, 2000, 3000 and 10000 pA overall current (corresponding to 0, 1, 4, 10, 15, 50 open pores). As shown in Figure 6.10, the current fluctuations were 25, 35, 45, 50, 50, 50 pA respectively, consistent with current power spectra density results at low frequency, indicating the low-frequency noise level as well as current fluctuations in our nanopore array system are not dramatically enhanced compared to the single nanopore system. Although no entirely satisfactory physical explanation for low-frequency noise

has been developed, the noise can be suppressed using piranha solution treatment and surface chemical modification<sup>149</sup>. Based on the above results, we believe introducing a pore array doesn't necessarily dramatically enhance the noise level or current fluctuation during DNA translocation, which is the case in our DNA translocation measurement.

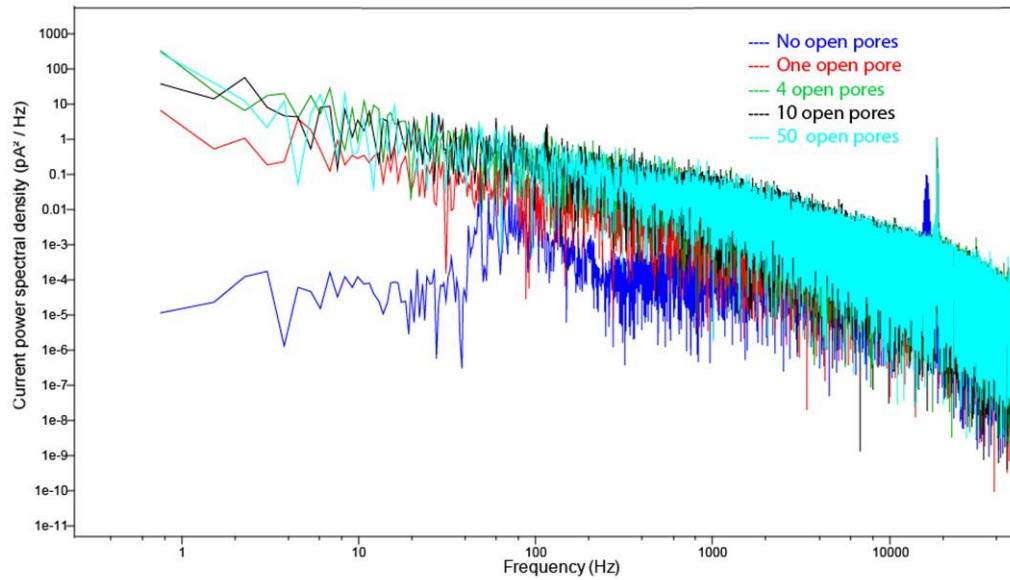


**Figure 6.9** Current power spectra density versus frequency at +200 mV, filtered at 10 KHz in 1M KCl buffered at pH 8.0 for (blue) no open pore, (red) one open pore, (green) 4 open pores, (black) 10 open pores and (light blue) 50 open pores cases, showing comparable high-frequency noise and more diverse low-frequency noise.

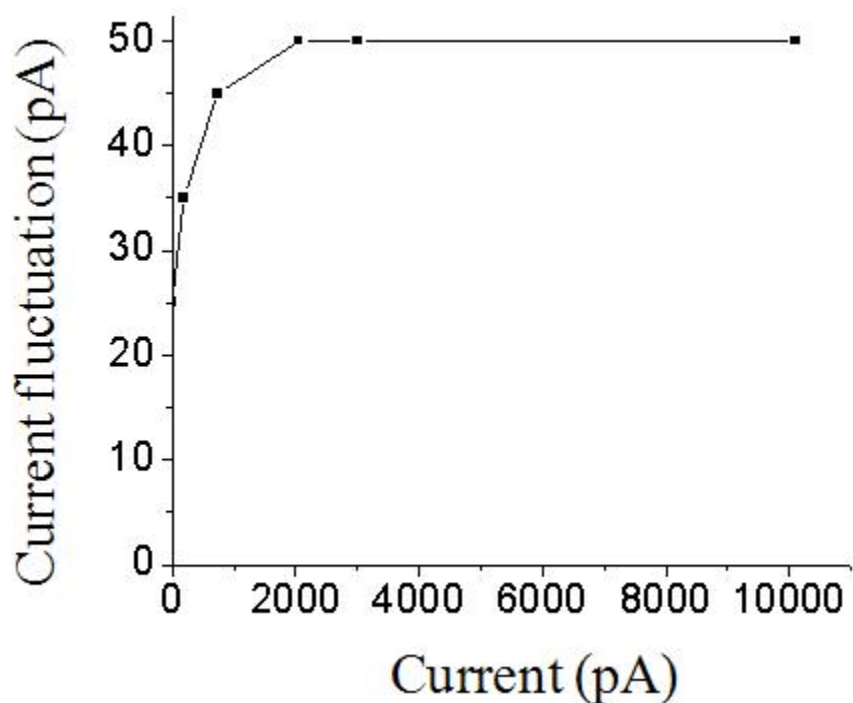


**Figure 6.10** Current fluctuation as a function of overall current (corresponding to the number of open pores in our nanopore array).

### 6.6 Current blockade frequency as a function of pore number

The nanopore array device is advantageous over the single solid-state nanopore for its possibility of fast and highly parallel readout of biological information. As we claim in this article, the overall current blockade frequency is the sum of the dsDNA translocation events on all nanopores supported over the FIBed aperture. So current blockade frequency should increase with the number of nanopores above the aperture. Three parallel DNA translocation experiments were conducted on samples with FIBed apertures of three different sizes to study the frequency as a function of the number of nanopores. The selected aperture sizes are 40x56nm, 69x73nm and 86x95nm (the

apertures are elliptical in shape so the area is determined from the long and short axes). The confined mesopore number after coating our thin film is calculated to be 70, 152 and 253 respectively. Figure 6.11 shows that the current blockage frequency increases with pore number, implying nanopore array device enhances the throughput of DNA translocation.

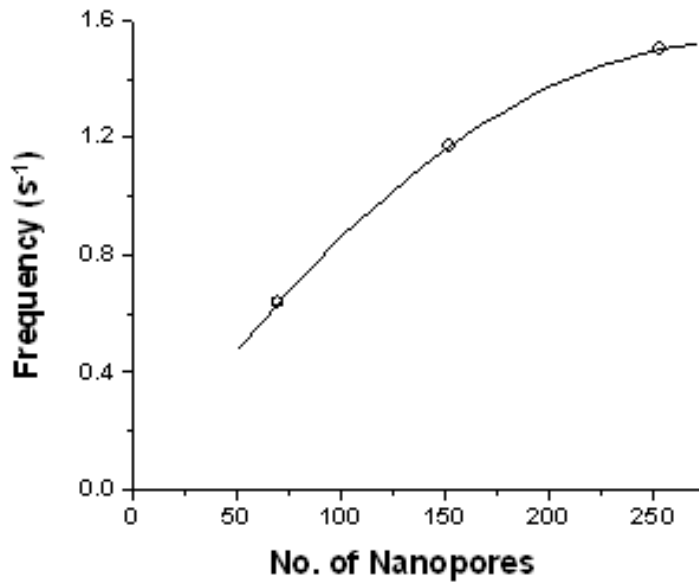


**Figure 6.11** Current blockage frequency as a function of the number of nanopores confined by FIBed hole.



## Chapter 7

### Conclusions and Future work

#### Conclusions:

We demonstrate a simple self-assembly procedure to create a free-standing nanopore array and its further physical and chemical modification by atomic layer deposition. Compared to lithography or etching, which yield individual, shallow, straight-through nanopores, self-assembly provides a novel means to direct the size, shape, and tortuosity of an array of solid-state nanopores. Subsequent conformal ALD of an oxide or silane reduces uniformly the diameters of all pores allowing, for example, the array to be tuned to transport efficiently ssDNA and reject dsDNA. Compared to protein pores of comparable pore diameters, the greater pore length combined with the kinked pore shape, derived from mixed distorted bcc (with  $Fmmm$  symmetry) and hcp mesophases, increases the frictional force and reduces the translocation velocity by a factor of up to 5. Our approach demonstrates how pore size and shape combine to influence translocation and to address the important issue of reducing translocation speed<sup>24, 50, 138</sup>. The qualitative DNA translocation characteristics developed in our nanopore array, e.g. the linear dependence of translocation time on polymer molecular weight and quadratic dependence of translocation velocity on voltage, can be understood on the basis of a 1D diffusion model, where factors contributing to the frictional force, *viz.* pore diameter, length, shape, and specific interactions, are coalesced into a single barrier potential. We anticipate that future improvements such as integration of our kinked nanopore array into a three

electrode ‘chem-FET’ architecture could combine reduced translocation velocities with increased signal to noise helping the field to realize the goal of direct DNA sequencing.

## **Future work:**

### **1. Further reducing translocation speed**

There are some other approaches to achieving slow translocation velocities, such as adding organic salts in electrolyte solutions<sup>155</sup>, controlling temperature, viscosity<sup>138</sup> and using optical tweezers (see Figure 7.1)<sup>24</sup>, some even achieving greater control over residence time than ours. A new approach using magnetic tweezers<sup>50</sup> is also reported recently to reverse DNA translocation through solid-state nanopores. However, our approach addresses the problem of the material itself (creating kinked pores other than straight through pores), which represents a different and perhaps complementary approach to those indicated above, as combining our kinked nanopore array with the above methods such as optical tweezing could present a new option for further controlling DNA translocation speed.

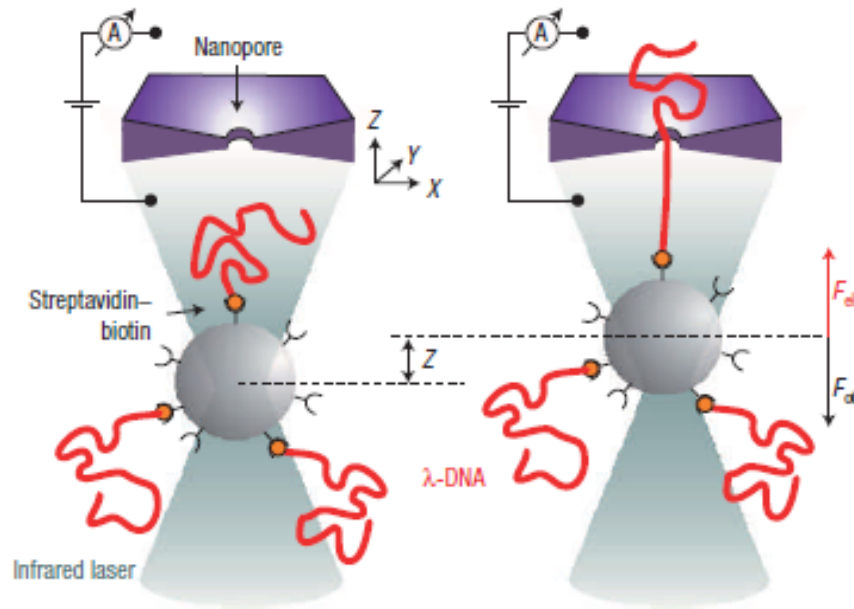


**Figure 7.1** Schematic of optical tweezer approach for DNA detection (Adopted from Keyser et al.<sup>24</sup>)

## 2. Further thinning film thickness and applying PA-ALD for more thickness control

Another obstacle impeding polymer identification and sequencing in nanopores, along with the translocation speed, is the pore length (that is, membrane thickness in conventional nanopores)<sup>111</sup>. Ideally, a nanopore system eliciting a distinct electrical signal from the space between bases to provide a clear count of the number of bases that are translocated is required for DNA sequencing. However, none of the current nanopore approaches can achieve single nucleotide discrimination because the pore lengths are much longer than the space between bases. Although this challenge won't diminish the significance of nanopore sequencing as compared to many other advantages it provides, further thinning the film thickness can be a promising research area that will broaden the applications of nanopore approach. In this dissertation, we had dramatically reduced film

thickness (from ~300 nm to ~30 nm) while maintaining high ordered periodic mesoporous structure. The free-standing membrane we report here is four unit cells thick and very uniform – reducing its thickness by one unit cell at a time is feasible by further steps of dilution of the precursor sol. We have also demonstrated plasma-assisted ALD<sup>126</sup> as a means to restrict ALD to a several-nm thick ‘aperture’ at the mouth of a pore<sup>156</sup>. In combination these advances could enable optimization of the transport characteristics of our general kinked array construct.

### **3. Integration of nanopore array on a wide range of devices**

One advantage of our self-assembled nanopore array fabrication, as discussed in Chapter 1, is that it can be easily integrated into different devices for its simple process. Although all the experiments described in this dissertation were conducted on single nanopore array system (i.e. mesoporous thin film spanning a single FIBed hole rather than an array of FIBed holes), it should be noted that the large area self-assembly process that we report allows us to prepare easily ‘arrays of nanopore arrays’ by evaporation-induced self-assembly (e.g. spin-coating) over substrates prepared with arrays of holes formed by FIB or anodization or conventional lithography (e.g. interferometric lithography to create a sparse arrays of holes), where each hole could be electronically and/or optically addressable. Our process is inherently scalable and can be further guided by lithographically defined features and tuned over large areas with ALD or plasma-assisted ALD.

Figure 7.2 shows the schematic of an ‘arrays of nanopore arrays’ device. It can find application in bioseparation as well as rapid and highly parallel read out of biological

information that require high throughput on large scale. As discussed in Chapter 4.3, the current FIB facility and technology in our lab allow us to make arrays of holes formed by FIB on a single substrate. Also in Chapter 4.3, we have demonstrated a so-called ‘selective nanopore blocking by focused-electron-beam’ new technique to block most of the nanopores while only leave one or a few nanopores open on the FIBed hole. With this capability of directing our nanopore array to larger or smaller scale, our approach open up the opportunities of solid-state nanopores in single molecule analysis and many other gating-, separation- and detection- related research areas.

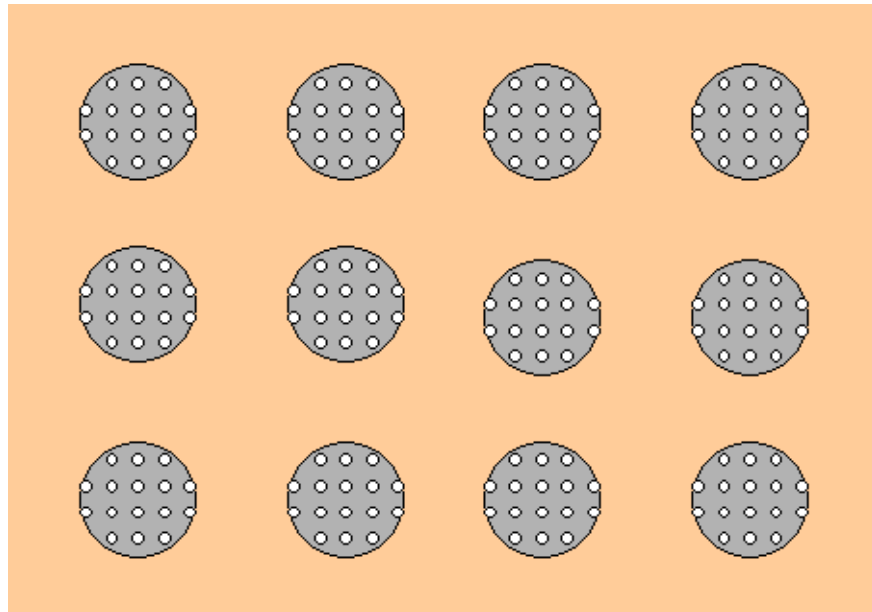


**Figure 7.2** Schematic of “arrays of nanopore array” device by integrating self-assembled nanopore array into arrays of holes made by FIB.

#### 4. Nanofluidic FET device

In this dissertation we have demonstrated the selectivity of highly charged stiff polymer (in this case ssDNA and dsDNA) through size-selective nanopores engineered by ALD. However, the polymer in this case are strongly biased local to pore entrance and thus gating cutoffs are non-selective. Open questions on the range of possible dynamics and mechanisms of electrokinetic force driven polymer threading into a nanochannel/nanopore should be addressed to fully understand the energetic requirement for a polymer to enter a narrow fluidic channel and achieve selective polymer gating. Instead of the nanopore array platform described in this dissertation, a new nanofluidic architecture is proposed for advanced polymer sensing and gating (see Figure 7.3). With this three electrode “chem-FET” architecture, we not only expect to combine the reduced translocation speed with increased signal to noise helping the field to realize the goal of direct DNA sequencing, but also expect to achieve selective polymer gating for a broader range of polymer options, like low charged, flexible protein, whose threading and gating cutoffs have not even been demonstrated before. This is an extension of our DNA study on the development, understanding, and exploitation of integrated, precision-fabricated nano/microfluidic architectures for selective detection, separation and gating of polymers.

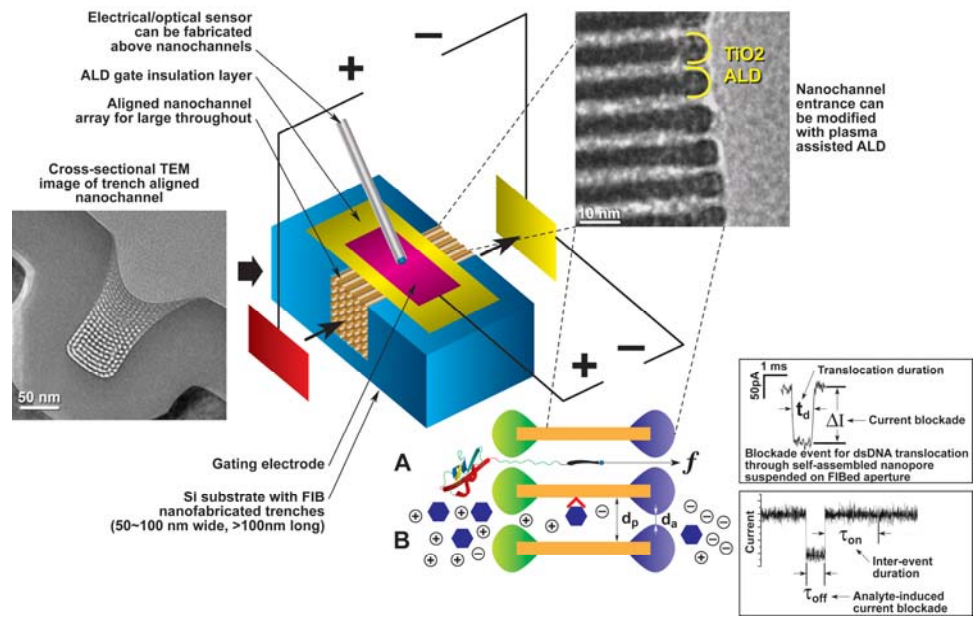


**Figure 7.3** Nanofluidic gate architecture with proposed incorporation of field effect transistor circuitry for advanced sensing and gating. Aligned channels are fabricated by silica self-assembly within lithographically defined trenches and further modified at the entrances and exits by PA-ALD (see TEM images). As illustrated schematically (bottom center) pore entrances and exits can be differentially modified with arbitrary materials (green and blue). Magnitude and duration of ion current occlusion during polymer translocation or analyte binding allows sensing and detection at individual polymer/analyte level – see insets on right.

## Reference

1. Miller, C. Ion channels: doing hard chemistry with hard ions. *Current Opinion in Chemical Biology* 4, 148-151 (2000).
2. MacKinnon, R. Potassium channels. *Febs Letters* 555, 62-65 (2003).
3. Sui, H. X., Han, B. G., Lee, J. K., Walian, P. & Jap, B. K. Structural basis of water-specific transport through the AQP1 water channel. *Nature* 414, 872-878 (2001).
4. Lander, E. S. et al. Initial sequencing and analysis of the human genome. *Nature* 409, 860-921 (2001).
5. Venter, J. C. et al. The sequence of the human genome. *Science* 291, 1304-+ (2001).
6. Sanger, F., Nicklen, S. & Coulson, A. R. DNA Sequencing with Chain-Terminating Inhibitors. *Proceedings of the National Academy of Sciences of the United States of America* 74, 5463-5467 (1977).
7. Shendure, J., Mitra, R. D., Varma, C. & Church, G. M. Advanced sequencing technologies: Methods and goals. *Nature Reviews Genetics* 5, 335-344 (2004).
8. Metzker, M. L. Emerging technologies in DNA sequencing. *Genome Research* 15, 1767-1776 (2005).
9. Chan, E. Y. Advances in sequencing technology. *Mutation Research-Fundamental and Molecular Mechanisms of Mutagenesis* 573, 13-40 (2005).
10. Mardis, E. R. The impact of next-generation sequencing technology on genetics. *Trends in Genetics* 24, 133-141 (2008).



11. Gupta, P. K. Ultrafast and low-cost DNA sequencing methods for applied genomics research. *Proceedings of the National Academy of Sciences India Section B-Biological Sciences* 78, 91-102 (2008).
12. Gupta, P. K. Single-molecule DNA sequencing technologies for future genomics research. *Trends in Biotechnology* 26, 602-611 (2008).
13. Jett, J. H. et al. High-Speed DNA Sequencing - an Approach Based Upon Fluorescence Detection of Single Molecules. *Journal of Biomolecular Structure & Dynamics* 7, 301-309 (1989).
14. Davis, L. M. et al. Rapid DNA Sequencing Based Upon Single Molecule Detection. *Genetic Analysis-Biomolecular Engineering* 8, 1-7 (1991).
15. Harding, J. D. & Keller, R. A. Single-Molecule Detection as an Approach to Rapid DNA Sequencing. *Trends in Biotechnology* 10, 55-57 (1992).
16. Brakmann, S. & Lobermann, S. A further step towards single-molecule sequencing: *Escherichia coli* exonuclease III degrades DNA that is fluorescently labeled at each base pair. *Angewandte Chemie-International Edition* 41, 3215-+ (2002).
17. Werner, J. H. et al. Progress towards single-molecule DNA sequencing: a one color demonstration. *Journal of Biotechnology* 102, 1-14 (2003).
18. Crut, A. et al. Detection of single DNA molecules by multicolor quantum-dot end-labeling. *Nucleic Acids Research* 33, - (2005).
19. Braslavsky, I., Hebert, B., Kartalov, E. & Quake, S. R. Sequence information can be obtained from single DNA molecules. *Proceedings of the National Academy of Sciences of the United States of America* 100, 3960-3964 (2003).

20. Bayley, H. Sequencing single molecules of DNA. *Current Opinion in Chemical Biology* 10, 628-637 (2006).
21. Kasianowicz, J. J., Brandin, E., Branton, D. & Deamer, D. W. Characterization of individual polynucleotide molecules using a membrane channel. *Proceedings of the National Academy of Sciences of the United States of America* 93, 13770-13773 (1996).
22. Akeson, M., Branton, D., Kasianowicz, J. J., Brandin, E. & Deamer, D. W. Microsecond time-scale discrimination among polycytidylic acid, polyadenylic acid, and polyuridylic acid as homopolymers or as segments within single RNA molecules. *Biophysical Journal* 77, 3227-3233 (1999).
23. Meller, A., Nivon, L., Brandin, E., Golovchenko, J. & Branton, D. Rapid nanopore discrimination between single polynucleotide molecules. *Proceedings of the National Academy of Sciences of the United States of America* 97, 1079-1084 (2000).
24. Keyser, U. F. et al. Direct force measurements on DNA in a solid-state nanopore. *Nature Physics* 2, 473-477 (2006).
25. Berg, H. C. *Random Walks in Biology* (Princeton University Press, Princeton, New Jersey, 1993).
26. Henrickson, S. E., Misakian, M., Robertson, B. & Kasianowicz, J. J. Driven DNA transport into an asymmetric nanometer-scale pore. *Physical Review Letters* 85, 3057-3060 (2000).
27. Nakane, J. J., Akeson, M. & Marziali, A. Nanopore sensors for nucleic acid analysis. *Journal of Physics-Condensed Matter* 15, R1365-R1393 (2003).

28. Bustamante, C., Marko, J. F., Siggia, E. D. & Smith, S. Entropic Elasticity of Lambda-Phage DNA. *Science* 265, 1599-1600 (1994).
29. Hagerman, P. J. Flexibility of DNA. *Annual Review of Biophysics and Biophysical Chemistry* 17, 265-286 (1988).
30. Tinland, B., Pluen, A., Sturm, J. & Weill, G. Persistence length of single-stranded DNA. *Macromolecules* 30, 5763-5765 (1997).
31. Wiggins, P. A. et al. High flexibility of DNA on short length scales probed by atomic force microscopy. *Nature Nanotechnology* 1, 137-141 (2006).
32. Coulter, W. H. Means for counting particles in suspended in a fluid. U.S. Patent, 2,656,508 (1953).
33. Bayley, H. & Martin, C. R. Resistive-pulse sensing - From microbes to molecules. *Chemical Reviews* 100, 2575-2594 (2000).
34. Deblois, R. W. & Wesley, R. K. A. Sizes and Concentrations of Several Type-C Oncornaviruses and Bacteriophage-T2 by Resistive-Pulse Technique. *Journal of Virology* 23, 227-233 (1977).
35. Mueller, P., Rudin, D. O., Tien, H. T. & Wescott, W. C. Reconstitution of Cell Membrane Structure in Vitro and Its Transformation into an Excitable System. *Nature* 194, 979-& (1962).
36. Hladky, S. B. & Haydon, D. A. Discreteness of Conductance Change in Bimolecular Lipid Membranes in Presence of Certain Antibiotics. *Nature* 225, 451-& (1970).
37. Neher, E. & Sakmann, B. Single-Channel Currents Recorded from Membrane of Denervated Frog Muscle-Fibers. *Nature* 260, 799-802 (1976).

38. Hamill, O. P., Marty, A., Neher, E., Sakmann, B. & Sigworth, F. J. Improved Patch-Clamp Techniques for High-Resolution Current Recording from Cells and Cell-Free Membrane Patches. *Pflugers Archiv-European Journal of Physiology* 391, 85-100 (1981).
39. Simmons, R. M., Finer, J. T., Chu, S. & Spudich, J. A. Quantitative measurements of force and displacement using an optical trap. *Biophysical Journal* 70, 1813-1822 (1996).
40. Bennink, M. L. et al. Unfolding individual nucleosomes by stretching single chromatin fibers with optical tweezers. *Nature Structural Biology* 8, 606-610 (2001).
41. Baumann, C. G. et al. Stretching of single collapsed DNA molecules. *Biophysical Journal* 78, 1965-1978 (2000).
42. Perkins, T. T., Quake, S. R., Smith, D. E. & Chu, S. Relaxation of a Single DNA Molecule Observed by Optical Microscopy. *Science* 264, 822-826 (1994).
43. Perkins, T. T., Smith, D. E., Larson, R. G. & Chu, S. Stretching of a Single Tethered Polymer in a Uniform-Flow. *Science* 268, 83-87 (1995).
44. Chiu, D. T. & Zare, R. N. Biased diffusion, optical trapping, and manipulation of single molecules in solution. *Journal of the American Chemical Society* 118, 6512-6513 (1996).
45. Smith, D. E., Babcock, H. P. & Chu, S. Single-polymer dynamics in steady shear flow. *Science* 283, 1724-1727 (1999).

46. Liphardt, J., Onoa, B., Smith, S. B., Tinoco, I. & Bustamante, C. Reversible unfolding of single RNA molecules by mechanical force. *Science* 292, 733-737 (2001).
47. Asbury, C. L. & van den Engh, G. Trapping of DNA in nonuniform oscillating electric fields. *Biophysical Journal* 74, 1024-1030 (1998).
48. Amblard, F., Yurke, B., Pargellis, A. & Leibler, S. A magnetic manipulator for studying local rheology and micromechanical properties of biological systems. *Review of Scientific Instruments* 67, 818-827 (1996).
49. Gosse, C. & Croquette, V. Magnetic tweezers: Micromanipulation and force measurement at the molecular level. *Biophysical Journal* 82, 3314-3329 (2002).
50. Peng, H. B. & Ling, X. S. S. Reverse DNA translocation through a solid-state nanopore by magnetic tweezers. *Nanotechnology* 20, - (2009).
51. Evans, E., Ritchie, K. & Merkel, R. Sensitive Force Technique to Probe Molecular Adhesion and Structural Linkages at Biological Interfaces. *Biophysical Journal* 68, 2580-2587 (1995).
52. Florin, E. L., Moy, V. T. & Gaub, H. E. Adhesion Forces between Individual Ligand-Receptor Pairs. *Science* 264, 415-417 (1994).
53. Rief, M., Gautel, M., Schemmel, A. & Gaub, H. E. The mechanical stability of immunoglobulin and fibronectin III domains in the muscle protein titin measured by atomic force microscopy. *Biophysical Journal* 75, 3008-3014 (1998).
54. Enderlein, J. Theoretical investigation of aspects of single-molecule fluorescence detection in microcapillaries. *Cytometry* 36, 195-199 (1999).

55. Van Orden, A., Machara, N. P., Goodwin, P. M. & Keller, R. A. Single molecule identification in flowing sample streams by fluorescence burst size and intraburst fluorescence decay rate. *Analytical Chemistry* 70, 1444-1451 (1998).
56. Zhuang, X. W. et al. Correlating structural dynamics and function in single ribozyme molecules. *Science* 296, 1473-1476 (2002).
57. Lavery, R., Lebrun, A., Allemand, J. F., Bensimon, D. & Croquette, V. Structure and mechanics of single biomolecules: experiment and simulation. *Journal of Physics-Condensed Matter* 14, R383-R414 (2002).
58. Goodwin, P. M. et al. Rapid Sizing of Individual Fluorescently Stained DNA Fragments by Flow-Cytometry. *Nucleic Acids Research* 21, 803-806 (1993).
59. Schwartz, D. C. et al. Ordered Restriction Maps of *Saccharomyces-Cerevisiae* Chromosomes Constructed by Optical Mapping. *Science* 262, 110-114 (1993).
60. Haab, B. B. & Mathies, R. A. Single-Molecule Fluorescence Burst Detection of DNA Fragments Separated Capillary Electrophoresis. *Analytical Chemistry* 67, 3253-3260 (1995).
61. Haab, B. B. & Mathies, R. A. Single-molecule detection of DNA separations in microfabricated capillary electrophoresis chips employing focused molecular streams. *Analytical Chemistry* 71, 5137-5145 (1999).
62. Anantharaman, T. S., Mishra, B. & Schwartz, D. C. Genomics via optical mapping.2. Ordered restriction maps. *Journal of Computational Biology* 4, 91-118 (1997).
63. Wang, Y. K., Huff, E. J. & Schwartz, D. C. Optical Mapping of Site-Directed Cleavages on Single DNA-Molecules by the RecA-Assisted Restriction-

- Endonuclease Technique. Proceedings of the National Academy of Sciences of the United States of America 92, 165-169 (1995).
64. Gilmanshin, R. & Chan, E. in US Patent Specification 6253286 (US Genomics, Inc., USA, 2001).
  65. Chan, E. in US Patent Specification 6355420 (USA, 2002).
  66. Neuman, K. C. & Block, S. M. Optical trapping. Review of Scientific Instruments 75, 2787-2809 (2004).
  67. Lee, J. W. & Meller, A. Perspectives in Bioanalysis (ed. Mitchelson, K.) (Elsevier, Amsterdam, 2007).
  68. Colton, C. K., Lai, C. J. & Satterfield, C. N. Diffusion and Partitioning of Macromolecules within Finely Porous-Glass. Aiche Journal 21, 289-298 (1975).
  69. Zwolak, M. & Di Ventura, M. Colloquium: Physical approaches to DNA sequencing and detection. Reviews of Modern Physics 80, 141-165 (2008).
  70. Meller, A. Dynamics of polynucleotide transport through nanometre-scale pores. Journal of Physics-Condensed Matter 15, R581-R607 (2003).
  71. Meller, A., Nivon, L. & Branton, D. Voltage-driven DNA translocations through a nanopore. Physical Review Letters 86, 3435-3438 (2001).
  72. Drmanac, R. e. a. Sequencing by hybridization (SBH):advantages, achievements, and opportunities. Adv. Biochem. Eng. Biotechnol. 77, 75-101 (2002).
  73. Ling, X. S., Bready, B. & Pertsinidis, A. (ed. patent, U.) (2007).
  74. Movileanu, L., Howorka, S., Braha, O. & Bayley, H. Detecting protein analytes that modulate transmembrane movement of a polymer chain within a single protein pore. Nature Biotechnology 18, 1091-1095 (2000).

75. Gu, L. Q., Braha, O., Conlan, S., Cheley, S. & Bayley, H. Stochastic sensing of organic analytes by a pore-forming protein containing a molecular adapter. *Nature* 398, 686-690 (1999).
76. Bayley, H. *NanoBiotechnology* (2005).
77. Vercoutere, W. et al. Rapid discrimination among individual DNA hairpin molecules at single-nucleotide resolution using an ion channel (vol 19, pg 248, 2001). *Nature Biotechnology* 19, 681-681 (2001).
78. Mathe, J., Visram, H., Viasnoff, V., Rabin, Y. & Meller, A. Nanopore unzipping of individual DNA hairpin molecules. *Biophysical Journal* 87, 3205-3212 (2004).
79. Sauer-Budge, A. F., Nyamwanda, J. A., Lubensky, D. K. & Branton, D. Unzipping kinetics of double-stranded DNA in a nanopore. *Physical Review Letters* 90, - (2003).
80. Halverson, K. M. et al. Anthrax biosensor, protective antigen ion channel asymmetric blockade. *Journal of Biological Chemistry* 280, 34056-34062 (2005).
81. Li, J. et al. Ion-beam sculpting at nanometre length scales. *Nature* 412, 166-169 (2001).
82. Heng, J. B. et al. Sizing DNA using a nanometer-diameter pore. *Biophysical Journal* 87, 2905-2911 (2004).
83. Ho, C. et al. Electrolytic transport through a synthetic nanometer-diameter pore. *Proceedings of the National Academy of Sciences of the United States of America* 102, 10445-10450 (2005).



84. Storm, A. J., Chen, J. H., Ling, X. S., Zandbergen, H. W. & Dekker, C. Fabrication of solid-state nanopores with single-nanometre precision. *Nature Materials* 2, 537-540 (2003).
85. Siwy, Z. & Fulinski, A. Fabrication of a synthetic nanopore ion pump. *Physical Review Letters* 89, - (2002).
86. Chen, P. et al. Atomic layer deposition to fine-tune the surface properties and diameters of fabricated nanopores. *Nano Letters* 4, 1333-1337 (2004).
87. Chang, H. et al. DNA-mediated fluctuations in ionic current through silicon oxide nanopore channels. *Nano Letters* 4, 1551-1556 (2004).
88. Fan, R. et al. DNA translocation in inorganic nanotubes. *Nano Letters* 5, 1633-1637 (2005).
89. Saleh, O. A. & Sohn, L. L. An artificial nanopore for molecular sensing. *Nano Letters* 3, 37-38 (2003).
90. Langer, R. & Tirrell, D. A. Designing materials for biology and medicine. *Nature* 428, 487-492 (2004).
91. Mitsui, T., Stein, D., Kim, Y. R., Hoogerheide, D. & Golovchenko, J. A. Nanoscale volcanoes: Accretion of matter at ion-sculpted nanopores. *Physical Review Letters* 96, - (2006).
92. Kresge, C. T., Leonowicz, M. E., Roth, W. J., Vartuli, J. C. & Beck, J. S. Ordered Mesoporous Molecular-Sieves Synthesized by a Liquid-Crystal Template Mechanism. *Nature* 359, 710-712 (1992).
93. Brinker, C., Lu, Y., Sellinger, A. & Fan, H. Evaporation-induced self-assembly: Nanostructures made easy. *ADVANCED MATERIALS* 11, 579-+ (1999).

94. Besson, S., Ricolleau, C., Gacoin, T., Jacquiod, C. & Boilot, J. P. A new 3D organization of mesopores in oriented CTAB silica films. *Journal of Physical Chemistry B* 104, 12095-12097 (2000).
95. Liu, N. G., Assink, R. A., Smarsly, B. & Brinker, C. J. Synthesis and characterization of highly ordered functional mesoporous silica thin films with positively chargeable -NH<sub>2</sub> groups. *Chemical Communications*, 1146-1147 (2003).
96. Liu, N. G., Assink, R. A. & Brinker, C. J. Synthesis and characterization of highly ordered mesoporous thin films with -COOH terminated pore surfaces. *Chemical Communications*, 370-371 (2003).
97. Urade, V. N., Wei, T. C., Tate, M. P., Kowalski, J. D. & Hillhouse, H. W. Nanofabrication of double-gyroid thin films. (vol 19, pg 768, 2007). *Chemistry of Materials* 19, 2382-2382 (2007).
98. Carlsson, A. et al. The structure of MCM-48 determined by electron crystallography. *Journal of Electron Microscopy* 48, 795-798 (1999).
99. Kaneda, M. et al. Structural study of mesoporous MCM-48 and carbon networks synthesized in the spaces of MCM-48 by electron crystallography. *Journal of Physical Chemistry B* 106, 1256-1266 (2002).
100. Imai, M. et al. Kinetic pathway to double-gyroid structure. *Journal of Chemical Physics* 122, - (2005).
101. Liu, N. G. et al. Photoregulation of mass transport through a photoresponsive azobenzene-modified nanoporous membrane. *Nano Letters* 4, 551-554 (2004).

102. Zhao, X. S. & Lu, G. Q. Modification of MCM-41 by surface silylation with trimethylchlorosilane and adsorption study. *Journal of Physical Chemistry B* 102, 1556-1561 (1998).
103. Liu, J. et al. Molecular assembly in ordered mesoporosity: A new class of highly functional nanoscale materials. *Journal of Physical Chemistry A* 104, 8328-8339 (2000).
104. Ek, S., Iiskola, E. I. & Niinisto, L. Gas-phase deposition of aminopropylalkoxysilanes on porous silica. *Langmuir* 19, 3461-3471 (2003).
105. Ek, S. et al. A Si-29 and C-13 CP/MAS NMR study on the surface species of gas-phase-deposited gamma-aminopropylalkoxysilanes on heat-treated silica. *Journal of Physical Chemistry B* 108, 11454-11463 (2004).
106. Platschek, B., Petkov, N. & Bein, T. Tuning the structure and orientation of hexagonally ordered mesoporous channels in anodic alumina membrane hosts: A 2D small-angle X-ray scattering study. *Angewandte Chemie-International Edition* 45, 1134-1138 (2006).
107. Wu, Y. Y. et al. Composite mesostructures by nano-confinement. *Nature Materials* 3, 816-822 (2004).
108. Yamaguchi, A. et al. Self-assembly of a silica-surfactant nanocomposite in a porous alumina membrane. *Nature Materials* 3, 337-341 (2004).
109. Xomeritakis, G. et al. Aerosol-assisted deposition of surfactant-templated mesoporous silica membranes on porous ceramic supports. *Microporous and Mesoporous Materials* 66, 91-101 (2003).

110. Patterson, N. et al. Controlled fabrication of nanopores using a direct focused ion beam approach with back face particle detection. *Nanotechnology* 19, - (2008).
111. Branton, D. et al. The potential and challenges of nanopore sequencing. *Nature Biotechnology* 26, 1146-1153 (2008).
112. Gregg, S. J. & Sing, K. S. W. Adsorption, surface area, and porosity (Academic Press, New York, 1982).
113. Tate, M. P. et al. Simulation and interpretation of 2D diffraction patterns from self-assembled nanostructured films at arbitrary angles of incidence: From grazing incidence (above the critical angle) to transmission perpendicular to the substrate. *Journal of Physical Chemistry B* 110, 9882-9892 (2006).
114. Storm, A. J. et al. Fast DNA translocation through a solid-state nanopore. *Nano Letters* 5, 1193-1197 (2005).
115. Falcaro, P., Grosso, D., Amenitsch, H. & Innocenzi, P. Silica orthorhombic mesostructured films with low refractive index and high thermal stability. *Journal of Physical Chemistry B* 108, 10942-10948 (2004).
116. Besson, S., Ricolleau, C., Gacoin, T., Jacquiod, C. & Boilot, J. P. Highly ordered orthorhombic mesoporous silica films. *Microporous and Mesoporous Materials* 60, 43-49 (2003).
117. Urade, V. N. & Hillhouse, H. W. Synthesis of thermally stable highly ordered nanoporous tin oxide thin films with a 3D face-centered orthorhombic nanostructure. *Journal of Physical Chemistry B* 109, 10538-10541 (2005).

118. Kalantar, D. H. et al. Direct observation of the alpha-epsilon transition in shock-compressed iron via nanosecond x-ray diffraction. *Physical Review Letters* 95, - (2005).
119. Ricco, A. J., Frye, G. C. & Martin, S. J. Determination of Bet Surface-Areas of Porous Thin-Films Using Surface Acoustic-Wave Devices. *Langmuir* 5, 273-276 (1989).
120. Sing, K. S. W. et al. Reporting Physisorption Data for Gas Solid Systems with Special Reference to the Determination of Surface-Area and Porosity (Recommendations 1984). *Pure and Applied Chemistry* 57, 603-619 (1985).
121. Hidrobo, A., Retuert, J. & Araya, R. Mesoporous aluminosilicate molecular sieve: Control of textural properties by post-synthesis hydrothermal treatment. *Journal of the Chilean Chemical Society* 48, 37-40 (2003).
122. Wu, Z. Y. et al. Formation of cubic Ia3d silicas and metal oxide-loaded silicas using a triblock copolymer (EO20PO70EO20) - Acetate mixture as structure director in aqueous solution. *Chemistry of Materials* 19, 1613-1625 (2007).
123. Kruk, M. & Jaroniec, M. Gas adsorption characterization of ordered organic-inorganic nanocomposite materials. *Chemistry of Materials* 13, 3169-3183 (2001).
124. Galarneau, A., Desplandier, D., Dutartre, R. & Di Renzo, F. Micelle-templated silicates as a test bed for methods of mesopore size evaluation. *Microporous and Mesoporous Materials* 27, 297-308 (1999).
125. Xomeritakis, G. et al. Anodic alumina supported dual-layer microporous silica membranes. *Journal of Membrane Science* 287, 157-161 (2007).

126. Jiang, Y. B., Liu, N. G., Gerung, H., Cecchi, J. L. & Brinker, C. J. Nanometer-thick conformal pore sealing of self-assembled mesoporous silica by plasma-assisted atomic layer deposition. *Journal of the American Chemical Society* 128, 11018-11019 (2006).
127. Khardani, M., Bouaicha, M., Bessais, B. Bruggeman effective medium approach for modeling optical properties of porous silicon: comparison with experiment. *phys. stat. sol.* 4, 1986-1990 (2007).
128. Cameron, M. A., Gartland, I. P., Smith, J. A., Diaz, S. F. & George, S. M. Atomic layer deposition of SiO<sub>2</sub> and TiO<sub>2</sub> in alumina tubular membranes: Pore reduction and effect of surface species on gas transport. *Langmuir* 16, 7435-7444 (2000).
129. Gregg, S. J. & Sing, K. S. W. *Adsorption, Surface Area and Porosity*, 214 (1967).
130. Ek, S. et al. Atomic layer deposition of a high-density aminopropylsiloxane network on silica through sequential reactions of gamma-aminopropyltrialkoxysilanes and water. *Langmuir* 19, 10601-10609 (2003).
131. Maglia, G., Restrepo, M. R., Mikhailova, E. & Bayley, H. Enhanced translocation of single DNA molecules through alpha-hemolysin nanopores by manipulation of internal charge. *Proceedings of the National Academy of Sciences of the United States of America* 105, 19720-19725 (2008).
132. Wanunu, M. & Meller, A. Chemically modified solid-state nanopores. *Nano Letters* 7, 1580-1585 (2007).
133. Heng, J. B. et al. The electromechanics of DNA in a synthetic nanopore. *Biophysical Journal* 90, 1098-1106 (2006).

134. Li, J. L., Gershow, M., Stein, D., Brandin, E. & Golovchenko, J. A. DNA molecules and configurations in a solid-state nanopore microscope. *Nature Materials* 2, 611-615 (2003).
135. Smeets, R. M. M. et al. Salt dependence of ion transport and DNA translocation through solid-state nanopores. *Nano Letters* 6, 89-95 (2006).
136. Chen, P. et al. Probing single DNA molecule transport using fabricated nanopores. *Nano Letters* 4, 2293-2298 (2004).
137. Storm, A. J., Chen, J. H., Zandbergen, H. W. & Dekker, C. Translocation of double-strand DNA through a silicon oxide nanopore. *Physical Review E* 71, - (2005).
138. Fologea, D., Uplinger, J., Thomas, B., McNabb, D. S. & Li, J. L. Slowing DNA translocation in a solid-state nanopore. *Nano Letters* 5, 1734-1737 (2005).
139. Lubensky, D. K. & Nelson, D. R. Driven polymer translocation through a narrow pore. *Biophysical Journal* 77, 1824-1838 (1999).
140. Wanunu, M., Sutin, J., McNally, B., Chow, A. & Meller, A. DNA Translocation Governed by Interactions with Solid-State Nanopores. *Biophysical Journal* 95, 4716-4725 (2008).
141. Deamer, D. W. & Branton, D. Characterization of nucleic acids by nanopore analysis. *Accounts of Chemical Research* 35, 817-825 (2002).
142. McNally, B., Wanunu, M. & Meller, A. Electromechanical Unzipping of Individual DNA Molecules Using Synthetic Sub-2 nm Pores. *Nano Letters* 8, 3418-3422 (2008).

143. Skinner, G. M., van den Hout, M., Broekmans, O., Dekker, C. & Dekker, N. H. Distinguishing Single- and Double-Stranded Nucleic Acid Molecules Using Solid-State Nanopores. *Nano Letters* 9, 2953-2960 (2009).
144. Smith, D. E., Perkins, T. T. & Chu, S. Dynamical scaling of DNA diffusion coefficients. *Macromolecules* 29, 1372-1373 (1996).
145. Mathe, J., Aksimentiev, A., Nelson, D. R., Schulten, K. & Meller, A. Orientation discrimination of single-stranded DNA inside the alpha-hemolysin membrane channel. *Proceedings of the National Academy of Sciences of the United States of America* 102, 12377-12382 (2005).
146. Gerland, U., Bundschuh, R. & Hwa, T. Translocation of structured polynucleotides through nanopores. *Physical Biology* 1, 19-26 (2004).
147. Lam, P. M., Liu, F. & Ou-Yang, Z. C. Driven translocation of a polynucleotide chain through a nanopore: A continuous time Monte Carlo study. *Physical Review E* 74, - (2006).
148. Lua, R. C. & Grosberg, A. Y. First passage times and asymmetry of DNA translocation. *Physical Review E* 72, - (2005).
149. Tabard-Cossa, V., Trivedi, D., Wiggin, M., Jetha, N. N. & Marziali, A. Noise analysis and reduction in solid-state nanopores. *Nanotechnology* 18, - (2007).
150. Dimitrov, V. et al. Nanopores in solid-state membranes engineered for single molecule detection. *Nanotechnology* 21, - (2010).
151. Danelon, C., Santschi, C., Brugger, J. & Vogel, H. Fabrication and functionalization of nanochannels by electron-beam-induced silicon oxide deposition. *Langmuir* 22, 10711-10715 (2006).



152. Nilsson, J., Lee, J. R. I., Ratto, T. V. & Letant, S. E. Localized functionalization of single nanopores. *Advanced Materials* 18, 427-+ (2006).
153. Smeets, R. M. M., Dekker, N. H. & Dekker, C. Low-frequency noise in solid-state nanopores. *Nanotechnology* 20, - (2009).
154. Smeets, R. M. M., Keyser, U. F., Dekker, N. H. & Dekker, C. Noise in solid-state nanopores. *Proceedings of the National Academy of Sciences of the United States of America* 105, 417-421 (2008).
155. de Zoysa, R. S. S. et al. Slowing DNA Translocation through Nanopores Using a Solution Containing Organic Salts. *Journal of Physical Chemistry B* 113, 13332-13336 (2009).
156. Moghaddam, S. et al. An inorganic-organic proton exchange membrane for fuel cells with a controlled nanoscale pore structure. *Nature Nanotechnology* 5, 230-236 (2010).